Doctoral   Engineering

2010-6

Antenna Development for Radio Frequency Hyperthermia Applications

Sergio Curto

Technological University Dublin, sergiocurtoramos@gmail.com

Antenna Development for Radio Frequency Hyperthermia Applications

Sergio Curto

Bachelor of Engineering

Doctor of Philosophy

Supervisor:

Dr. Max J. Ammann

DUBLIN INSTITUTE OF TECHNOLOGY

SCHOOL OF ELECTRONIC & COMMUNICATIONS ENGINEERING

JUNE 2010

Abstract

This thesis deals with the design steps, development and validation of an applicator for radio frequency hyperthermia cancer therapy. An applicator design to enhance targeted energy coupling is a key enabler for preferential temperature increments in tumour regions. A single-element, near-field approach requires a miniaturised solution that addresses ergonomic needs and is tolerant to patient anatomy. The antenna near-field modality and the high-dielectric patient loading introduce significant analytical and computational resource challenges. The antenna input impedance has to be sufficiently insensitive to in-band resonant detuning and the fields in the tissue can be targeted to selected areas in the patient.

An introduction to the medical and biological background of hyperthermia is presented. The design requirements of antennas for medical and in particular for hyperthermia applications are highlighted. Starting from a conventional circular patch, the antenna evolved into a compact circular patch with a concentric annular ring and slotted groundplane, operating at the 434 MHz Industrial Scientific and Medical frequency band. Feed point location is optimized for an energy deposition pattern aligned with the antenna centre.

The applicator is assessed with other published approaches and clinically used loop, dipole and square patch antennas. The antennas are evaluated for the unloaded condition and when loaded with a tri-layer body tissue numerical model. This model comprises skin, fat and transverse fiber of muscle of variable thicknesses to account for different body locations and patient anatomy. A waterbolus containing de-ionized water is added at the skin interface for superficial tissue cooling and antenna matching. The proposed applicator achieves a

penetration depth that supersedes other approaches while remaining compact
and an ergonomic fit to tumour areas on the body.

To consider the inner and peripheral complex shapes of human bodies, the
full human body numerical model developed by Remcom is used. This model
was segmented from 1 mm step computed tomography (CT) and magnetic
resonance imaging (MRI) cross-sections through and adult male and it com-
prises twenty-three tissue types with thermal and frequency-dependent dielec-
tric properties. The applicator performance is evaluated at three anatomical
body areas of the model to assess its suitability for treatment of tumours at
different locations. These three anatomical regions present different aperture
coupling and tissue composition. 'Different conformal waterbolus and air gap
thickness values are evaluated.

The models used in this work are validated with measurements performed in
a phantom containing a lossy liquid with dielectric properties representative of
homogeneous human body tissue. The dosimetric assessment system (DASY)
is used to evaluate the specific absorption rate (SAR) generated for the antenna
into the liquid. The measurement setup with the antenna, phantom and liquid
are simulated. Simulated and measured results in terms of specific absorption
rate and return loss are evaluated.

Declaration

I certify that this thesis which I now submit for examination for the award of PhD, is entirely my own work and has not been taken from the work of others save and to the extent that such work has been cited and acknowledged within the text of my own work.

This thesis was prepared according to the regulations for postgraduate study by research of the Dublin Institute of Technology and has not been submitted in whole or in part for an award in any other Institute or University.

The work reported on in this thesis conforms to the principles and requirements of the Institute's guidelines for ethics in research.

The Institute has permission to keep, to lend or to copy this thesis in whole or in part, on condition that any such use of the material of the thesis be duly acknowledged.

Signature: _____ Date 20·07·10

Sergio Curto

Acknowledgements

My first thanks are to my supervisor, Max J. Ammann, for his indispensable support throughout this project. Max has taught me a lot, directly and indirectly, and prepared me for my future professional endeavors. I consider myself fortunate as a student to have found a supervisor, and more than that, a friend as Max.

Thanks to my colleagues at the Antenna & High Frequency Research Centre, Maria, Antoine, Giuseppe, Matthias, Patrick, Shynu and Xiulong, for our enthusiastic scientific talks that guided my work during the last four years.

I want to acknowledge Victor Thorne and Hugh Tinsley for their medical guidance, and James Murphy for sharing his knowledge of radio frequency fields interaction with in-vitro cell systems.

I had the privilege to work at the Institute for Infocomm Research under the supervision of Zhi Ning Chen, with whom I shared enriching discussions on antenna miniaturization techniques. I want to thank Terence S. P. See for his help with the measurements, and Siew Bee Yeap, Wee Kian Toh and Jefnaj Al Afif for their support during my time in Singapore.

Thanks to all the friends who helped me during this period, and especially my housemates, with whom I shared most of my time, Laura, Seb, Marc, Margue, Aliche, because they were my family in Dublin.

I would like to express my gratitude to my parents Ventura and Rosa, and to my brothers Javi and Dani, who taught me to be curious and never stop learning, and provide me with unconditional support.

Thanks Melody, for this time together, for your never ending support, for sharing this journey with me.

Abbreviations and Definitions

Abbreviations

AG	Air Gap
AR	Annular Ring
AR-CCP	Annular Ring with Concentric Circular Patch
AR-CCP-GPS	Annular Ring with Concentric Circular Patch and Groundplane Slots
ARF	Annular Ring Fed
ASHO	Asian Society for Hyperthermic Oncology
AUT	Antenna Under Test
CAD	Computed Aided Design
ChT	Chemo Therapy
CP	Circular Patch
CPF	Circular Patch Fed
CSF	Cerebrospinal Fluid
CST	Computer Simulation Technology GmbH
CT	Computed Tomography
DAE	Data Acquisition Electronic
DASY	Dosimetric Assessment System
DNA	Deoxyribonucleic Acid
DRL	Distance Related Losses
EM	Electromagnetic
EOC	Electro Optical Converter

ESHO	European Society for Hyperthermic Oncology
FD	Feed Diagonal
FDTD	Finite Difference Time Domain
FIT	Finite Integration Technique
GPIB	General Purpose Interface Bus
HT	Hyperthermia
IEEE	Institute of Electrical and Electronics Engineers
IET	Institution of Engineering and Technology
	was IEE – Institution of Electrical Engineers
ISM	Industrial Scientific and Medical
LED	Light Emitting Diode
ML	Mismatch Losses
MR	Magnetic Resonance
MRI	Magnetic Resonance Imaging
MWS	*CST* Microwave Studio
PC	Personal Computer
PRFS	Proton Resonance Frequency Shift
RAM	Random Access Memory
RF	Radio Frequency
RFID	Radio Frequency Identification
RT	Radio Therapy
SAR	Specific Absorption Rate
STM	Society for Thermal Medicine
USB	Universal Serial Bus
UWB	Ultra Wide Bandwidth
VNA	Vector Network Analyzer
WB	Waterbolus
WHO	World Health Organization
XFDTD	Three-dimensional full wave electromagnetic solver based on the *FDTD* method

Definitions

c_0	speed of light in vacuum, $299\,792\,458$ $[\text{m/s}]$
ε_0	dielectric constant of free space, $8.854 \cdot 10^{-12}$ $[\text{F/m}]$

Contents

List of Figures

List of Tables

1. Introduction

T̲HE̲ American Cancer Society estimates that there were 1,479,350 new diagnosed cancer cases and 562,340 deaths from the disease in the USA in the year 2009 [1]. In Europe, there are 2.9 million new cases and 1.7 million cancer deaths per year [2]. The World Health Organization (WHO) established that cancer is one of the leading causes of death (along with heart disease and stroke) and deaths from cancer are expected to continue rising with an estimation of 12 million deaths worldwide in 2030 [3].

Early cancer detection and adequate treatment are crucial in the control of the disease [4]. While radiotherapy, chemotherapy and surgery, are the worldwide established conventional cancer treatments, some tumours cannot be treated by these therapies. Hypoxic cells are resistant to radiotherapy. Tumours with insufficient perfusion are unresponsive to chemotherapies. And tumours at high risk locations such as those located very close to the spine are not suitable for surgical resection [5–7].

1.1. Radio Frequency Hyperthermia

Radio frequency (RF) hyperthermia is an adjunct cancer treatment used with radio- or chemo-therapies [5–8] to increase their effectiveness. The performance of an RF hyperthermia system is proportional to the energy transfer into the targeted region. External RF hyperthermia antenna applicators are designed to non-invasively couple electromagnetic (EM) energy through human skin.
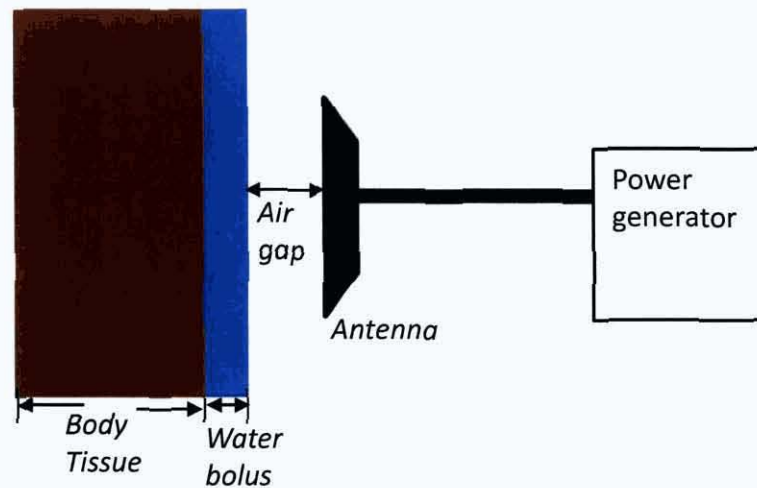
Figure 1.1.: Hyperthermia system schematic representation.

Figure 1.1 shows a schematic representation of a hyperthermia system. The antenna is a critical element in the hyperthermia system and its performance determines the EM energy deposition into the tissue, and the system quality. The energy is deployed in regions with cancerous tumour-masses to elevate the temperature to approximately $40 - 44\,°C$. Since tumours have reduced rates of temperature cooling due to naturally impeded blood flow, the non-ionizing application aims to selectively infuse the additional energy without damaging the enclosing healthy tissue. Benefits include the direct kill of raised temperature tumours cells, increased cell oxygenation, stimulation of the immune system, increased metabolic activity and an improved drug uptake in cells [5].

The first international congress on hyperthermic oncology in 1975 instigated the research and new interest in the hyperthermia field. After an encouraging first decade, the initial curiosity diminished following unsatisfactory clinical results [5] mainly due to the difficulties in adequately heating tumours [6]. Nowadays results of randomized clinical trials showing the effectiveness of improved hyperthermia therapy have generated a renewed and optimistic interest [5].

1.2. Motivation and Research Objectives

Enhancing tumour temperatures with EM energy is a complex task. Determining factors include the type, size and proximity of the applicator, the frequency of the power source, the applied-field polarization and the non-uniformity of patient anatomies [9]. Additionally, differing physiological responses to localized elevated temperatures and the consequent changes in the dielectric properties of the tumour can produce time-dependent variances during treatment.

The close presence of tissue and consequently near E-field interaction is a challenging environment for an applicator compared to the standard free space condition. The human body presents a variety of complex impedances which make it difficult for the systematic delivery of power from a transmitter via the antenna. Modelling the complexity of the human body requires powerful computational resources and the time required is proportional to the model accuracy. Dedicated resources are required for accurate simulation.

The main objectives of this research were to develop antennas for use in RF hyperthermia systems. While design criteria for medical antennas and in particular for hyperthermia antennas are detailed in Chapter 3, the main antenna requirements pursued in this work are listed as follows:

- Minimizing the size and weight of the applicator to simplify access to the treatment region, manoeuvrability during treatment and integration into a portable system,
- The antenna should remain sufficiently matched to the source frequency during unloaded and variably-loaded conditions to simplify the overall system stability,
- The applicator should present tangentially aligned E-fields to increase the penetration into the body tissue and to reduce the power necessary to couple energy into the tumour area,
- Avoidance of matching circuits to increase the efficiency of the system and simplify the specialized clinical use.

1.3. Multi-Disciplinary Research

This thesis highlights the background of hyperthermia from the medical point of view and describes the development, performance and evaluation process of a novel compact RF hyperthermia applicator.

The final goal is to further stimulate interest and research in hyperthermia technology for clinicians and engineers, and consequently, make this technique widely available to more patients suffering of cancer.

While the core work of this thesis was carried out in the Antenna & High Frequency Research Centre at the Dublin Institute of Technology, Dublin; and in the RF and Optical Department at the Institute for Infocomm Research, Singapore; this work involved collaboration with the Radiation & Environmental Science Centre, Focas Institute, Dublin; Institute of Technology Sligo, Sligo; and the Rose Lodge Clinic, Dublin. The collaboration involved exchange of ideas and advice.

1.4. Outline of this Thesis

Chapter 2 describes a general background for the work carried out in the thesis. The definition and historical evolution of hyperthermia are depicted. The physics of hyperthermia as well as clinical trials and treatments are described from the medical point of view. Benefits of ultrasound and radio frequency techniques for hyperthermia treatment are given. The concept of hyperthermia treatment planning is introduced. The interaction between antenna and human tissue and the dependence on frequency of operation and tissue dielectric properties is highlighted from the engineering point of view. Specific absorption rate and temperature calculations are introduced in addition to modelling techniques.

In Chapter 3 the antenna design requirements for hyperthermia applications are introduced, and the design process of the proposed compact patch antenna is presented. The antenna is evaluated next to a layer of homogeneous muscle tissue.

Chapter 4 evaluates the compact patch antenna with the clinically used wire loop and dipole designs and with the conventional square patch antenna in the presence of a tri-layer tissue human model.

Chapter 5 is devoted to an evaluation of the compact patch antenna when located at different anatomical regions of a realistic human body model. The investigation includes the use of conformal waterboluses and a study of various antenna-to-tissue air gap separations.

Chapter 6 concentrates on the explanation of the modelling validation, and the measurements conducted with the dosimetric assessment system (DASY) in a phantom containing a lossy liquid with dielectric properties representative of homogeneous human body tissue.

Chapter 7 brings together the main conclusions of this work, while an outlook to domains of possible future study are presented.

Findings published during this work have been presented in journals and conferences which are listed separately in the List of Publications.

2. Background

THIS chapter introduces hyperthermia as well as a brief historical evolution. The fundamental physics of hyperthermia is described and the medical background of the different methods, clinical trials and treatments are summarised. The benefits of RF hyperthermia are compared to ultrasound techniques. The engineering aspects of hyperthermia are detailed with special consideration to the frequency of operation and the dielectric properties of tissues that form the basis of antenna-human tissue interaction. The specific absorption rate and mechanism of temperature rise within the tissue is explained, and to conclude the chapter, the modelling and simulation methods used in this work are presented.

2.1. Introduction to Hyperthermia

2.1.1. Definition

Hyperthermia, also called thermal therapy, is defined as a medical treatment in which body tissue temperature is raised to between 40 and 44 °C [5]. Hyperthermia is used to treat muscular traumas and some cancer types. When used for muscular treatments it is usually for treating acute muscle injuries in sports, with the benefits of reducing pressure pain and contraction in physical medicine and rehabilitation [10]. When used in cancer treatment it is applied as adjunctive of conventional treatments, such as chemotherapy or radiotherapy, to increase their effectiveness. Hyperthermia increases the blood

flow which leads to an increase in perfusion and concentration of oxygen in the tumour region. The increase of oxygen enhances the effectiveness of radiotherapy and the increase in perfusion improves the drug uptake in cells for chemotherapy [7]. This work is focused on hyperthermia as a cancer treatment.

2.1.2. Historical Background of Hyperthermia

The use of heat as medical treatment can be traced to the age of the Egyptian Edwin Smith surgical papyrus (3,000 – 2,500 B.C.) in Egypt [11], Ramajama (2,000 B.C.) in India, Hippocrates (400 B.C.) in Greece and Galen (200 A.D.) in Rome, when hot irons were applied to superficial tumours as a pain palliative [12].

In 1898, Westermark found that hot water-circulation cisterns could be used to treat advanced inoperable carcinomas of the uterus and also as palliative shedding of different tumours [12].

It was the first decade of the 20th century when high frequency currents were first used in hyperthermia treatments with the research from d'Arsonval, Telsa and others [13]. Diseases such as arthritis, asthma, multiple sclerosis, syphilis and gonorrhoea were treated with hyperthermia in the early part of the 20th century [14, 15]. Later, in 1926, electromagnetic waves were first considered for cancer treatment with the research of Nagelschmidt [12].

The first clinical trials of hyperthermia in cancer patients began on the 70s and 80s [16, 17] and the first hyperthermia session at a congress was organized in 1974 by Dr. Eugene Robinson at the International Congress of Radiation Research, in Seattle, WN, USA. The following year, Robinson organized the first International Congress on Hyperthermic Oncology, in Washington, DC, USA [5, 18].

Nowadays, there are different hyperthermia societies around the globe such as the Society for Thermal Medicine (STM) [19] in the USA, the Asian Society for Hyperthermic Oncology (ASHO) [20] or the European Society for Hyperthermic Oncology (ESHO) [21]. Hyperthermia combined with radiotherapy is

one of the standard treatment approaches for patients diagnosed with locally advanced cervical cancer in the Netherlands [22]. The Atzelsberg Circle is an international working group with the endeavour of hyperthermia in clinical practice and performing clinical protocols.

2.1.3. Physics of Hyperthermia

Surgery, radiotherapy and chemotherapy are the most established cancer treatments worldwide. However, sometimes due to the patient's state of health or to the pathological characteristics of the tumour, these therapies cannot be endured or present a high risk to the patient. Surgical resection is not suitable in cases of metastases, leukaemia, or in some tumours located very close to the spine. Also, cells that present hypoxia, low pH areas, or are in the synthesis period (S-phase) are resistant to radiotherapy, and cells with insufficient perfusion are unresponsive to chemotherapy, as the drug concentration in these cells is low [5, 6].

When hyperthermia is applied to a tissue, the metabolism tries to reduce the heat generated by increasing the blood flow. When normal healthy tissue is exposed to hyperthermia the blood vessels can enlarge to facilitate an increased blood flow in the region which produces a reduction in the temperature. Tumour tissues present a chaotic vascular architecture with regions of hypoxia, low pH and lack of perfusion compared with the normal vascularity of healthy tissue. Those physiological deficiencies dictate that when tumour tissue is exposed to hyperthermia, although the blood flow is increased, tumour tissue cannot expand efficiently and its ability to increase blood flow is limited, with a consequential rise in temperature [8]. This process ensures that the temperature in the normal tissue does not increase greatly and the oxygenation and perfusion enhancement in the tumour area results in an increased acceptance of radio- or chemo-therapy respectively [5]. With a significant increase of temperature in the tumour tissue, some cells die or the tumour may shrink facilitating a surgical removal. Additionally, it has been shown that some

drugs as mitomycin C, nitrosureas, cisplatin, doxorubicin and mitoxantrone are potentiated by heat and they can counteract drug resistance [5].

A target of hyperthermia is proteins, because protein denaturation is one of the main mechanisms for cell death, which has been observed at temperatures greater than 40 °C. Some of the effects of protein denaturation are damage to the DNA repair systems and alterations to the cell membrane with the consequent higher drug concentration [5, 8].

Glucose provides energy for cell division and multiplication. This process is realized in the presence of oxygen for normal cells and as an anaerobic process for cancer cells. If oxygen is present, the ability of cancer cells to multiply will decreased [23]. The 1931 Novel Laureate Dr. Otto Warburg stated that cancer cells require 10 to 50 times more glucose than normal healthy tissue [24]. Holt's theory [23] states that hyperthermia induces cancer cells to consume certain drugs which mimic glucose, but actually they block the glucose absorption from the blood and contain oxygen (glutathione, alpha lipoic acid, etc.). This leads to a reduction of the cancer cells ability to multiply and increase the effectiveness of radio- and chemo-therapies.

2.1.4. Types of Hyperthermia Treatment

Heating techniques or hyperthermia treatments can be categorized into three broad types: local, regional or whole body hyperthermia.

Local Hyperthermia

Local hyperthermia involves the treatment of tumours up to 5 to 6 cm in the longest dimension [8]. Depending on the applicator positioning, local hyperthermia can be classified into superficial or interstitial/endocavitary.

Superficial hyperthermia involves the treatment of tumours in the skin or up to 4 to 6 cm below the skin, and it is performed with an external applicator [25]. Waveguides and microstrip antennas are common external applicators [26, 27]. Some cancers that can be treated with superficial hyperthermia

are lymph-node metastases of head and neck tumours, breast cancer, cutaneous metastases or chest wall recurrences and melanomas [7]. Gabriele *et al* [28] concludes that the combined treatment of hyperthermia and radiotherapy should be the first choice in the treatment of superficial recurrences.

Interstitial hyperthermia requires the insertion of the heat source into the tumour. The heat source can be microwave antennas, radio frequency electrodes or other types of applicators or ferromagnetic seeds [7]. Microwave antennas are inserted into catheters and then placed into the tumour [29]. Some head and neck tumours, prostate, or breast cancer are examples of tumours that can be treated with interstitial antennas. Ferromagnetic seeds are injected into the tumour tissue and then heated using a magnetic field. It can treat tumours situated in deep body regions such as the skull (recurrent glioblastoma) or pelvis (such as prostate and cervical carcinoma) [8]. Endocavitary applicators are inserted in natural openings such as the oesophagus, urethra, vagina or rectum [7]. Prostate (urethra, rectum), rectal, vaginal cervix or oesophagus are examples of cancer that can be treated with endocavitary applicators. Interstitial or endocavitary techniques can raise the tumour temperature more than external applicators and without damaging the surrounding normal tissue [16]. Thermoablation is another cancer therapy which uses invasive applicators and radio frequency. Tumour temperature is raised to over 50 °C with the consequent cellular coagulation and tissue necrosis. Tumours which can be treated with thermoablation techniques include small focal tumours located within the liver, lung, kidney or bones [8].

Regional Hyperthermia

Regional hyperthermia involves the heating of a large part of the body as the abdominal cavity, limbs or organs. When regional hyperthermia has to treat deep-seated tumours, arrays of antennas can be used. The Sigma-60 applicator is one of the most common hyperthermia array systems [30]. Advanced cervical, prostate, bladder, colorectal, ovarian, liver, stomach or some melanomas are example of tumours that can be treated with regional hyperthermia [7].

Whole Body Hyperthermia

Whole body hyperthermia is usually indicated for the treatment of carcinomas with distant metastases. Various methods such as hot water blankets, thermal chamber or infrared radiators are used. This hyperthermia treatment usually requires general anaesthesia or deep sedation. Examples of tumours which can be treated with whole body hyperthermia include melanomas, soft tissue sarcomas or leukaemia [7, 8].

2.1.5. Hyperthermia Treatment Clinical Trials

Numerous studies have shown the efficiency of hyperthermia when used in combination with radio- or chemo-therapies. Clinical trials show evidence of improved local control, improved survival and no change in morbidity when adding hyperthermia to conventional therapies [6]. Some examples of clinical trials of hyperthermia in combination with radio- or chemo-therapy are summarized in Table 2.1.

Table 2.1 shows that in a summary of the nine clinical trials evaluated there was a complete response end point mean rate of 35% for the treatments without hyperthermia while the complete response end point mean rate increased up to 60% in treatments where hyperthermia was combined with radio- or chemo-therapies. The follow up considered the survival rate and the tumour local control. The mean survival rate increased from 21% in treatments without hyperthermia to 38% in treatments with hyperthermia. The local control increased from 23% in treatments without hyperthermia to 42% in treatments with hyperthermia.

2.1.6. Medical Hyperthermia Treatment

A hyperthermia treatment takes around 5 weeks; usually it is administered once or twice per week in sessions that last around 60 to 90 minutes [22]. The temperature reached in the tumour and surrounding tissue is monitored by

Table 2.1.: Hyperthermia treatment clinical trials. N: number of patients, Freq: frequency of hyperthermia system, NDA: no data available, LC: local control, HT+RT: hyperthermia plus radiotherapy, HT+ChT:hyperthermia plus chemotherapy.

Tumour	Reference	N	Treatment	Freq [MHz]	Complete Response No HT	Complete Response With HT	Follow up No HT	Follow up With HT
Bladder	Van der Zee, 2000 [31]	101	HT+RT	433	51%	73%	23% surv at 3 years	28% surv at 3 years
Breast	Sherar, 1997 [32]	120	HT+RT	NDA	41%	61%	NDA	NDA
Cervix	Franckena, 2008 [33]	114	HT+RT	70-120	57%	83%	20% surv at 12 years	37% surv at 12 years
Head	Datta, 1990 [34]	65	HT+RT	27.12	31%	55%	19% surv at 18 months	33% surv at 18 months
Melanomas	Overgaard, 2009 [35]	70	HT+RT	144-915	35%	62%	28% LC at 2 years	46% LC at 2 years
Rectum	Berdov, 1990 [36]	56	HT+RT	915	1.7%	16.1%	6.6% surv at 5 years	35.6% surv at 5 years
Superficial	Jones, 2005 [37]	109	HT+RT	433	42%	66%	18.7% LC at 5 years	37% LC at 5 years
Bladder	Colombo, 1996 [38]	52	HT+ChT	915	22%	66%	NDA	NDA
Peritoneal	Verwaal, 2003 [39]	105	HT+ChT	NDA	NDA	NDA	39% surv at 21.6 months	56% surv at 21.6 months
Summary mean values					35%	60%	21% surv 23% LC	38% surv 42% LC

temperature sensors. Variations of those guidelines depend on the patients and treatment conditions. If radiotherapy is administered, this is delivered before or after the hyperthermia treatment. In general, it is accepted that irradiating during the heating period maximizes cell killing and as the time between hyperthermia and radiotherapy increases, the effect of improved acceptation of radiation decreases [6]. When chemotherapy is administered, it is usually delivered during the hyperthermia treatment [38].

Hyperthermia may induce in some tissues a temporary resistance to increase its temperature; this phenomenon is known as thermotolerance or thermoresistance [6]. The consequence is that when a patient is treated with hyperthermia the sessions cannot be repeated with a periodicity of less than 3 or 4 days. If this non-session period is not respected, the following session treatment can be less effective because the tumour increases the thermoresistance and more energy would be necessary to deposit inside the tissue for the same temperature increase.

2.1.7. Ultrasound and Radio Frequency Hyperthermia

While radio frequency hyperthermia (usually 27 MHz to 2.45 GHz) is the technique considered in this work, ultrasound hyperthermia (usually 100 kHz to 10 MHz) techniques have also been used in cancer treatments [40]. A penetration up to 12 cm can be obtained and as the wavelengths are small compared with their sources, good focusing can be achieved. There is no significant heating at the interfaces of fat and muscle tissues. Some disadvantages are that ultrasound waves do not propagate through air which can cause heating of interfacing tissues, organs containing air or air cavities such as lungs or stomach. There is high absorption in bones, causing overheating and pain [15].

2.1.8. Hyperthermia Treatment Planning

Hyperthermia treatment planning is a modality to design, control, document and evaluate a treatment with the aim of optimizing the treatment and increase the quality of the hyperthermia [41].

The first step of hyperthermia treatment planning is to obtain the anatomy of the area to treat with a computed tomography (CT) or magnetic resonance imaging (MRI) scan. Anatomies have to be segmented, and dielectric, temperature and perfusion properties have to be assigned. The $3D - patient$ model has to be generated and imported into the electromagnetic simulator. The applicator has to be positioned in the model and the electromagnetic distribution and temperature will be computed and optimized. The treatment will be planned. Before the hyperthermia treatment can be performed, the thermometry is positioned to monitor the treatment area. After the treatment is conduced, all the procedure and results have to be analyzed for possible future improvements.

Magnetic resonance (MR) guided hyperthermia is a hybrid system where the temperature rise produced by the hyperthermia system can be non-invasively real-time monitored by the use of the proton resonance frequency shift (PRFS) method [42]. Research is being conducted to investigate algorithms for online hyperthermia system response to MR thermal imaging [43, 44].

2.2. ISM Frequency Bands. 434 MHz

When working on medical applications which require energy deposition into tissue, the frequency selection balances improved energy penetration depths by longer wavelengths against increased antenna dimensions and focus, although larger sizes can inhibit optimal proximity positioning at concaved areas of the body.

Depending on the spectrum jurisdiction, hyperthermia applicators [9] have exploited frequencies in various Industrial Scientific and Medical (ISM) fre-

quency bands (or similar) at 27, 434, 915 and 2450 MHz. The longer wavelength of 434 MHz (λ_o= 0.690 m) has shown a more uniform specific absorption rate (SAR) distribution and a greater penetration depth than 915 MHz (λ_o= 0.327 m) [45] and 2450 MHz (λ_o= 0.122 m) [46]. Holt employed 434 MHz throughout thirty years of successful cancer treatments [47]. However, when lighter-weight, low-permittivity dielectric substrates are used for lower frequency antennas, it is usually necessary to increase the dimensions for efficient coupling from the longer wavelength resonant modes. This work is based on the frequency of 434 MHz.

2.3. Dielectric Properties of Tissues

The different water content of different body tissues determines their dielectric properties, and consequently the RF energy absorption [48]. Due to their water content, tissues are considered wet (skin and muscle) or dry (fat).

The dielectric properties of a tissue are frequency dependent. Figure 2.1 shows the relative permittivity, Figure 2.2 the conductivity and Figure 2.3 the penetration depth for skin, fat and muscle tissue in the range of frequency from 100 to 1000 MHz [49].

It is shown that the permittivity decreases with frequency for the three tissues, but the fat presents a very low permittivity with little change in frequency. Skin and muscle present greater values of permittivity with a greater reduction rate at low frequencies. The conductivity increases with frequency and again it is shown that fat tissue presents the lowest values. Skin and muscle tissue present a similar increase rate. The penetration depth, or skin depth, δ [m], is defined as the distance within a material at which the field reduces to 1/e (approximately 36.78%) of its value at the interface [50] and it can be calulated with the equation

$$\delta = \left(\frac{1}{\omega}\right)\left\{\left(\frac{\mu\varepsilon}{2}\right)\left[\left(1+p^2\right)^{1/2}-1\right]\right\}^{1/2}, \tag{2.1}$$
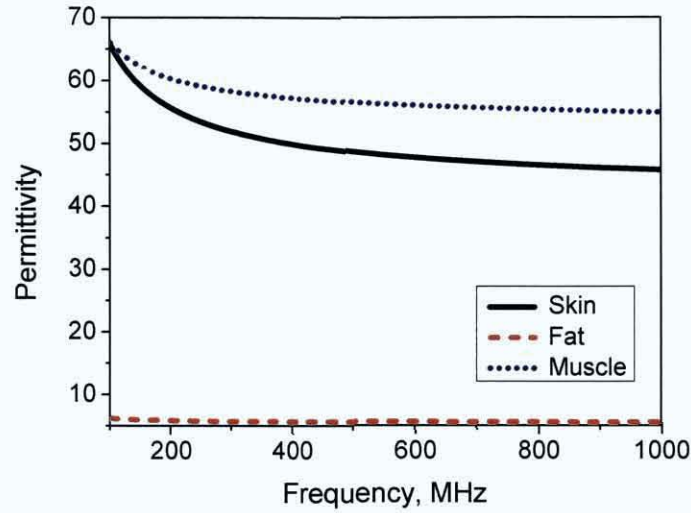
Figure 2.1.: Permittivity of skin, fat and muscle tissue.

where ω is the angular frequency [1/s], μ and ε are the permeability [N/A^2] and permittivity [$F/$m] of the tissue, $p=\sigma/\omega\varepsilon$ and σ is the tissue conductivity [S/m]. The field amplitude decays exponentially when the depth increases. The penetration depth decreases with frequency and fat tissue presents the greatest values. In this case, the rate of decrease for fat is larger than for skin or muscle tissue.

Dielectric properties of human tissue may vary significantly among patients, tissue types and during treatment [43]. Normal and tumour tissues present different dielectric properties, and in general, tumour tissue presents greater conductivity and permittivity. For frequencies between 50 to 900 MHz the differences between normal and tumour tissue for kidney were around 6% and 4% for permittivity and conductivity respectively, while for mammary gland the differences were around 233% and 577% [51].

Other benefit of using hyperthermia as a medical treatment is that hyperthermia increases the contrast between cancer and healthy tissue. Cancer tissue has enhanced energy absorption due to the higher water content with respect to their normal counterparts. A breast thermoacoustic CT of three pa-
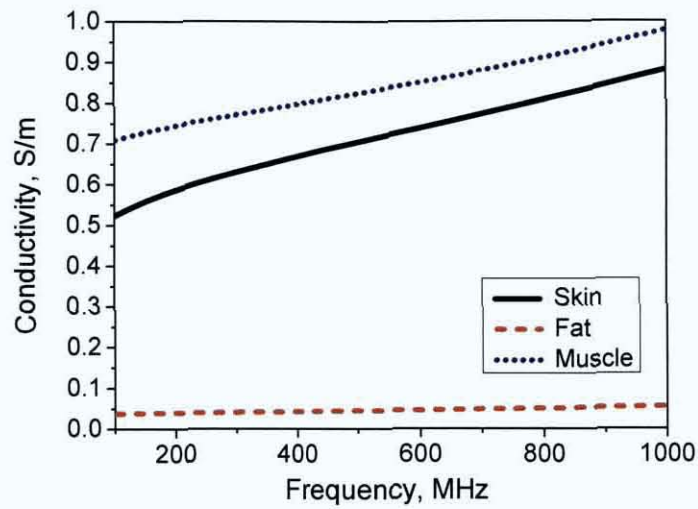
Figure 2.2.: Conductivity of skin, fat and muscle tissue.
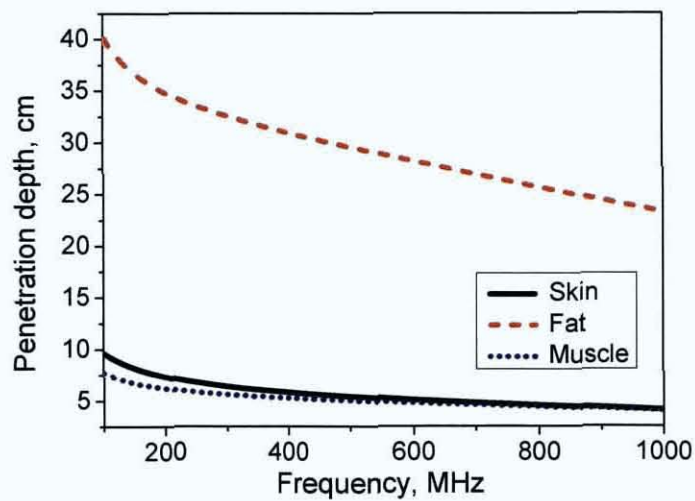
Figure 2.3.: Penetration depth of skin, fat and muscle tissue.

tients with known breast cancer showed increased energy absorption whereas no absorption enhancement was seen in two other patients who had a complete pathologic cancer remission after chemotherapy [52]. This increased contrast could facilitate tumour location and monitoring of the tumour regression with thermoacoustic CT or ultra wide bandwidth (UWB) imaging antennas.

2.4. Antenna-Human Tissue Interaction

Since the body has low permeability, the absorbing effect is principally associated with tissue permittivity losses. There are three principal ways in which energy can be transferred from an electric field to an absorbing object:

- Transfer of kinetic energy to free electrons,
- Friction associated with the alignment of electric dipoles with the internal electric field,
- Friction associated with ionic and molecular vibrational and rotational motion associated with the internal electric field.

A lossy substance absorbs electromagnetic energy when it is exposed to an electromagnetic field. The more water or other "polar" molecules a substance contains per unit volume, the greater the loss, and the drier a substance is, the less lossy it is [53].

The interaction of an E-field with a tissue is described using its complex permittivity given by the equation

$$\varepsilon = \varepsilon_0 \left(\varepsilon' - j\varepsilon'' \right), \tag{2.2}$$

where ε_0 is the permittivity of the free space, ε' (also represented by ε_r) is the real part or relative permittivity (dielectric constant), and ε'' is an indicative of the energy transferred from the incident E-field to the tissue. The larger ε'', the greater the loss in the tissue, and it can be calculated with the equation
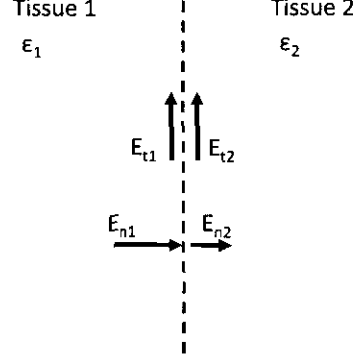
Figure 2.4.: Normal and tangential E-field representation at the interface between two tissues.

$$\varepsilon'' = \frac{\sigma}{\omega \varepsilon_0}, \tag{2.3}$$

where σ is the tissue conductivity [S/m], and ω is the angular frequency [1/s]. The E-fields can propagate between tissues and penetrate deeply into the adjacent tissue if the fields are tangential to the interface. However, the propagation is dependent on the tissue permittivity if the fields are normal to the interface. This is known as boundary conditions and it is represented with the equations

$$E_{t1} = E_{t2}, \tag{2.4}$$

$$\varepsilon_1 E_{n1} = \varepsilon_2 E_{n2}, \tag{2.5}$$

where E_{t1} and E_{t2} are the tangential field components, E_{n1} and E_{n2} are the normal field components and ε_1 and ε_2 are the permittivities, of the first and second tissue at both sides of the interface. Figure 2.4 shows a schematic representation of the tangential and normal E-fields at the interface between two tissues.

The power absorbed per unit of volume and time averaged can be described with the equation

$$P = \sigma|E|^2, \tag{2.6}$$

where σ is the tissue conductivity [S/m], and $|E|$ is the rms magnitude [V/m] of the incident E-field in a point.

2.5. Specific Absorption Rate

The specific absorption rate (SAR) is an index that quantifies the rate of energy absorption in biological tissue. It is the power absorbed per unit of volume, P, in a tissue (equation 2.6) normalized to its density to have the ratio of power absorbed per unit mass of tissue, and it is proportional to the ratio between conductivity and density of the exposed tissue as shown in the equation

$$SAR = \frac{P}{\rho} = \frac{\sigma|E|^2}{\rho}, \tag{2.7}$$

where P is the power absorbed in the tissue [W], ρ is the mass density of the medium [kg/m^3], σ is the electrical conductivity [S/m], and $|E|$ is the rms magnitude of the electric field strength vector [V/m].

The dielectric parameter values at 434 MHz for fat ($\sigma_{fat} = 0.041$ S/m and ρ_{fat}=916 kg/m^3) and muscle ($\sigma_{muscle} = 0.805$ S/m and ρ_{muscle}=1041 kg/m^3) [49] cause that the SAR in fat tissue is 5.78% of the SAR in muscle tissue for the same incident E-field. The SAR is expressed in watts per kilogram [W/kg] and it is generally quoted as a figure averaged over a volume corresponding to either 1 g or 10 g of body tissue [53].

The SAR can be determined by E-field measurements at a point, as shown in the equation 2.7 or by the rate of temperature increase as shown in equation 2.8. This is only if the measurements are made under "ideal" conditions, where the heat transfer or blood flow is not considered. This equation is not valid for in-vivo exposure conditions.

$$SAR = \frac{C\Delta T}{\Delta t},\qquad (2.8)$$

where C is the specific heat capacity of the exposed tissue [J/kg/ °C], ΔT is the change in temperature [°C], and and Δt is the exposure duration [s].

2.6. Temperature

The increase of temperature inside the human body is determined for two factors, absorbed and lost energy. The absorbed energy is a function of the frequency of operation, incident E-field, and dielectric properties of the tissue. The lost energy is a function of the generated blood flow in the tissue and the conduction of heat.

A waterbolus is a bag filled with circulating water, whose temperature can be controlled. In superficial hyperthermia, the waterbolus is positioned interfacing the skin and has the functions of enhancing the transfer of energy into the tissue and to control the skin temperature.

The Pennes bio-heat equation [54] (equation 2.9) is used to calculate the temperature rise in the exposed human tissue. Heat exchange mechanisms such as blood flow, heat conduction, metabolism heat and electromagnetic heating are considered in this equation

$$\rho C\frac{\delta T}{\delta t} = \nabla\cdot(K\nabla T) - \rho_{blood}\omega C_{blood}(T - T_{core}) + Q_m + SAR\rho,\qquad (2.9)$$

where ρ is the material density [kg/m^3], C is the specific heat capacity [J/kg/ °C], T is the variable quantity of temperature [°C] at a time t [s], K is the thermal conductivity [W/ m/ °C], ρ_{blood} is the blood density [kg/m^3], ω is the perfusion by blood [ml/100 g/ min], C_{blood} is the blood heat capacity [J/kg/ °C], T_{core} is the blood temperature [°C], Q_m is the heat generated by metabolism [W/ m^3].

The boundary condition between the body model (skin) and the surrounding air or waterbolus is given by the equation

$$K\frac{\delta T}{\delta n} = -h(T - T_A),$$

(2.10)

where δn is the vector unit normal to the skin, h is the convection coefficient [W/m²/°C] and T_A is the air (or waterbolus) temperature [°C].

The time step must be chosen based on all materials used in the calculation and is determined with the equation [55, 56]

$$\delta t \leq \frac{2\rho C \Delta_x^2}{12K + B\Delta_x^2},$$

(2.11)

where Δ_x [m] is the smallest cell size in the geometry, and B is the blood flow constant [W/m³/°C] which is determined with the equation

$$B = \frac{\omega \rho_{blood} C_{blood}}{6000}$$

(2.12)

The simulation platform initially solves the Pennes bio-heat equation (equation 2.9) without considering the external sources, only as the metabolism heats the tissue and the blood flows to cool the tissue. This process is iteratively repeated until a steady state is reached.

The temperature of the tissues at the steady state would be considered as the baseline. Then, the Pennes bio-heat equation is solved again considering the absorbed energy with the SAR term. The temperature rise is the difference between the calculated temperature or baseline and the temperature with the addition of the SAR term [56].

In order to properly control the treatment, the temperature inside the tumour has to be monitored. To monitor this internal temperature, usually microthermometers are inserted through the skin into the tumour [16]. However, the probability of metastases developing might increase with the disruption of blood vessels if probes are inserted into the tumour or the heat is delivered invasively.

2.7. Modeling and Simulations

The commercially available electromagnetic simulators CST MWS [57] and XFDTD [58] were used to model the antennas and the body anatomies. Both simulators provide a user-friendly computer aided design (CAD) environment to generate the different geometries. CST is based on the Finite Integration Technique (FIT) whereas XFDTD is based on the finite difference time domain method (FDTD).

Both FIT and FDTD are time domain solutions of Maxwell's equations whose origins can be traced in the work of Yee in 1966 [59]. The FIT was first proposed by Weiland in 1977 [60] and the FDTD was proposed by Taflove in 1980 [61]. In both methods the entire computational domain is divided into cells that form the mesh. The equations in integral and differential form are solved in the FIT and FDTD method respectively, to calculate the field on the edges of each mesh cell. While manual subgriding has to be used in the FDTD method to improve the accuracy at the boundaries, adaptive automatic meshing is provided with the FIT method.

3. Hyperthermia Antenna Development

Different antennas have been employed for medical use, both for diagnostic and/or therapeutic applications. A novel compact patch antenna for hyperthermia applications has been developed and the design evolution is presented.

In this chapter antennas for medical applications and hyperthermia antenna design requirements are introduced. While there are increasingly sophisticated hyperthermia systems, this work is focused on a single applicator, which is low cost and easy to manufacture. Pursuing the requirements criteria, a compact patch antenna is developed. The design evolution and analysis of the feed point location, E-field and SAR distribution are presented. The antenna groundplane features and actual antenna geometry are depicted. In this chapter the geometry of the antenna is presented, while the next chapter compares the proposed antenna with clinically used and previously published applicators.

3.1. Antennas for Medical Applications

The use of antennas in medical applications [62], tissue parameters analysis [63] and epidemiological studies has been the research topic of many investigators in the last few years [64]. The main requirement in many medical applications

is that the electromagnetic energy is coupled into deeper tissues of the body without damaging the skin and superficial tissues [65]. Energy deposition can penetrate deeper at low frequency (see Section 2.3) but the large wavelength produces that energy cannot be localized to small areas and consequently, large regions are heated. At low frequencies, the applicator will be electrically small if its physical size is manageable, and the near-field can overheat the superficial tissues.

Medical application antennas can be classified into two groups: information transmission and therapeutic antennas. Radio frequency identification (RFID), wearable or implantable monitors, magnetic resonance imaging (MRI) and microwave imaging for breast cancer detection are some of the most investigated information transmission applications. Various waveguide and horn apertures have been used in microwave imaging systems [65]. Thermal therapy such as hyperthermia or thermoablation are some of the therapeutic applications.

Hyperthermia antennas can be classified into non invasive and invasive [65]. Non invasive or not penetrating antennas can be classified into E-type, H-type and radiative applicators. E-type applicators mainly produce electric fields that heat the tissue. Capacitor plates are examples of E-type applicators [66]. These applicators operate at the relatively low frequencies of 13.56 MHz or 27.12 MHz and can heat deep tissue but they produce large normal field components which can overheat the superficial and interfacing tissues. H-type applicators primarily produce a magnetic field, which in turn induces the E-field that heats the tissue. Coaxial current loops are examples of H-type applicators [67]. Eddy currents circulate around the axis of the loop and the heating in the centre is very small. Relatively high currents are usually needed to get adequate heating, but the advantage over E-type applicators is that they produce tangential E-field components which prevent overheating of superficial and interfacing tissues. Waveguide and microstrip antennas are very common radiative applicators. Waveguides are simple and can be loaded with dielectric to improve the impedance matching, but for compactness and weight, mi-

crostrip applicators have a fundamental advantage. Invasive or intracavitary applicators can efficiently heat specific locations but the intrusive nature is not practical for all tumours. Coaxial antennas are inserted into a catheter to avoid the contact between the antenna and the tissue, and then located inside the tumour mass [29, 68]. Ferromagnetic particles can be injected into the tumour tissue and if they are stimulated with an alternating magnetic field they produce heat due to Brownian and Neel relaxation process. This approach can be specially indicated for deep-seated and poorly accessible tumours [69].

3.2. Hyperthermia Antenna Requirements

Distance related losses (DRL) and mismatch losses (ML) are two limitations that need to be considered when working with antennas for medical applications. The antenna has to be close to the tissue to have the minimum possible DRL and provide the highest amount of energy into the tissue. On the other hand, the antenna normally has to be far from the tissue to have the minimum possible ML and detuning the antenna operating frequency [70]. The human body presents a high permittivity complex load (variable tissues of different dielectric properties) to an antenna when located in its near-field and can detune the antenna from the system frequency and impair the coupling performance. In practical clinical applications selecting the appropriate distance between antenna and human body is a critical task.

An antenna that remains sufficiently matched to the source frequency during unloaded and variably-loaded conditions can simplify the overall system stability [62]. The applicator will be suitable for various tissue loads while the system source, typically $50 - 60\,$dBm, will have reduced vulnerability to destructive power reflections. Conventional applicators exhibit tissue-dependent or distance-dependent matching performance. A suitable hyperthermia applicator has to provide good matching without detuning from the operational resonant frequency.

Deeper energy deposition requires low frequency of operation. The frequency of operation is inversely proportional to the antenna size. This compromises the suitability of the antenna to treat tumours located in curved sites of the human body and the antenna efficiency when miniaturizing the geometry. The antenna must couple well with tissue despite its small size. In order to produce elevated temperatures, the applicator has to generate high SAR at the required depth in tissue, and in order to limit overheating of the superficial tissues and tissue interfaces, the applicator should produce tangential E-fields that can be transferred from one interface to the next.

An unbalanced input connection to the antenna facilitates simple feed systems as they do not require balanced-to-unbalanced (balun) transitions which can increase volume and incur loss [70]. In order to facilitate manageability in a clinical environment the applicator has to be low weight, low cost and easy to manufacture. Reducing the complexity of the hyperthermia system can facilitate its use by non antenna experts clinicians.

Knowing that the effect of the human body can change the performance of the antenna, strategies are needed to maintain the detuning resilience at the resonant frequency. The antenna network matching impedance [71] is dependent on antenna-to-tissue distance, waterbolus dimensions, human body region and patient anatomy. Dielectric stepped impedance has been previously reported [72], but this method increases the weight, volume and cost of the hyperthermia system. If the applicator operational band can be increased, the detuning becomes less of an issue as long as the detuned band is still within the system resonant frequency [73]. Using geometries which allow distance-dependent mode changes to occur can facilitate current paths for different loading conditions without detuning the operational frequency. For wire antennas with only one possible current path (i.e. dipole or loop) this is not possible.

3.3. Compact Patch Antenna

3.3.1. Compact Patch Antenna Design Steps

The basic element chosen for the antenna design was a microstrip patch antenna. Different miniaturization, input impedance and bandwidth enhancement techniques have been used in the design of the proposed applicator. The antenna was initially designed in free space conditions, and later optimized next to a waterbolus interfacing simulated human tissue.

Initially, the antenna evolved from a circular patch to an annular ring patch antenna. The circular patch antenna presents a fundamental resonant frequency of [74]:

$$f = \frac{1.8412 c_0}{2\pi a_e \sqrt{\varepsilon_r}},$$ (3.1)

$$a_e = a_{CP} \left[1 + \frac{2h}{\pi a_{CP} \varepsilon_r} \left(\ln\left(\frac{\pi a_{CP}}{2h}\right) + 1.7726 \right) \right]^{1/2},$$ (3.2)

where c_0 is the speed of the light in the vacuum, ε_r is the dielectric constant of the substrate, h is the substrate thickness [cm], a_e is the effective radius to account the fringing that makes the patch look electrically larger [cm], and a_{CP} is the physical radius of the circular patch [cm].

The fundamental resonance frequency for the annular ring patch antenna can be calculated with [75]:

$$f = \frac{c_0 k}{2\pi \sqrt{\varepsilon_{reff\_ann\_ring}}},$$ (3.3)

$$k = \frac{2}{a_{ARP} + b_{ARP}},$$ (3.4)

$$\varepsilon_{reff\_ann\_ring} = \frac{\varepsilon_r + 1}{2} + \frac{\varepsilon_r - 1}{2} \left[1 + 12 \frac{h}{b_{ARP} - a_{ARP}} \right]^{-1/2},$$ (3.5)
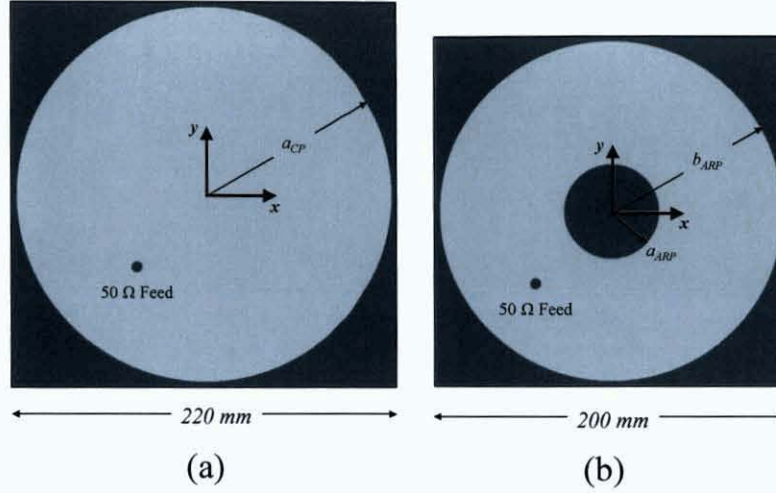
Figure 3.1.: Geometry of the (a) circular patch and (b) annular ring patch antenna.

where $\varepsilon_{reff\_ann\_ring}$ is the effective dielectric constant, and a_{ARP} [cm] and b_{ARP} [cm] are respectively the inner and outer radius of the annular ring patch.

Figure 3.1 shows the geometry of the simulated circular and annular ring patch antennas resonant at 434 MHz. The antennas are modelled on Taconic RF 35 ($\varepsilon_r = 3.5$) dielectric substrate of thickness $h = 2.97$ mm. The ground-plane extends beyond the outer radius of the circular patch and annular ring models by 3 mm.

The conventional circular patch antenna has the specifications: a circular patch radius, a_{CP}, of 107 mm and a groundplane length of 220 mm. The conventional annular ring patch antenna has the dimensions: an annular ring patch inner radius, a_{ARP}, of 27 mm, an annular ring patch outer radius, b_{ARP}, of 97 mm and a groundplane length of 200 mm. The feed point is located at the rectangular coordinates $x = y = -20$ mm for both antennas. The area of the annular ring antenna is 17.35% smaller than the area of the circular patch.

Loading the annular ring with a circular patch as shown in Figure 3.2 (a) further reduces the circular patch area up to 23.83%, however this antenna is

192 mm

130 mm

(a)   (b)
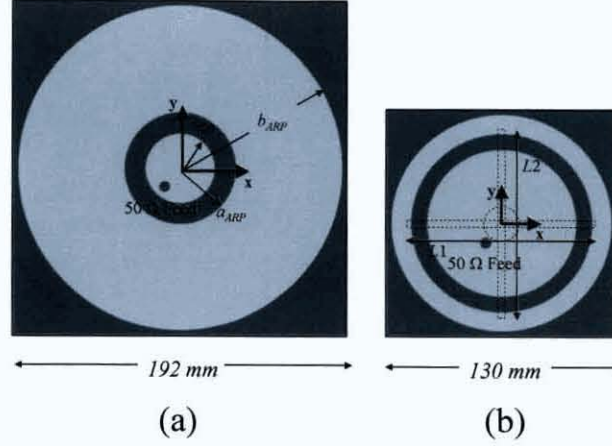
Figure 3.2.: Geometry of the (a) annular ring with concentric circular patch
and (b) annular ring with concentric circular patch and ground-
plane slots antenna.

difficult to match to $50\,\Omega$ input impedance without a feeding network. The
dimensions of this antenna are: an annular ring patch inner radius, a_{ARP},
of $32\,\text{mm}$, annular ring patch outer radius, b_{ARP}, of $93\,\text{mm}$, circular patch of
radius, c_{CP}, $20\,\text{mm}$ and a groundplane length of $192\,\text{mm}$.

The addition of a crossed slot and a circular slot in the groundplane as shown
in Figure 3.2 (b) was the next step in the antenna evolution. The crossed
slot forces the surface current to be meandered and affords an antenna area
reduction of 65.08% with respect to the conventional circular patch. Not only
do the crossed slots in the groundplane enable miniaturisation, but they also
provide wide bandwidth and resilience to proximity detuning. The circular slot
improves the antenna input impedance. A detailed geometry of this proposed
applicator is presented in Section 3.4.

The general annular ring dimensional design strategies are that increasing
the outer radius of the annular ring produces a reduction of the resonant fre-
quency and improves the matching, while enlarging the inner radius of the
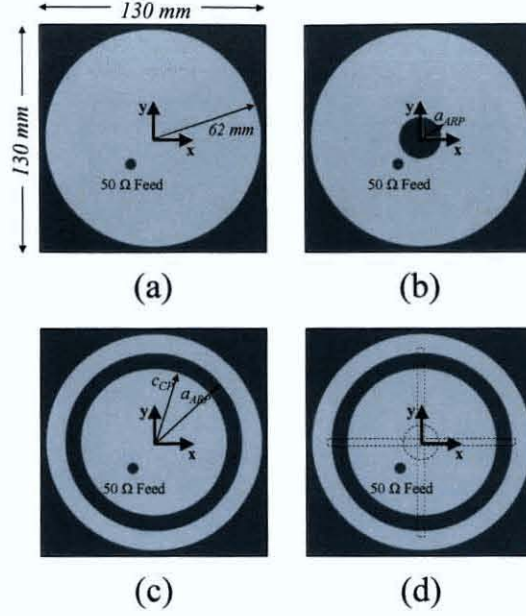
Figure 3.3.: Antenna evolution progress. (a) Circular patch, (b) annular ring, (c) annular ring with concentric circular patch and (d) annular ring with concentric circular patch and groundplane slots antenna.

annular ring reduces the resonant frequency but degrades the antenna matching. Increasing the circular patch radius improves the matching but increases the resonant frequency.

Figure 3.3 shows the antenna miniaturization evolution process considering a 130 mm × 130 mm groundplane, circular patch or annular ring outer radius of 62 mm and feed point located at the rectangular coordinates $x = y = -10$ mm. Figure 3.3 (a) presents the circular patch antenna. Figure 3.3 (b) shows the annular ring geometry with an annular ring patch inner radius, a_{ARP}, of 12 mm. Figure 3.3 (c) presents the annular ring applicator of dimensions: an annular ring patch inner radius, a_{ARP}, of 51 mm and a circular patch of radius, c_{CP}, 42 mm. Figure 3.3 (d) presents the annular ring applicator with concentric circular patch and rectangular and circular slots in the groundplane.
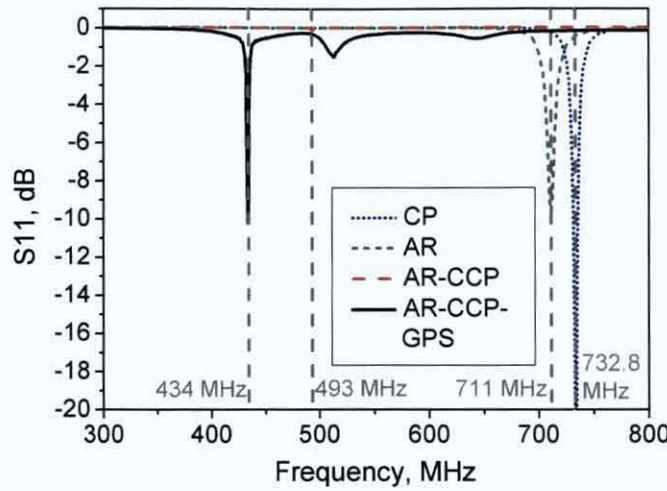
Figure 3.4.: Simulated free space S11 for the different models of the minia-
turization evolution. CP (circular patch), AR (annular ring),
AR-CCP (annular ring with concentric circular patch), AR-CCP-
GPS (annular ring with concentric circular patch and ground-
plane slots) antenna.

The S11 of these progressively more complex models (Figure 3.3) is shown
in Figure 3.4. The circular patch antenna presents a resonant frequency of
732.8 MHz. When the circular patch evolves into an annular ring the reso-
nant frequency decreases by 3%. If a concentric circular patch is added at
the annular ring geometry the resonant frequency decreases by 32.72% of the
circular patch resonant frequency. Adding a crossed slot and a circular slot in
the groundplane further reduce the resonant frequency by 40.77%.

3.3.2. Feed Location, E-field and SAR Analysis

Further analysis shows that in the annular ring with concentric circular patch
and groundplane slots antenna, locatin the feed point in the annular ring as
opposed to locating the feed in the circular patch produces different antenna
performance, improving the matching and broadening the bandwidth for both
the free space and tissue-loaded condition. The free space S11 of the two
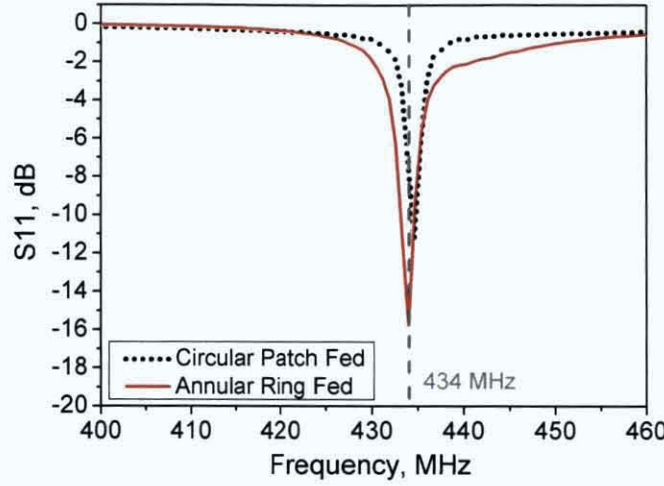
Figure 3.5.: Simulated free space S11 for the AR-CCP-GPS antenna with circular patch fed and annular ring fed.

approaches with circular patch feed at the rectangular coordinates $x = y = $ -10 mm and annular ring feeding at the rectangular coordinates $x = y = $ -40 mm is shown in Figure 3.5.

The S11 at 434 MHz is -11.21 dB (with a -6 dB bandwidth from 433.57 to 435.17 MHz, 0.36%) for the circular patch fed (CPF) antenna and -15.78 dB (with a -6 dB bandwidth from 432.41 to 435.24 MHz, 0.65%) for the annular ring fed (ARF) antenna. The ARF antenna presents a real part of the input impedance between 37 and 57 Ω across the -6 dB bandwidth, while for the CPF antenna the minimum input impedance is 72 Ω.

As the operational situation of this antenna is to work in close proximity to human tissue and produce tangentially aligned E-fields to increase penetration and prevent overheating superficial or interfacing tissue, the two antenna feed approaches were evaluated when the antenna was loaded with simulated human muscle tissue at 2.7 mm $(\lambda_0/256)$ from the antenna. The S11 (Figure 3.6) at 434 MHz is -5.58 dB (with a -6 dB bandwidth from 401.1 to 432.5 MHz of 7.53%) for the CPF antenna and -7.69 dB (with a -6 dB bandwidth from 424.1 to 480.8 MHz 12.53%) for the ARF antenna.
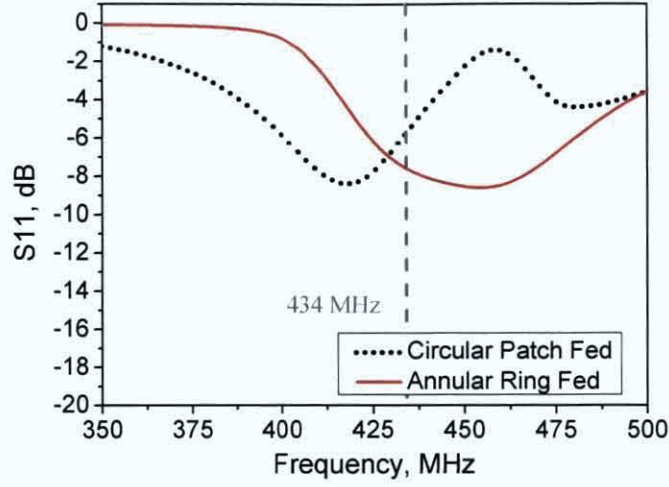
Figure 3.6.: Simulated S11 for the AR-CCP-GPS antenna with circular patch
fed and annular ring fed when located at 2.7 mm from simulated
muscle tissue.

Figure 3.7 and Figure 3.8 show the tangential E-field and SAR distribution
cross-section for the circular patch and annular ring patch antennas for 2.7 mm
antenna-tissue distance normalized to 1W of antenna input power. The cross-
section corresponds with a plane through the feed point and antenna centre.

The circular patch fed antenna produces a tangential E-field distribution
with two hot spots near the surface. However the annular ring fed antenna
generates a tangential E-field distribution focused at the patch centre and
achieves the highest coupling penetration into the tissue. Evidence of some
reflection from the far tissue boundary can be seen in Figure 3.7.

The circular patch fed antenna SAR distribution (Figure 3.8 (a)) is charac-
terized by large values at the superficial tissues with two hot spots on deeper
tissues. The annular ring fed antenna (Figure 3.8 (b)) presents a low SAR dis-
tribution on the superficial tissues with SAR concentrated and focused at the
patch centre for deeper tissues. At superficial tissues larger SAR is achieved
with the circular patch fed antenna and at deeper tissues enhanced SAR is
attained with the annular ring fed antenna. The 1 g averaged spatial peak
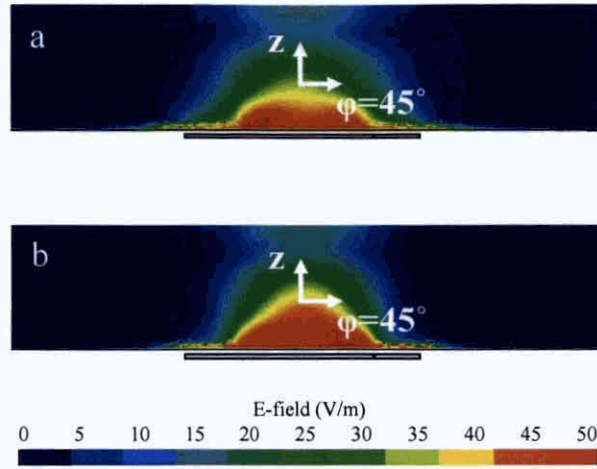
Figure 3.7.: Tangential E-fields cross-section for the AR-CCP-GPS antenna for 2.7 mm antenna-tissue distance and through the feed point and the antenna centre for (a) circular patch fed and (b) annular ring fed antenna.
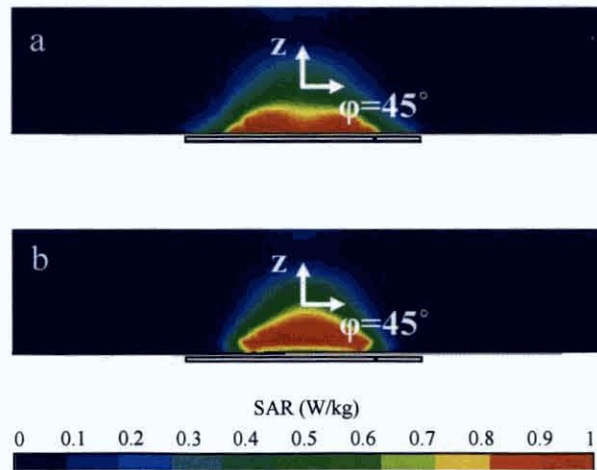
Figure 3.8.: SAR cross-section for the AR-CCP-GPS antenna for 2.7 mm antenna-tissue distance and through the feed point and the antenna centre for (a) circular patch fed and (b) annular ring fed antenna.
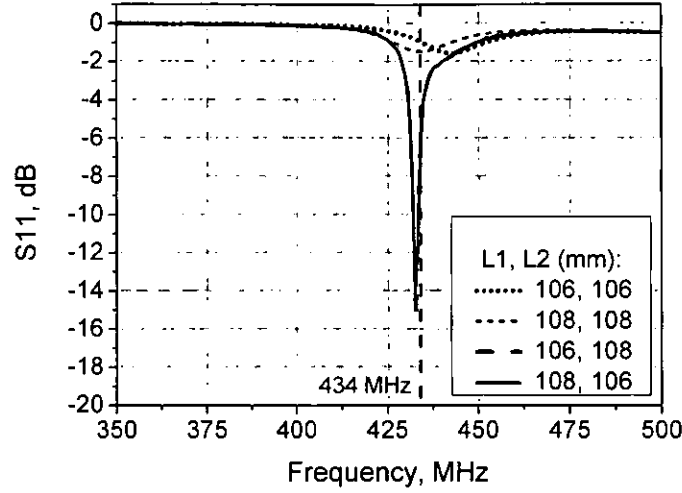
Figure 3.9.: Simulated free space S11 for the AR-CCP-GPS antenna with different groundplane crossed slot lengths ($L1$ and $L2$).

SAR is 1.39 W/kg and 2.03 W/kg for the circular patch fed and the annular ring patch fed antenna, respectively.

3.3.3. Crossed Slots Dimensions Analysis

A parametric study of the crossed slots showed that the optimum dimensions for $L1$ and $L2$ are 106 mm and 108 mm, respectively. Figure 3.9 shows the free space S11 of the antenna for different combinations of $L1$ and $L2$. When the slots have equal length of 106 mm the antenna detunes to 443 MHz with very poor matching. When the slots have equal length of 108 mm, the antenna resonant frequency is at 434 MHz with again very poor matching. Offsetting the slots lengths ($L1 = 106$ mm and $L2 = 108$ mm or $L1 = 108$ mm and $L2 = 106$ mm) produces a phase difference on the slot tip currents and enhances the antenna matching at the 434 MHz resonant frequency.
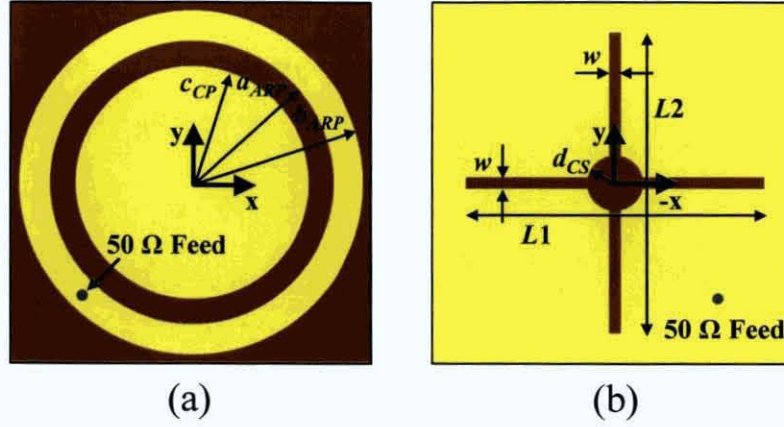
Figure 3.10.: Proposed compact patch AR-CCP-GPS antenna (a) the front annular-ring/patch surface and (b) the rear groundplane/slots surface.

3.4. Geometry of the Proposed Compact Patch Antenna

The proposed compact patch antenna geometry is shown in Figure 3.10. This applicator comprises a circular patch of radius c_{CP}, a concentric annular ring of inner radius a_{ARP} and outer radius b_{ARP}, on 130 mm × 130 mm × 2.97 mm of Taconic RF 35 dielectric substrate ($\varepsilon_r = 3.5$). The groundplane extends to the four edges and has two rectangular slots, of width w, that intersect an impedance matching circular slot, of radius d_{CS}, positioned concentrically behind the circular patch. The rectangular slots have unequal lengths $L1$ and $L2$. The optimized dimensions are: $c_{CP} = 42$ mm, $a_{ARP} = 51$ mm, $b_{ARP} = 62$ mm, $d_{CS} = 10$ mm, $L1 = 106$ mm, $L2 = 108$ mm, $w = 4$ mm. The 50 Ω feed is in the concentric annular ring at the rectangular coordinates $x = y = -40$ mm and the centre of the circular patch coincides with the coordinate origin.

The antenna frequency is adjusted by coupling resonant currents on the circumferences of the circular patch and the annular ring. The orthogonal

groundplane slots disrupt the resonant currents on the circular patch and an-
nular ring to reduce the overall patch dimensions. Offsetting the slot lengths,
$L1$ and $L2$, increases the bandwidth, and broadening the slot widths, w, re-
sults in a second-order enhancement for the Q-factor. The lengths and width
of the slots were iteratively optimized to prevent mismatch and for antenna
resonant frequency stability when in free space and when loaded with tissue.

Positioning the feed point in the annular ring matches the antenna with
$50\,\Omega$ and creates a SAR pattern that converges concentrically as opposed to
locating the feed in the circular patch, which produces a lower and diverging
SAR distribution.

3.5. Conclusions

Antennas for medical applications with emphasis on hyperthermia antenna
types have been introduced in this chapter. The design of a novel compact
patch for superficial hyperthermia treatment has been described. The evolu-
tionary process of the proposed antenna has been described following the de-
sign criteria. Starting from the conventional circular patch antenna, evolving
into an annular ring and subsequent annular ring with embedded concentric
circular patch, the proposed compact patch antenna has been designed and
developed. The proposed compact patch antenna area is 34.92% of the size of
the conventional circular patch applicator. The design overcomes the geomet-
rical constraints of other applicators. An analysis of the feed point location in
terms of matching, E-field and SAR distribution shows that locating the feed
point in the annular ring patch as opposed to the circular patch improves the
matching, produces deeper tangential E-fields into the tissue located at close
distances from the antenna, and generates greater and focused SAR aligned
with the antenna patch centre. In the next chapter, the compact patch an-
tenna is assesed with other previously published approaches and loop, dipole
and square patch antennas in terms of energy deposition into the tissue.

4. Compact Patch Antenna Assessment

$\mathbf{S}$INGLE element loop, dipole and conventional square patch antennas have been used as hyperthermia applicators in the treatment of cancerous human cells at superficial depths inside the body.

In this chapter, the performance of the novel compact patch antenna, which geometry was presented in the previous chapter, is assessed with that of the loop, dipole and conventional square patch when the antennas are located at very close proximity to a body tissue numerical model. The compact patch antenna produces an enhanced specific absorption rate pattern without significant frequency detuning or impedance mismatch. For computation efficiency and clarity in the synthesized hyperthermia treatment conditions, simplified planar tri-layered tissue models interfaced with a waterbolus are used to study the permittivity loading on the antennas and the resultant specific absorption rates.

4.1. Introduction

A patient's sensitivity to contact pressure by an applicator relates to the severity of the tumour growth and their tolerance is increased if the device is lightweight. Similarly, smaller antenna dimensions allow a better fit to concave anatomical areas and can minimize power loss due to separation distance from

the tumour region. When in close proximity to a patient, the antenna performance is dependent on several influences. The waterbolus [26, 76, 77] and the patient's tissue [78, 79] impose a bulk load of high permittivity on the antenna's radiating near-field regions. The thicknesses and depths of the constituent skin, fat and muscle layers in human tissue alter considerably across the body and among patients [80–82].

While hyperthermia array applicators [70, 83] with sophisticated control systems [84, 85] offer advanced targeting for treating different cancers, a range of complementary single element designs continue to offer simple solutions [86]. Various 434 MHz single element applicator types have been reported and $1/e^2$ (13.53%) of the peak SAR or temperature values are used to compare the penetration depths for the following references. The theoretical penetration depth due to a 120 mm × 160 mm dielectrically loaded waveguide aperture was ∼53.8 mm in [87]. By substituting the dielectric with water to overcome tissue hotspots close to the aperture, an applicator size was further reduced to 28 mm × 56 mm and achieved ∼33 mm penetration depth [88]. While the aperture efficiency of these approaches its desirable, the cumbersome dimensions of practical implementations would also have to be considered. The deposited energy area was enhanced by a 100 mm × 100 mm flared horn aperture with dielectric inserts and while applicator volume and weight remained large, the penetration depth improved to ∼36 mm [26]. The analytical optimization of a 90.3 mm × 125.5 mm water-loaded modified box-horn in [46] further enhanced the SAR penetration depth to 40.1 mm but increased the applicator volume.

Microstrip solutions offer several ergonomic advantages over waveguide and horn approaches [89, 90]. A 434 MHz microstrip shorted loop on a circa 87 mm groundplane with 3.2 mm profile was optimized for ∼28 mm penetration depth [27]. To reduce an applicator size, a higher permittivity design resulted in a rectangular printed patch on a 50 mm × 70 mm × 25 mm, $\varepsilon_r = 80$ substrate [91] with a similar penetration to [27]. A 5.5 mm profile microstrip applicator with a 150 mm × 160 mm dipole-like radiator produced a larger aperture of tangential E-fields and a penetration depth of ∼14 mm [86].

The dominant energy deposition patterns due to applicators in [26, 27, 91–94] are considered with homogeneous body tissue numerical models but the effects of superficial hotspots due to inhomogeneous models with fat layers should not be discounted [87]. Tri-layered skin-fat-muscle tissue models with fixed layer thicknesses [46, 88] have provided further detail but do not quantify the effects for the range of layer thickness in human tissue.

The novel 434 MHz compact patch antenna which geometry was presented in the previous chapter contains the shapes of a loop, dipole and square patch designs. The simulated analysis contrasts the compact patch with these basic antenna elements and the applicator performances are assessed with SAR > 0.5 W/kg for variable skin-fat-muscle tissue layer thicknesses. The frequency detuning due to different separation distances from the load is also considered. The proposed compact applicator remains ergonomically shaped while it achieves a deeper SAR penetration than the aforementioned referenced designs and is insensitive to variations in tissue layer thicknesses and to variations in the proximity from the tissue models.

4.2. Materials and Methods

4.2.1. Antenna Geometries

Despite being optimized for unloaded far-field performance at 434 MHz, treatment clinics have successfully used loop [47, 95], dipole [83] and conventional square patch [96] applicator designs. In this chapter the performance of those previously published applicators is assessed with the proposed compact patch antenna whose geometry was described in the previous chapter.

The full-wavelength wire loop antenna dimensions are a loop inner radius of 113.5 mm, a loop outer radius of 115.5 mm and a feed gap of 1.8 mm. The half-wavelength wire dipole antenna has the specifications: a wire length of 324.8 mm, a wire radius of 1.0 mm and a feed gap of 1.8 mm. The half-wavelength square patch antenna [74] has the dimensions: a patch length of

182 mm and a groundplane length of 232 mm on Taconic RF 35 ($\varepsilon_r = 3.5$) dielectric substrate of thickness 2.97 mm. The radiating patch and groundplane are centered on the origin of the rectangular coordinate system and the offset feed point is located at $x = 0$, $y = 37.5$ mm.

When loaded by the tissue models, the 434 MHz resonant lengths on the loop and dipole wire antennas become shorter than the mechanical (free space) dimensions. Consequently, their effective electrical lengthening produces anti-phased current reflections that superimpose on the shortened resonances to reduce the radiating efficiency. To repair the radiating efficiency of the wire antennas next to the tissue loads, the shortened loop and dipole antennas were also compared. The short-loop inner radius is 76.5 mm and outer radius is 78.5 mm. The short-dipole length is 239 mm and both geometries have a feed gap of 1.8 mm.

4.2.2. Waterbolus and Body Tissue Numerical Model

Parameters for inhomogeneous body tissues are defined [97] and whole-body electromagnetic models with highly resolved and detailed subterraneous geometries [98, 99] exist for in-silico analysis [100]. To minimize computational resources and for clarity, a tri-layered tissue model was used. The inhomogeneous planar tissue model represents the skin, fat and transverse fiber of muscle [101] and a waterbolus containing de-ionized water was added at the skin interface for superficial tissue cooling. The model dielectrically loads the antenna fields and renders the principal SAR pattern due to the coupled energy. Table 4.1 details the dielectric parameters of relative permittivity (ε_r), conductivity (σ S/m) [49] and density (ρ kg/m^3) [102] at 434 MHz. The square side dimension of the waterbolus and tissue model was 458 mm ($5 \times \lambda_m$), where λ_m is the wavelength inside the muscle. The thickness of the tissue models was limited to 100 mm, since the muscle layer depth had sufficient losses to discount reflections that would otherwise occur from inhomogeneous features in full body numerical models [101].

4. Compact Patch Antenna Assessment

Table 4.1.: Permittivity, conductivity, density and thickness of tissue material for 434 MHz.

	Permitivity $[\varepsilon_r]$	Conductivity $[\sigma,\ S/m\ ]$	Density $[\rho,\ kg/m^3]$	Body tissue layer summed to 100 mm thickness [mm]					
Water	76.00	0.001	1000	5.0	5.0	5.0	5.0	5.0	5.0
Skin	46.05	0.702	1100	0.4	0.4	0.4	2.6	2.6	2.6
Fat	5.566	0.041	916	0	15	30	0	15	30
Muscle	56.86	0.805	1041	99.6	84.6	69.6	97.4	82.4	67.4

For all body regions, the skin thickness ranges from minima at the thorax, abdomen, spine and limbs in children to maxima at the adult thorax [82]. In this study, the lower and upper limit skin layer thicknesses of 0.4 mm and 2.6 mm were considered. If obese conditions are disregarded, fat storing adipose tissue thicknesses range from 0 mm to 23.2 mm [80]. To account for greater variations [103], fat layer thicknesses of 0 mm, 15 mm and 30 mm were evaluated. The waterbolus was 5 mm thick. Figure 4.1 shows a schematic representation of the antenna and the layered tissue model.

4.2.3. Methodology

The key performance criterion for the antennas is the efficient transfer of energy into the layered tissue models. The antenna input impedances, resonant surface currents and the electric near-fields were analyzed to interpret the basis for the SAR responses due to the four basic applicator types. Practical distances between the antenna and waterbolus which corresponded with fractional wavelengths were selected. Evaluation studies for all of the antennas were made at 43.2 mm ($\lambda_0/16$), 10.8 mm ($\lambda_0/64$), 8.1 mm ($3\lambda_0/256$), 5.4 mm ($2\lambda_0/256$) and 2.7 mm ($\lambda_0/256$) with each of the various combinations of tri-layered tissue thicknesses which are summarized in Table 4.1.

Using a 3.4 GHz PC with 4 Gbytes of RAM, the applicator geometries were modelled in CST MWS [57]. Memory requirements ranged from 224 Mbytes for
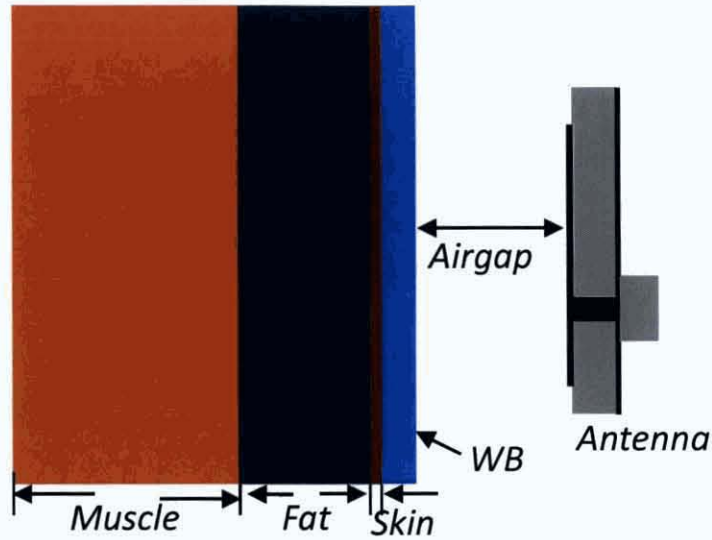
Figure 4.1.: Anntenna and layered tissue model.

the dipole near the waterbolus and body tissue numerical model combination to 551 Mbytes for the square patch. Figure 4.2 illustrates good agreement between the numerical and measurement result for the compact patch when placed 5.4 mm from a load consisting of a waterbolus and homogeneous 10 g/l saline solution liquid [70].

4.3. Results and Discussion

The illustrated results are a review of the experiments that investigate the modelling accuracy and compare the different antenna types by considering the frequency detuning and matched impedance stability, the patterns of electric field intensity and the resultant specific absorption rate patterns, normalized to 1 W of antenna input power. Figure 4.3 – Figure 4.9 show the tissue loading conditions in the various parameter studies due to an intermediate dimensioned body tissue numerical model with 2.6 mm skin, 15 mm fat and 82.4 mm muscle.
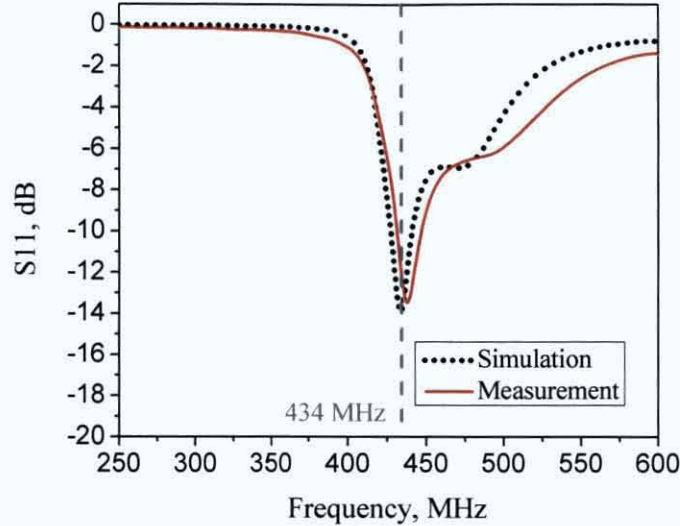
Figure 4.2.: Simulated and measured S11 with homogeneous 10 g/l saline solution liquid for the compact patch antenna.

4.3.1. Matched Impedance

The S11 simulations in Figure 4.3 – Figure 4.4 are used to compare the antennas for frequency detuning stability and their matched impedance. The antenna-waterbolus distance of 43.2 mm does not significantly detune the free-space dimensioned antennas from 434 MHz but the short-loop and short-dipole resonate at frequencies that are too high. The impedance match of the compact patch resonant frequency remains sufficient stable when the separation distance is reduced by a small wavelength fraction of 40.5 mm ($\lambda_0/17$) to 2.7 mm. The other antenna designs exhibit a higher sensitivity to this change in permittivity loading.

4.3.2. Electric Field Patterns

The electric field patterns for the different antenna types at 2.7 mm distant from the waterbolus and tissue model are shown in Figure 4.5. In the case of
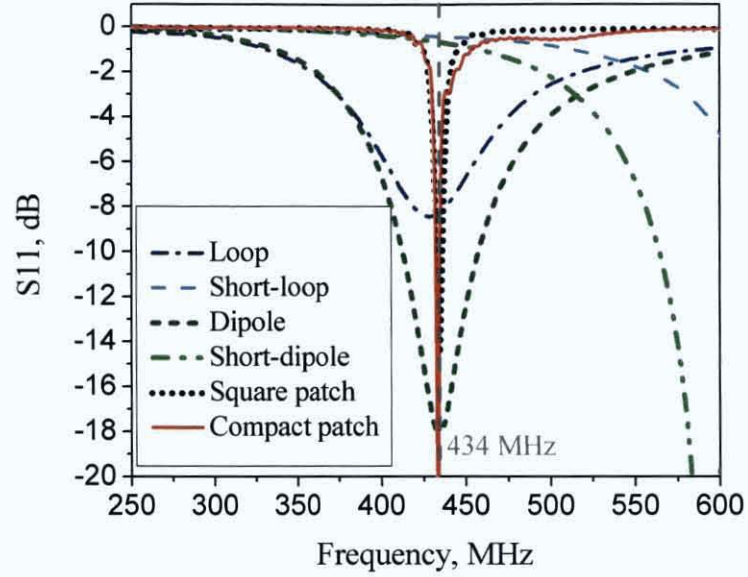
Figure 4.3.: Simulated S11 for 43.2 mm antenna-waterbolus distance.
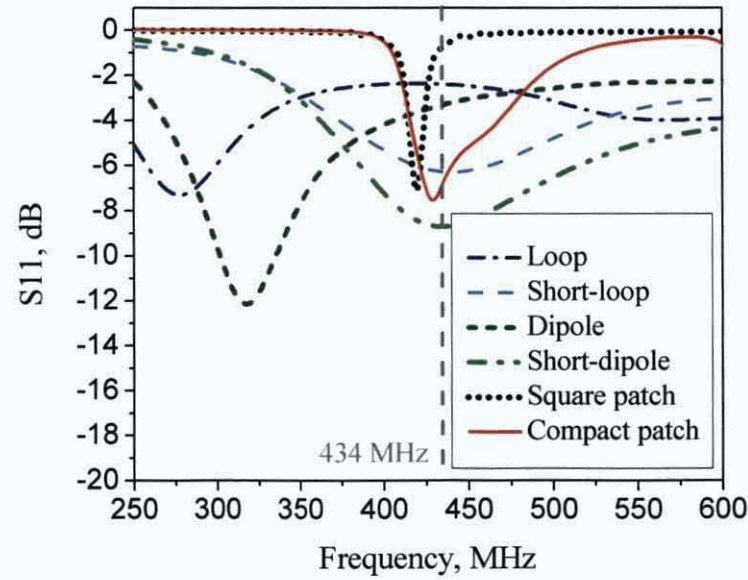
Figure 4.4.: Simulated S11 for 2.7 mm antenna-waterbolus distance.

the loops, the flux lines curve with the circumferences and are tangential to the skin surface. The short-loop has a greater intensity and consequently a greater coupling compared with the detuned full-wavelength loop. Similarly, the dipole field patterns are tangential with the skin but the intensity of aligned fields exceeds that of the loops. The shorter, tuned dipole produces a deeper tissue penetration distributed along the structure. The conventional square patch presents fields normal to the tissue and results in the weakest coupling. The compact patch electric field pattern is a converging distribution of tangential fields focused at the patch center and it achieves the highest coupling penetration into the tissue. In general, inspection of antenna geometries and the electric fields next to the tissue show that a higher coupling corresponds with an increased aperture of tangentially distributed fields.

4.3.3. Specific Absorption Rate Patterns

The plots show the skin surface profile and the cross-section; in Figure 4.6 and 4.7 due to the applicators being 2.7 mm distant and in Figure 4.8 and 4.9 due to compact patch at various distances. The scale is clamped at $1\,\mathrm{W/kg}$ for finer resolution illustration of the lower and medium SAR patterns.

By inspection, Figure 4.6 (a, b) shows that SAR profiles of the loop and short-loop align to the circumference of the wire elements and that the peak values, 0.27 and $0.54\,\mathrm{W/kg}$ respectively, are located near the feed points. Under the loaded conditions, the shorter loop sustains an even distribution of energy with $3.66\,\mathrm{cm^2}$ at the $\mathrm{SAR} > 0.5\,\mathrm{W/kg}$ threshold; while in contrast, the shortened resonant current length on the larger loop produces a very low SAR diagonally opposite the feed. Figure 4.6 (c, d) illustrates that the dipole and short-dipole elements have larger patterns, $6.79\,\mathrm{cm^2}$ and $89.44\,\mathrm{cm^2}$ respectively, at the $\mathrm{SAR} > 0.5\,\mathrm{W/kg}$ threshold. The peak values, 0.52 and $0.95\,\mathrm{W/kg}$ respectively, are centered on the feed points. SAR patterns due to the conventional square patch and the compact patch are illustrated in Figure 4.6 (e, f). In the square patch, the radiating edge adjacent to the feed point domi-
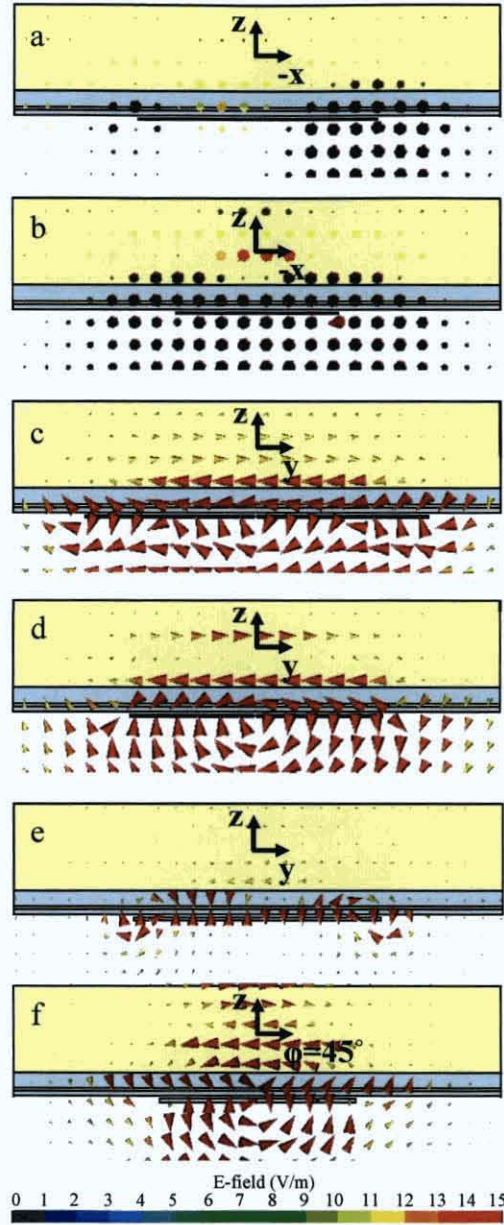
Figure 4.5.: Electric field cross-section for 2.7 mm antenna-waterbolus distance. (a) Loop, (b) short-loop, (c) dipole, (d) short-dipole, (e) conventional square patch and (f) compact patch antenna. Plots (a) – (b) in the plane $y = 0$ mm, plots (c) – (e) in the plane $x = 0$ mm and plot (f) in the plane $\varphi = 45°$.
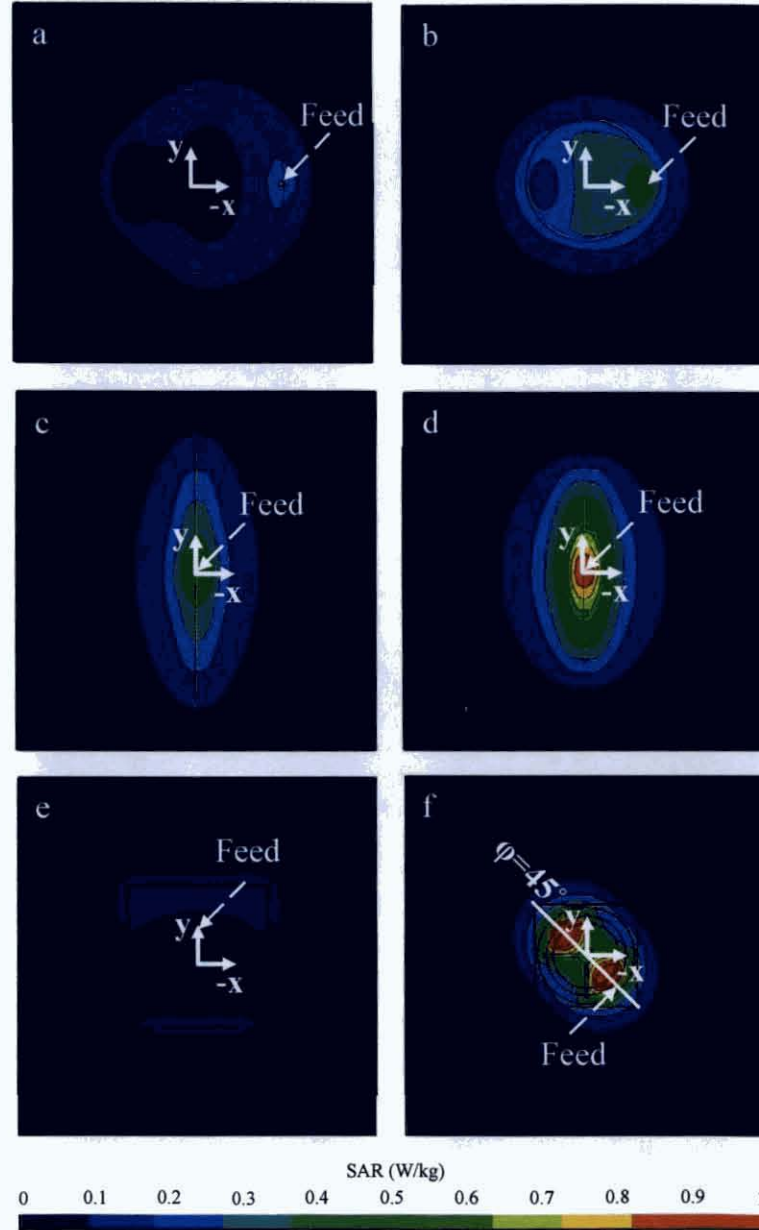
Figure 4.6.: SAR at tissue surface for 2.7 mm antenna-waterbolus distance. (a) Loop, (b) short-loop, (c) dipole, (d) short-dipole, (e) conventional square patch and (f) compact patch antenna.

nates the SAR profile while the pattern due to opposite edge is reduced. Peak values are less than 0.07 W/kg and a large null exists in the patch centre. The SAR > 0.5 W/kg profile of the compact patch is dominant at the two locations where a diagonal line through the origin (φ=45°) intersects with the loop aperture. The area covered is 91.52 cm^2 and the peak value is 1.32 W/kg.

Figure 4.7 illustrates the absorption patterns of the peak SAR body tissue numerical model cross-sections for each of the antennas. Shortening the loaded loop antenna circumference (Figure 4.7 (a, b)) increases both the SAR penetration depth into the muscle layer and the peak value by a factor of three to 0.3 W/kg at the loop centre point. The 0.5 W/kg penetration depth for the short-loop is 0.64 cm. Similarly, the short-dipole SAR cross-section exceeds that for the dipole (Figure 4.7 (c, d)) by a factor of two with a level of 0.4 W/kg. The SAR pattern is concentrated at the feed point but is distributed evenly across the length of the short-dipole. The 0.5 W/kg penetration depths for the dipole and short-dipole are 0.57 cm and 2.89 cm, respectively. The conventional square patch SAR pattern cross-section (Figure 4.7 (e)) shows values of about 0.06 W/kg in the patch centre reaching the muscle layer. The SAR cross-section of the compact patch (Figure 4.7 (f)) is concentrated within the smaller aperture and it exhibits the deepest tissue penetration. The 0.5 W/kg threshold is 5.21 cm below the surface and the $1/e^2$ penetration depth is 63 mm.

Figure 4.8 and 4.9 show the SAR front profile and cross-section patterns for the compact patch as the antenna-waterbolus separation distance reduces. Despite the increased permittivity load on the antenna electric fields, the resonant modes remain matched at the source frequency and the SAR increases due to improved tissue coupling. The similar SAR profiles for the 5.4 mm and 2.7 mm separation distances show that the compact patch is insensitive to changes in high dielectric loading at very close proximities. Table 4.2 compares the dimensions and SAR values for each of the antennas. The resultant SAR levels are primarily a function of the antenna geometry and the compatibility of field coupling with the tissue at a given distance. Reducing the separation distance further increases the SAR, provided the antenna remains frequency

Figure 4.7.: SAR cross-sections for 2.7 mm antenna-waterbolus distance. (a) Loop, (b) short-loop, (c) dipole, (d) short-dipole, (e) conventional square patch and (f) compact patch antenna. Plots (a) – (b) in the plane $y = 0$ mm, plots (c) – (e) in the plane $x = 0$ mm and plot (f) in the plane $\varphi = 45°$.
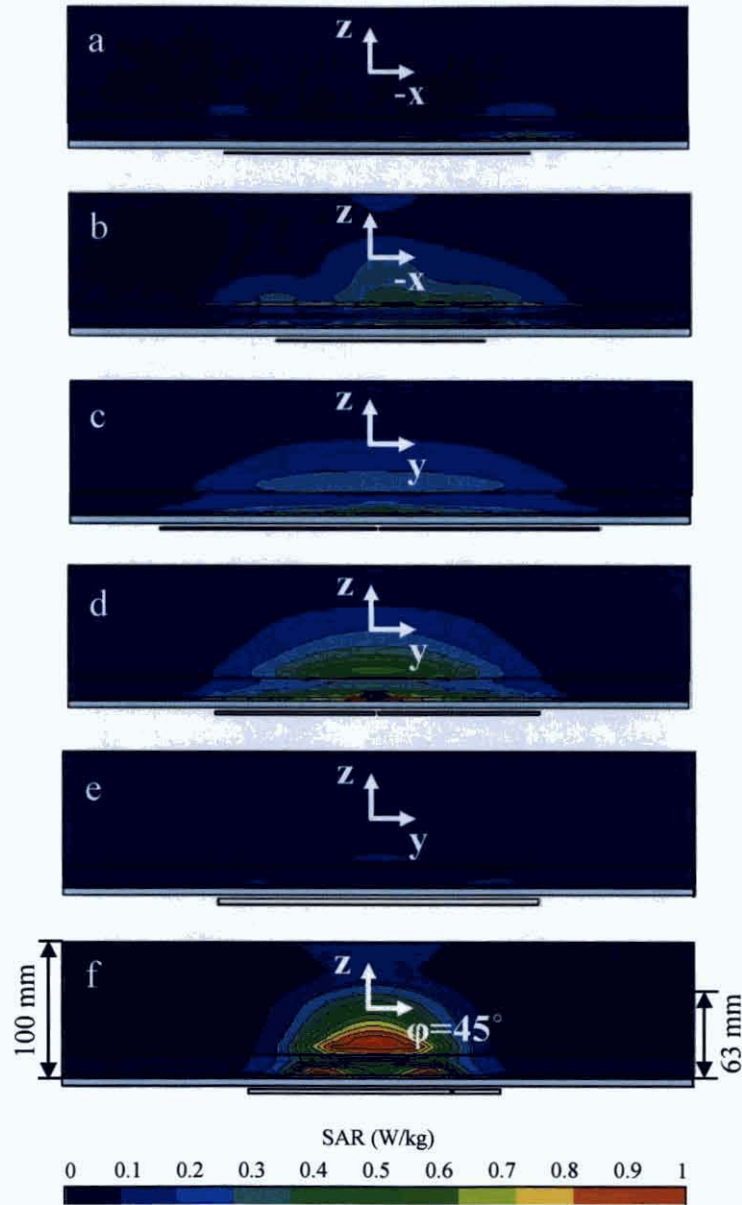
Table 4.2.: Summary of antenna dimensions, peak SAR and SAR pattern parameters for 2.7 mm antenna-waterbolus distance. (Normalized to 1 W antenna input power).

	Largest dimension [cm]	Antenna area [cm^2]	Peak SAR [W/kg]	Body model area with SAR>0.5 W/kg [cm^2]	Body model penetration depth SAR>0.5 W/kg [cm]
Loop	22.6	404.7	0.27	SAR<0.5 W/kg	SAR<0.5 W/kg
Short-loop	15.6	193.5	0.54	3.66	0.64
Dipole	32.4	6.5	0.52	6.79	0.57
Short-dipole	23.9	4.7	0.95	89.44	2.89
Conv. Sq. Patch	33.0	538.2	0.07	SAR<0.5 W/kg	SAR<0.5 W/kg
Compact Patch	18.4	169.0	1.32	91.52	5.21

and impedance matched with the source. Variations in the tissue layer thickness are less influential on the SAR rates. The thicker skin layer produces a reduced SAR penetration and the thickest layer of fat results in greater penetration. The differences in SAR due to the tissue layer thickness changes are summarized in Table 4.3.

4.3.4. Resonant Function of the Compact Patch Antenna

The compact patch area is 31% of the conventional square patch and 40% of the loop, and compared to the dipoles, the smaller dimensions make it an improved ergonomic shape for placing next to the human body.

The compact patch input impedance is characterized by a pair of resonance modes. At very close distances to the waterbolus-tissue load, the paired resonance modes combine to be indistinguishable. As the antenna approaches the waterbolus, the loaded currents on the groundplane constrict to the periphery of the slots. Unlike the wire element antennas, changes in the input impedance of the compact patch are desensitized by the dielectric substrate which shadows/buffers the near-field evanescent modes from direct loading by the tissue. The bandwidth is increased (Figures 4.3 - 4.4) and the input impedance mismatch is reduced.
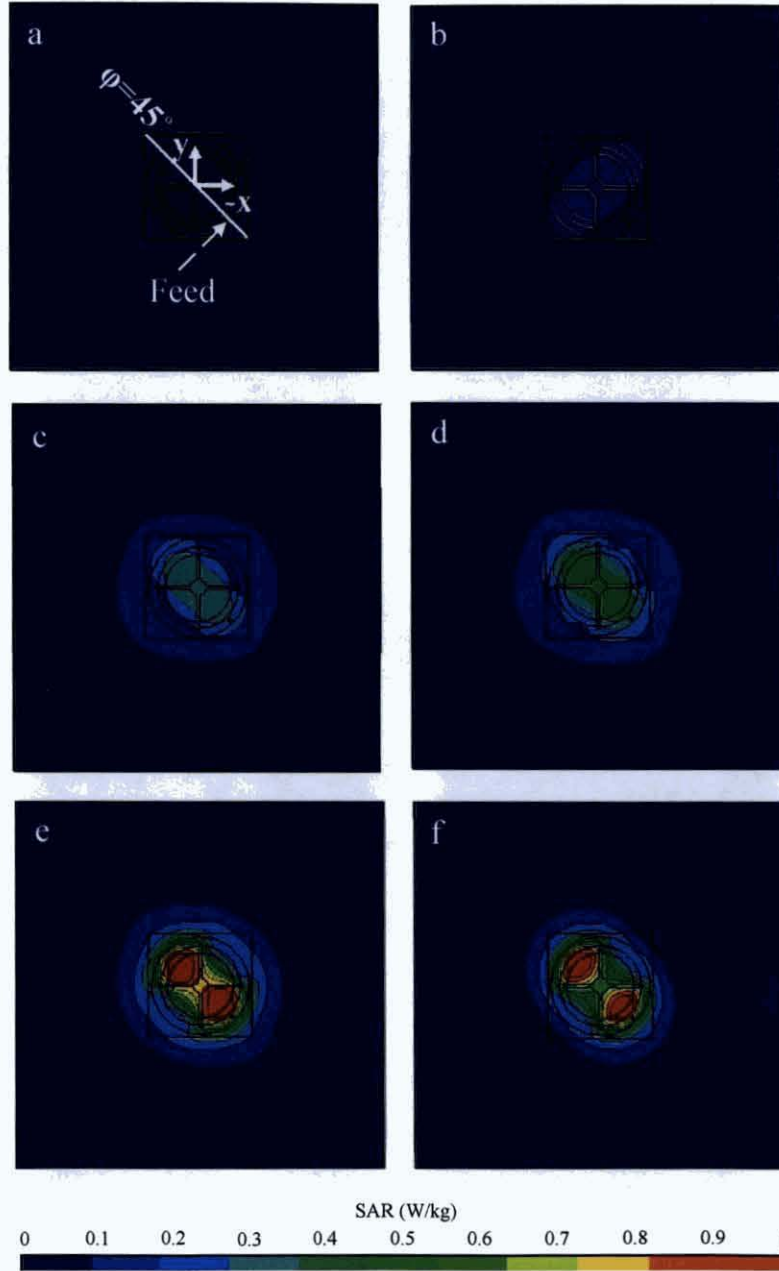
Figure 4.8.: SAR at tissue surface for the compact patch. (a) Antenna geometry and coord. syst. Antenna-waterbolus distance: (b) 43.2 mm, (c) 10.8 mm, (d) 8.1 mm, (e) 5.4 mm and (f) 2.7 mm.
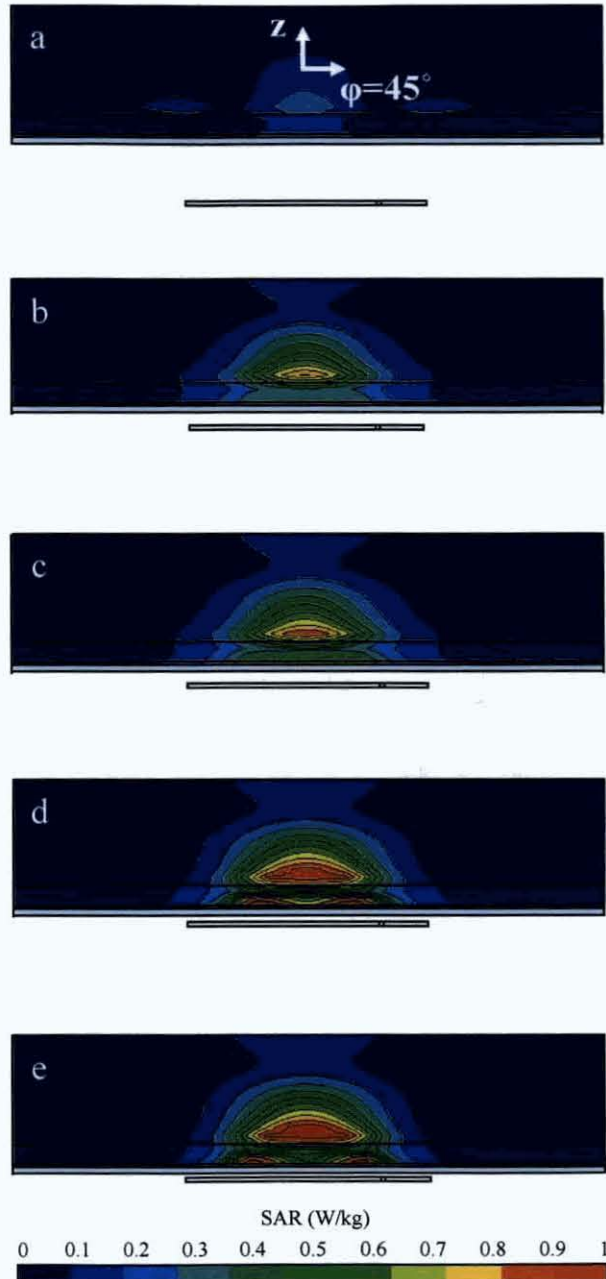
Figure 4.9.: SAR cross-sections for the compact patch (plane $\varphi = 45°$) for antenna-waterbolus distances: (a) 43.2 mm, (b) 10.8 mm, (c) 8.1 mm, (d) 5.4 mm and (e) 2.7 mm.

Table 4.3.: Compact patch SAR penetration for various combinations of skin, fat and muscle layer thicknesses for 2.7 mm antenna-waterbolus distance. (Normalized to 1 W antenna input power).

Tissue Layers			Body model penetration depth
Skin [mm]	Fat [mm]	Muscle [mm]	for SAR>0.5 W/kg [cm]
0.4	0	99.6	4.90
0.4	15	84.6	5.42
0.4	30	69.6	5.78
2.6	0	97.4	4.79
2.6	15	82.4	5.21
2.6	30	67.4	5.31

4.4. Conclusion

The design of the compact patch antenna presented in the previous chapter is contrasted with basic loop, dipole and conventional square patch antennas which have been previously used in clinical settings. It also has low-cost, ease of manufacture and low profile advantages over other waveguide and horn applicators. The slotted features in the antenna geometry afford a 69% area reduction with respect to the conventional square patch design and also prevent load suppression of the resonant modes. The dominant electric field flux lines on the antenna are tangentially aligned to produce a larger coupling aperture with the tissue layers. This results in a $1/e^2$ SAR penetration depth of 63 mm which exceeds the performance of other waveguides, horn and microstrip designs. The next chapter evaluates the suitability of the compact patch antenna for the treatment of tumours located at three different regions of the human body.

5. In-silico Performance of the Compact Patch Antenna at Various Human Anatomical Regions

$\mathbf{S}$IMPLIFIED planar-layered or homogeneous body tissue numerical models do not include the complex internal shapes of heterogeneous biological bodies. Heterogeneous body modelling provides more credible and higher peak SAR values due to the interfaces between wet and dry tissues.

In this chapter the applicator performance is evaluated at three body areas of a heterogeneous full-body model to assess the suitability of the proposed antenna for different patient anatomy. These three anatomical regions present diverse aperture coupling and tissue composition. Different conformal waterbolus and air gap thickness are evaluated. Antenna impedance matching, specific absorption rate and thermal distribution are reported.

5.1. Introduction

Positioning a patient within the radiating near-field of an antenna can enhance mutual interaction between the radiator and the body. Standard electromagnetic body tissue numerical models do not account for the tissue perfusion

variability due to patient individuality and temporal biological responses but the specific absorption rate and estimated temperature maps can assist in clinical dosage planning [104].

An effective, near-field-loaded antenna design should maintain a stable resonant frequency, efficient matched impedance and a tolerance of various dielectric loads due to different patients or anatomy locations. Simulation of the antenna-to-body tissue numerical model interaction is essential for basic understanding and is particularly dependent on the electromagnetic accuracy of the numerical human model.

One-dimensional [105], coarse-resolution homogeneous [27] and planar layered [103] body tissue numerical models can reveal a basic coupled energy distribution. However, such models can underestimate the actual peak SAR and patterns, which could have implications for patient comfort and application strategies during clinical treatment.

The commercial heterogeneous body tissue numerical model used here has 5 mm resolution voxels that were segmented from 1 mm stepped CT and MRI cross-sections through an adult male [106]. While the resolution limited the tissue and organ detail to outline shapes, the inter-tissue boundaries introduce reflection, transmission and dispersion effects that occur in the body. Modelling inaccuracies occur where the electric field or surface current orientations align with under-resolved features in the model geometry. A steady state thermal response to the electromagnetic coupling is produced by post processing with the Pennes equation. However, the calculation does not factor dynamic physiological responses in the temperature rise predictions and can underestimate the natural cooling processes.

While the effects of waterbolus thickness have been investigated with simplified body models [107, 108], this work explores the antenna-to-waterbolus air gap and conformal-shaped waterbolus thickness effects for the compact patch antenna, which geometry was detailed in the previous chapters, at three locations on the human body. The antenna was positioned in the coronal plane in front of the stomach, at the rear of the head and between the shoulder blades

(a)   (b)
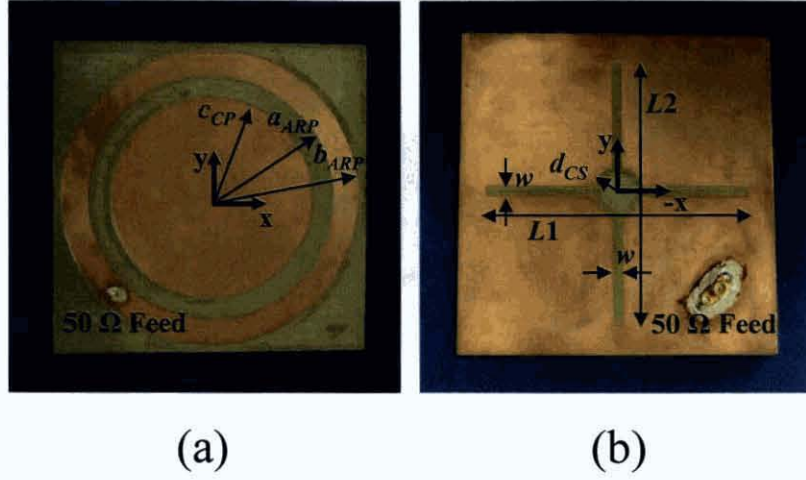
Figure 5.1.: Fabricated antenna and dimensions viewed from (a) front side, towards the tissue and (b) rear side, away from the tissue.

areas to study differing coupling mechanisms of the antenna. Those three locations are respectively named epigastric, inter-scapular and head region through this work.

5.2. Methodology

5.2.1. Compact Patch Antenna

Figure 5.1 shows a photograph of the compact patch antenna [109] which is discussed in Chapter 3. Chapter 4 compares the basic functionality of the design with other published approaches and clinically used antennas.

5.2.2. Human Body Tissue Numerical Model

The human body tissue numerical model used in this work was developed by Remcom with data from the Visible Human Project [106] for compatibility with the XFDTD electromagnetic solver [58]. The body model is 1.80 m long, has a mass of 103 kg and comprises twenty-three tissue types with thermal

Table 5.1.: Dielectric properties of the tissues at 434 MHz [49] for the simulated body areas.

	Permittivity $[\varepsilon_r]$	Conductivity $[\sigma,\ S/m]$	Density $[\rho,\ kg/m^3]$	σ/ρ ratio $\times 10^{-4}$
Blood	63.826	1.361	1058	12.9
Cancellous bone	22.257	0.241	1920	1.26
Cartilage	45.140	0.598	1097	5.45
Cortical bone	13.071	0.094	1990	0.47
CSF - Cerebrospinal Fluid	70.630	2.260	1007	22.4
Fat, yellow marrow ·	5.566	0.041	916	0.45
Gray matter, cerebellum	56.814	0.751	1038	7.24
Lung	23.579	0.380	260	14.6
Muscle, heart, spleen, colon, tongue	56.866	0.805	1041	7.69
Nerve	35.038	0.455	1038	4.39
Pancreas, tendon, aorta, liver, other	47.120	0.568	1220	4.66
Skin	46.059	0.702	1100	6.24
Small intestine	65.266	1.922	1042	18.4
Stomach, esophagus	67.186	1.013	1050	9.65
White matter	41.659	0.451	1038	4.35

and frequency-dependent dielectric properties. Table 5.1 lists the conductivity, density and relative permittivity values of the tissues at 434 MHz for the simulated body areas [49].

An adaptive mesh, with 1 mm cell resolution, was set for the antenna structure and the analysed body locations. This improves simulation accuracy and complements the FDTD constraint of having 10 cells per wavelength [110]. For cerebrospinal fluid (ε_r=70.63), the highest permittivity in the treatment area, a 1 mm cell is 1.21% of guided wavelength (82.2 mm). More than 20 million cells were generated and required 1.03 Gbytes of memory. A Gaussian monocycle was used to calculate the broadband impedance performance and a sinusoidal source centred at 434 MHz is required for steady state analysis.

The simulation time was typically 10 hours on a 3.4 GHz PC with 4 Gbytes of RAM.

Comparisons of cubic cell sizes in numerical human body models, between 5 mm and 3 mm meshes [98] and between 6 mm and 2 mm meshes [111], indicate that a finer resolution is only necessary for SAR accuracy in tiny organs (e.g. eye lens). Increased body model accuracy here reveals the complexity of the coupling to multiple tissues.

When magnetic resonance images (MRI) are used in custom-made hyperthermia treatment planning, this numerical body model can provide interinstitutional reference for hyperthermia applicator comparison. Limitations of this model are related to limited resolution and constant perfusion rates. Future temperature analysis tools should account for spatial and time dependent perfusion rates.

5.2.3. SAR and Temperature Analysis

The E-field distribution in the exposed body tissue is calculated and then the specific absorption rate (SAR) is computed as seen in equation 2.7. The conductivity-to-density ratio is a measure of absorbed energy into a tissue, and the value at 434 MHz for the tissues at the simulated body areas is listed in Table 5.1.

SAR patterns were normalized to 1 W of antenna input power and evaluated for 1 g averaged spatial peak SAR to mitigate against FDTD approximated hotspots [112, 113]. The 50% iso-SAR and the $1/e^2$ penetration are reported as ESHO quality guidelines for homogeneous or layered body models. The 25% iso-SAR was found to be a better analytical factor for hyperthermia treatment planning in a study of 196 patients [114, 115]. In this work, the 50%, 25% and $1/e^2$ iso-SAR contours are reported.

The temperature increase due to the SAR in each of the simulated body areas is calculated with the Pennes bio-heat equation [54] and computed as seen in Section 2.6. Table 5.2 lists the specific heat capacity, thermal conductivity,

Table 5.2.: Thermal properties [58] of the tissues for the simulated body areas.

	Heat capacity C [J/kg/°C]	Thermal conductivity K [W/m/°C]	Perfusion ω [ml/100 g/ min]	Metabolic heat Q_m [W/m³]
Blood	3600	0.51	1000	0
Cancellous bone	2238	0.36	3	0
Cartilage	3400	0.45	14.3	1000
Cortical bone	1300	0.36	1.4	0
CSF - Cerebrospinal Fluid	4200	0.60	0	0
Fat, yellow marrow	2300	0.23	2.8	293.1
Gray matter, cerebellum	3680	0.56	67.1	5370
Lung	2354	0.45	40	0
Muscle, heart, spleen, colon, tongue	3500	0.49	5	758
Nerve	3640	0.53	56	332.1
Pancreas, tendon, aorta, liver, other	3600	0.51	100	390.4
Skin	3150	0.34	12	1125
Small intestine	3600	0.55	100	333.6
Stomach, esophagus	3500	0.52	40	703.5
White matter	3600	0.50	23.7	5370

perfusion by blood and heat generated by metabolism values of the tissues for the simulated body areas [58].

While temperature increase in the range of 43 to 45 °C was the objective of past hyperthermia treatments, contemporary research is placing greater interest in target the temperature range of 40 to 43 °C, also called mild temperatures [104]. The aim is to improve radiotherapy killing of cancerous cells by overcoming hypoxic protection [116]. The power required to achieve a maximum temperature of 43 °C at the simulated body areas is reported in this work.

5.3. Antenna-Body Locations

When evaluating the suitability of an antenna for different types of cancer, while conductivity-to-density ratios indicate absorption rates across the body, other features needs to be considered. Factors such as aperture loading of tissue volumes, organ shapes, contoured tissue layers and proximity distances have to be investigated for each anatomical body regions

5.3.1. Relevance to Types of Cancer Treatments

The antenna is evaluated at three typical locations during cancer treatment, as shown in Figure 5.2. The antenna is centered and parallel to the sagittal and coronal plane, respectively. At the epigastric location, the antenna is located 600 mm from the top of the scalp, which can be applied for the treatment of superficial adenocarcinoma. The antenna placed at the head location, which is 100 mm from the top of the scalp, can be commonly applied for the treatment of different kind of brain or meninges cancers. At the inter-scapular location, the antenna is located 350 mm from the top of the scalp and can be used to treat melanoma, vertebral or sarcoma cancer.

5.3.2. Variations of Tissue Types and how These are Indicative of Variations Across the Body

The body tissue composition at the three locations is significantly different as outlined in Figure 5.3. The epigastric area is modelled with a layer of skin followed for a very thick layer of fat (around 100 mm) which contains parts of muscle, small intestine, pancreas, and the stomach. The head area is modelled as an abrupt layer of skin next to a layer of yellow marrow and muscle, followed by cortical and cancellous bone structures with cerebrospinal fluid (CSF) involving grey and white matter. The inter-scapular area of the body is modelled with a 10 mm thick layer of skin next to a variable layer of
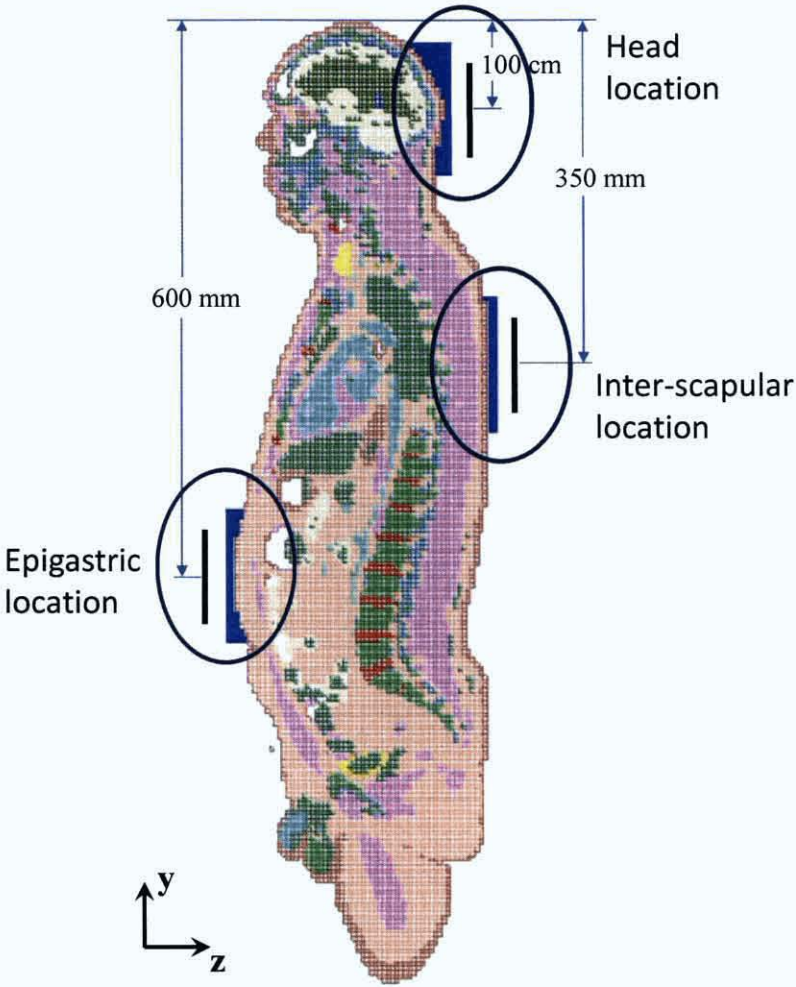
Figure 5.2.: Human body model and antenna locations.

fat tissue and muscle. The cortical bone and white matter precedes the spine, mainly modelled with cancellous bone; cartilage and nerves.

5.3.3. Waterbolus and Aperture Loading

A bolus interfacing the skin of the exposed body region is used to cool the body surface and for improved antenna coupling [107]. In clinical trials the water circulates in a temperature controlled system and in this work values are reported for a water temperature of 27 °C. Different water temperature analysis are not the aims of this work.

The radiating aperture suffers various tissue-loading, depending on its location with respect to the different body shapes. Around 41.4%, 22.4%, and 100% of the radiating aperture area is loaded when the antenna is placed at the epigastric, head, and inter-scapular region, respectively. Different curvature loading at the different antenna-body locations produces different waterbolus thicknesses.

Volume and surface wave oscillations are generated inside the waterbolus if the thickness of the waterbolus exceeds a frequency dependent value. Equations for maximum waterbolus thickness were derived [107, 108] and thinner waterbolus are required as the frequency of the applicator is increased. The maximum waterbolus thickness at the frequency of 434 MHz is found to be 19 mm. In [107, 108] the waterbolus and body model were considered rectangular, but here a more realistic conformal waterbolus and body model are analyzed.

5.4. Results

5.4.1. Antenna Performance with Waterbolus

The effect of different waterbolus thickness and air gap values are analyzed for each body region and the optimum combination in terms of S11 and peak SAR
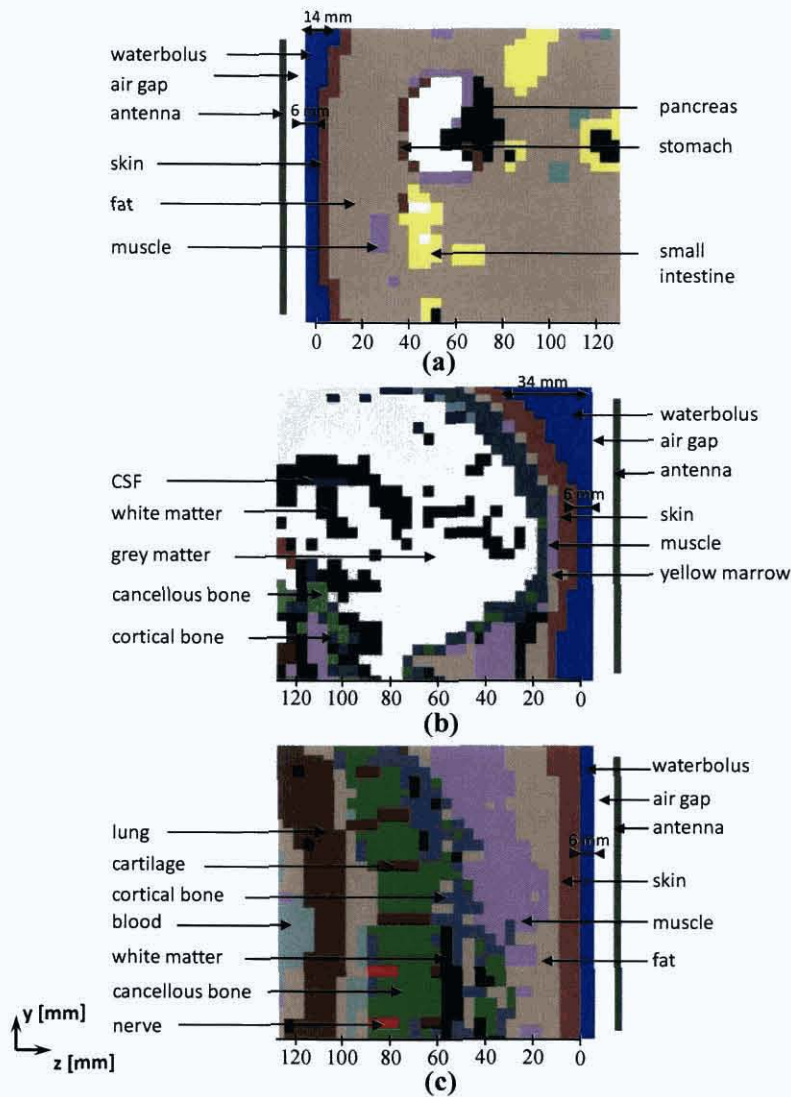
Figure 5.3.: Tissue composition for (a) epigastric, (b) head and (c) inter-scapular location.

is determined. Waterbolus of 6, 8 and 10 mm minimum thickness (i.e, at the antenna centre, because due to the conformability of the bolus around the body the waterbolus thickness is larger on the antenna sides than on the antenna centre for the epigastric and head location) and air gaps from 2 to 16 mm with 2 mm interval were considered. Thinner waterbolus values were not considered because the cooling effects are reduced, and 5 to 10 mm thick waterboluses were found to be optimum for even SAR distribution [107, 108]. The antenna in contact with the waterbolus was not analyzed in this work because of detuning and the antenna performance was compromised. Figure 5.4 summarizes the antenna S11 with constant 10 mm air gaps and variable waterbolus thickness values, and for constant waterbolus thickness of 6 mm with variable air gaps for the epigastric (Figure 5.4 (a) and Figure 5.4 (b)), head (Figure 5.4 (c) and Figure 5.4 (d)) and inter-scapular location (Figure 5.4 (e) and Figure 5.4 (f)).

Increasing the minimum thickness of the waterbolus from 6 to 10 mm produces a drop in resonant frequency of 0.5 MHz for the epigastric, 1 MHz for the head and 3 MHz for the inter-scapular location with a simultaneous degradation in S11 by 3.3 dB, 0.94 dB and 2.12 dB for the three regions respectively. On average for the three antenna-body locations, increasing the waterbolus thickness from 6 to 10 mm, reduces the resonant frequency by 1.5 MHz and degrades the S11 by 2.1 dB.

Increasing the air gap from 2 to 16 mm increases the resonant frequency by 40 MHz for the epigastric, 44 MHz for the head and 29 MHz for the inter-scapular location. The increase in air gap improves the S11 by 10.8 dB for the epigastric, 15.1 dB for the head and 20.24 dB for the inter-scapular location. On average for the three antenna-body locations, increasing the air gap from 2 to 16 mm, increases the resonant frequency by 37.6 MHz and improves S11 by 15.3 dB.

Figure 5.5 shows a summary of the combination of S11 at 434 MHz and peak SAR for the different combinations of waterbolus and air gaps investigated. Increasing the thickness of the waterbolus with a constant air gap 10 mm thick (Figure 5.5 (a)) produces a degradation of the S11 at 434 MHz and small
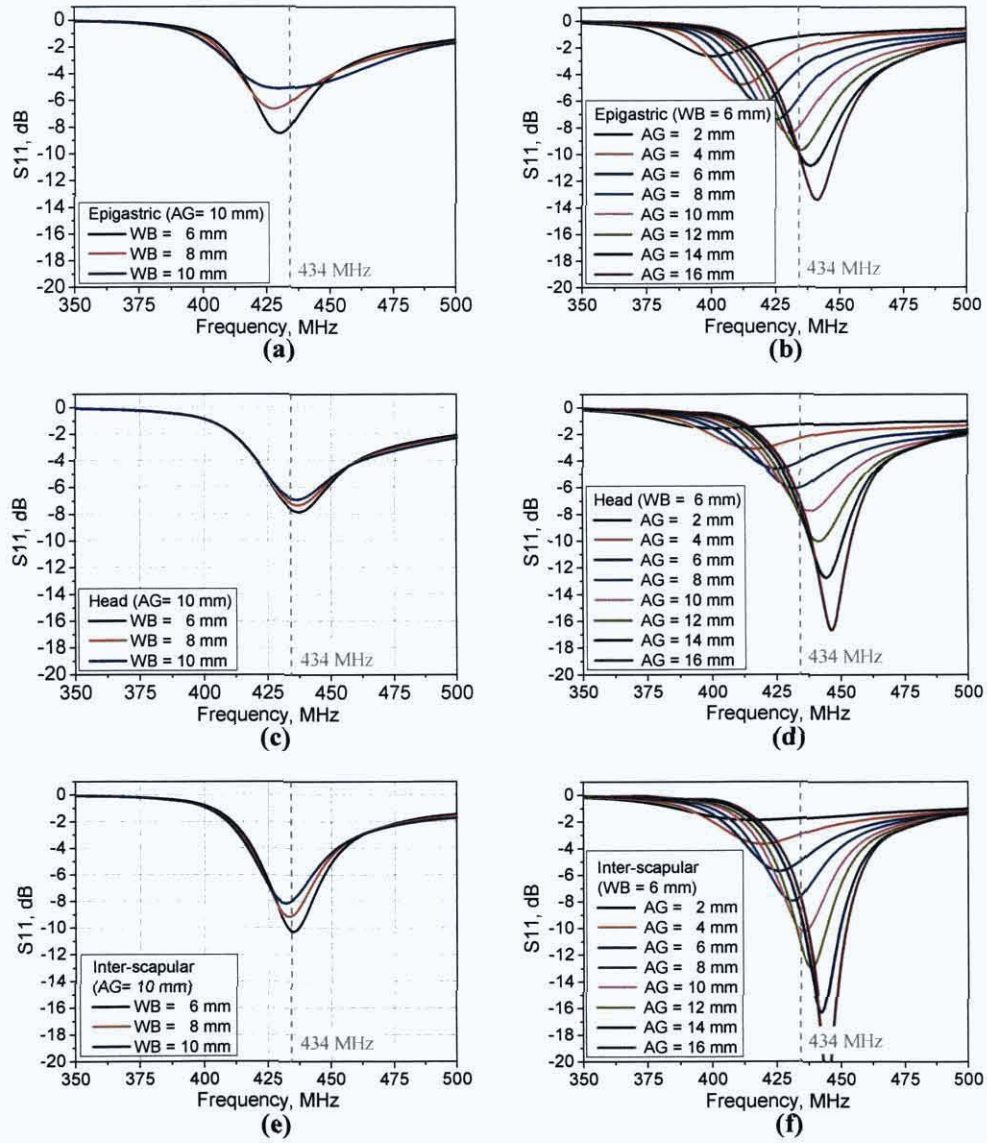
Figure 5.4.: Simulated S11 for different values of waterbolus (WB) and air gaps (AG) thickness for epigastric, head and inter-scapular location.
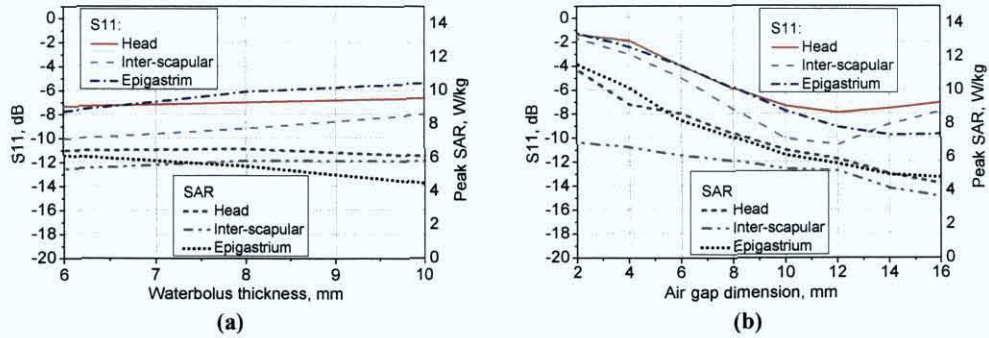
Figure 5.5.: Simulated S11 and SAR for different combinations of (a) waterbolus and (b) air gaps.

variances in peak SAR (around 0.8 W/kg). Increasing the thickness of the air gap with a constant waterbolus 6 mm thick (Figure 5.5 (b)) produces a deeper S11 value at 434 MHz from 2 to 12 mm, and for larger air gaps produces a poorer S11. The peak SAR reduces as the air gap increases.

A waterbolus 6 mm thick and an air gap of 10 mm are found to be the optimum values in order to have an S11 of at least -8 dB and highest peak SAR at 434 MHz.

5.4.2. In-silico Specific Absorption Rate

The SAR cross-section at the medium sagittal plane for the epigastric, head and inter-scapular locations is shown in Figure 5.6. The scale for the SAR is clamped at 4 W/kg for finer resolution illustration of the lower and medium SAR patterns. The different tissues at those locations were specified in Section 5.3. The peak SAR for the three antenna locations was found at 6 ± 1 mm from the surface and aligned with the antenna centre. For the three antenna locations, the SAR is characterized for the 50% iso-SAR being restricted to the skin-fat interface, followed by a cold-spot that coincides with fat tissue for epigastric and inter-scapular location and yellow marrow for the head location. Behind the fat or yellow marrow location, a secondary SAR hotspot

Table 5.3.: Peak SAR and iso-SAR penetrations for the heterogeneous body tissue numerical model.

	Peak SAR [W/kg]	50% SAR penet. [mm]	25% SAR penet. [mm]	Sec. 25% SAR penet. [mm]	$1/e^2$ SAR penet. [mm]
Epigast.	6.14	7	9	51	55
Head	6.41	10	15	28	44
Inter-scap.	5.28	10	17	52	60

aligned with the antenna centre follows the contours of the tissues with greater conductivity-to-density ratio, in particular the small intestine for epigastric, gray matter for head and muscle tissue for inter-scapular location.

The epigastric location presents a peak SAR of 6.14 W/kg. The 50% iso-SAR area has a length of 82 mm and a penetration of 7 mm. The 25% iso-SAR area has a length of 95 mm and a penetration of 9 mm. The 25% SAR secondary penetration is 51 mm and the $1/e^2$ SAR penetration is 55 mm.

The head location presents a peak SAR of 6.41 W/kg. The 50% iso-SAR area has a length of 57 mm and a penetration of 10 mm. The 25% iso-SAR area has a length of 77 mm and a penetration of 15 mm. The 25% SAR secondary penetration is 28 mm and the $1/e^2$ SAR penetration is 44 mm.

The inter-scapular location presents a peak SAR of 5.28 W/kg. The 50% iso-SAR area has a length of 78 mm and a penetration of 10 mm. The 25% iso-SAR area has a length of 106 mm and a penetration of 17 mm. The 25% SAR secondary penetration is 52 mm and the $1/e^2$ SAR penetration is 60 mm.

Peak SAR differences and iso-SAR penetration for the three locations of the heterogeneous body model are summarized in Table 5.3.

5.4.3. In-silico Temperature

The temperature increase cross-sections at the medium sagittal plane for the epigastric, head and inter-scapular locations is shown in Figure 5.7. A maximum final temperature of 43 °C is considered. The waterbolus prevents the

Figure 5.6.: SAR distribution at the sagittal plane for (a) epigastric, (b) head
and (c) inter-scapular location.
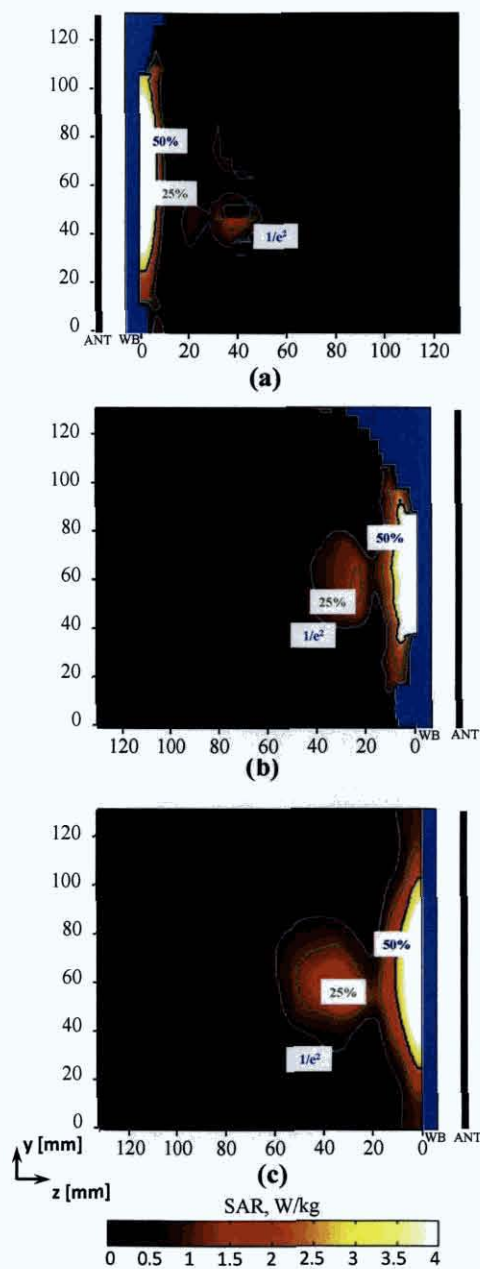
temperature increase from the surface up to 2 to 5 mm depth, reaching the maximum increase at around 6 mm depth. In order to get the 43 °C temperature threshold, the required power source is 78 W for the epigastric, 75 W for the head, and 92 W for the antenna placed at the inter-scapular location. Although the maximum temperature increase is dominated by SAR hotspots located near the surface, the heterogeneity of thermal tissue properties dictates that temperature increase diverges from SAR distribution at deep distances. At the epigastric location, the internal hotspot coincides with the small intestine and stomach, and it can be seen how the temperature increases in the air filled cavities of those organs. At the head location it can be seen that the cooling properties of the tissues at the medium sagittal plane result that the maximum temperature in this plane does not reach the 43 °C. At the inter-scapular location, the length of the temperature increase hotspot is reduced compared with the SAR hotspot. The secondary temperature increase hotspot follows the $1/e^2$ iso-SAR.

Correlation between simulation and measured data was improved when perfusion values were double that of the initial value [104]. In our study, when doubling the value of the initial perfusion values, to reach the 43 °C threshold, the required power source has to increase by 3 W for the epigastric, 4 W for the head and 7 W for the inter-scapular location, with respect to the initial power values.

5.4.4. Layered Planar and Homogeneous Muscle Body Model

In order to improve the understanding of how the power deposition mechanism in body anatomies are related to different antenna apertures or different tissue loading, the SAR performance was analyzed for a layered planar model and the body model with homogeneous muscle tissue.

The layered planar model has been modelled with three layers of skin, fat and muscle of 5 mm, 20 mm and 75 mm respectively. These are the tissues
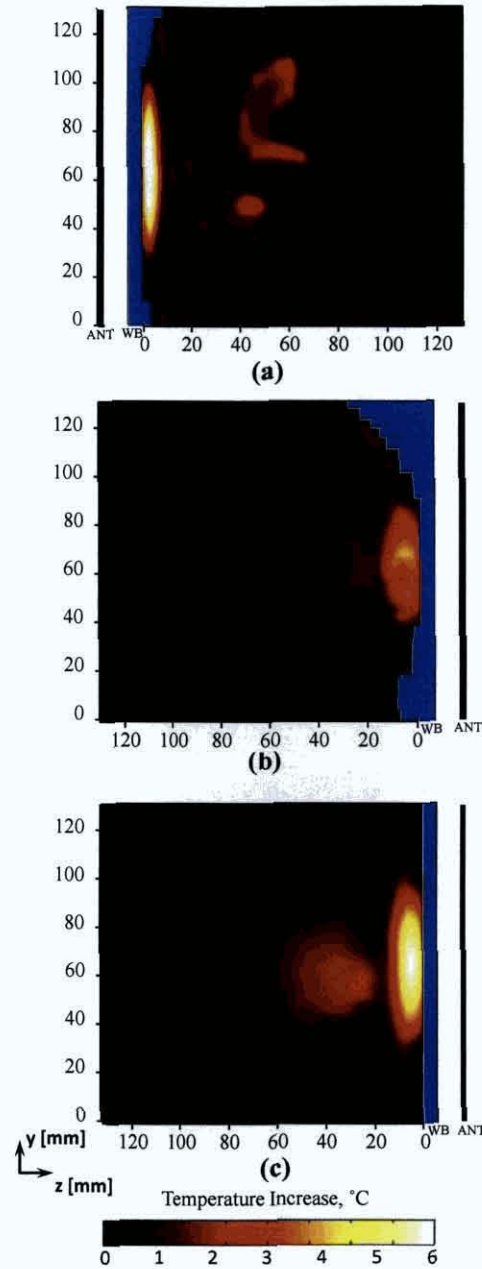
Figure 5.7.: Temperature distribution at the sagittal plane for (a) epigastric,
(b) head and (c) inter-scapular location.
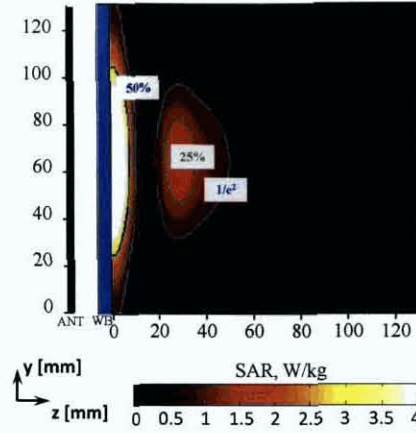
Figure 5.8.: SAR distribution through the antenna centre for layered planar model.

and thicknesses found at the epigastric location through the antenna centre. Figure 5.8 shows the SAR profile through the antenna centre for this layered model. The peak SAR is 5.54 W/kg. The 50% iso-SAR area has a length of 78 mm and a penetration of 7 mm. The 25% iso-SAR area has a length of 106 mm and a penetration of 9 mm. The 25% SAR secondary penetration is 38 mm and the $1/e^2$ SAR penetration is 51 mm.

Figure 5.9 shows the SAR profile through the sagittal plane for the epigastric, head and inter-scapular locations when the antenna is loaded with the homogeneous muscle body model. The maximum SAR is aligned with the antenna centre and presents a smooth distribution only distorted at the epigastric location, when the energy reaches air filled cavities at the stomach and small intestine. With the homogeneous muscle body model, the epigastric location presents a peak SAR of 3.95 W/kg. The 50% iso-SAR area has a length of 82 mm and a penetration of 25 mm. The 25% iso-SAR area has a length of 105 mm and a penetration of 47 mm. The $1/e^2$ SAR penetration is 56 mm. The head location presents a peak SAR of 4.20 W/kg. The 50% iso-SAR area has a length of 57 mm and a penetration of 22 mm. The 25% iso-SAR area has

Table 5.4.: Peak SAR and iso-SAR penetrations for the homogeneous muscle
body tissue model.

	Peak SAR [W/kg]	50% SAR penet. [mm]	25% SAR penet. [mm]	$1/e^2$ SAR penet. [mm]
Epigast.	3.95	25	47	56
Head	4.20	22	37	53
Inter-scap.	3.75	32	49	60

a length of 60 mm and a penetration of 37 mm. The $1/e^2$ SAR penetration is 53 mm. The inter-scapular location presents a peak SAR of 3.75 W/kg. The 50% iso-SAR area has a length of 78 mm and a penetration of 32 mm. The 25% iso-SAR area has a length of 130 mm and a penetration of 49 mm. The $1/e^2$ SAR penetration is 60 mm. Peak SAR differences and iso-SAR penetration for different anatomical regions of the muscle tissue model are summarizes in Table 5.4.

5.5. Discussion

Rectangular waterbolus interfacing a homogeneous muscle tissue models [107] and fat-muscle layered models [108] showed that waterbolus thickness is a critical parameter for clinical hyperthermia applications. The optimum waterbolus in terms of best S11 and higher peak SAR for the three antenna locations has been found to be 6 mm thick at the antenna centre, but the different body shapes produces different waterbolus thickness at the antenna sides for each location.

The experiment with waterbolus of different thicknesses (Figure 5.4) showed that thicker waterbolus produces poorer S11 values for the antenna-body areas investigated. Figure 5.10 shows the S11 for the antenna at the three body areas with the optimum waterbolus and air gap combination. The smaller antenna loading aperture for the head location with a 22 to 34 mm thick waterbolus in the antenna edges (in [107, 108] the maximum waterbolus thickness at 434 MHz
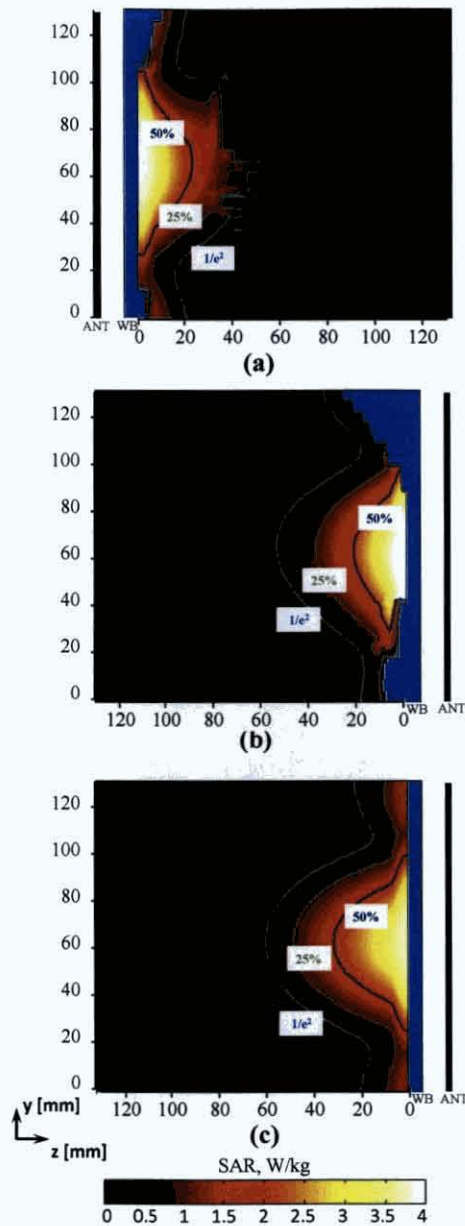
Figure 5.9.: SAR distribution at the sagittal plane for homogeneous muscle
body model for (a) epigastric, (b) head and (c) inter-scapular
location.
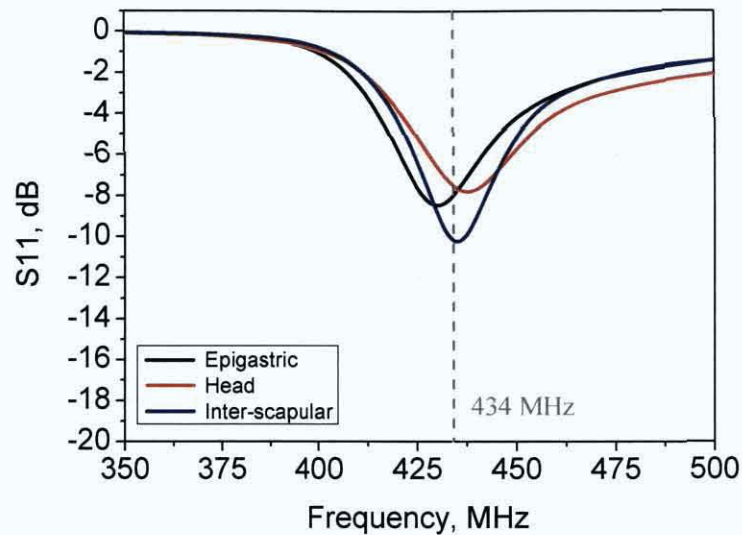
Figure 5.10.: Simulated S11 for the optimum waterbolus and air gap combination.

is 19 mm) produces that both volume and surface wave oscillations can be generated inside the waterbolus [107]. This generates a poorer S11 for the antenna at this location compared with the antenna at the epigastric and inter-scapular location.

The highest peak SAR was found at the head location, which presents the smaller antenna aperture loading. The smaller antenna aperture produces that the tangentially aligned E-field [109] perpendicularly intercepts the skin with the consequential greater peak SAR.

In terms of SAR penetration, at the epigastric location, the tissue which produces the deeper penetration is the small intestine, which is the tissue with the second highest conductivity-to-density ratio. The deepest penetration at the head and inter-scapular locations are found at the grey matter and muscle, respectively. These two tissues present similar conductivity-to-density ratios.

Small differences were found for the current density distributions at the antenna patch surface for the three antenna-body locations as shown in Fig-

ure 5.11 as an indication of antenna stability for different loading conditions. Currents remain stronger at the annular ring and weaker at the circular patch for the antenna at the head location compared with epigastric and the inter-scapular location. The presence of the thick waterbolus at the annular ring (which can generate volume and surface wave oscillations), prevents the activation of the parasitic circular patch.

The temperature prediction analysis has to be improved due to the lack of understanding of tissue perfusion variances at different temperatures, perspiration variances and other factors. However, to have an initial approximation, the temperature distribution was analysed following the criteria mentioned in Section 5.2 at the three antenna-body areas, and the required power source in order to get the 43 °C threshold was determined. The required power source is inversely proportional to the peak SAR obtained for the different locations and there is a linear relation between peak SAR and required power for the epigastric (peak SAR = 6.14 W/kg, required power = 78 W), head (peak SAR = 6.41 W/kg, required power = 75 W) and inter-scapular location (peak SAR = 5.28 W/kg, required power = 92 W. The small differences are due to the different thermal properties of the tissues at the different locations. The thicker skin and muscle tissue (which presents 76% and 44% higher perfusion than fat tissue) for the inter-scapular location demands a greater increase in required power source when doubling the tissue perfusion, in order to get the 43 °C threshold.

To improve the understanding of the different loading effects on the antenna performance, the SAR distribution has been analysed for a layered planar model and the homogeneous muscle body model. The simplified layered body model of similar tissue thickness to those found at the epigastric area and aligned with the antenna centre underestimates peak SAR by 9.77% and presents lower penetration compared with the heterogeneous body model.

It was found that peak SAR is related to the permittivity gradient between interfacing tissues [117]. The peak SAR in the body tissue models reduces similarly from the heterogeneous to the homogeneous muscle models with values
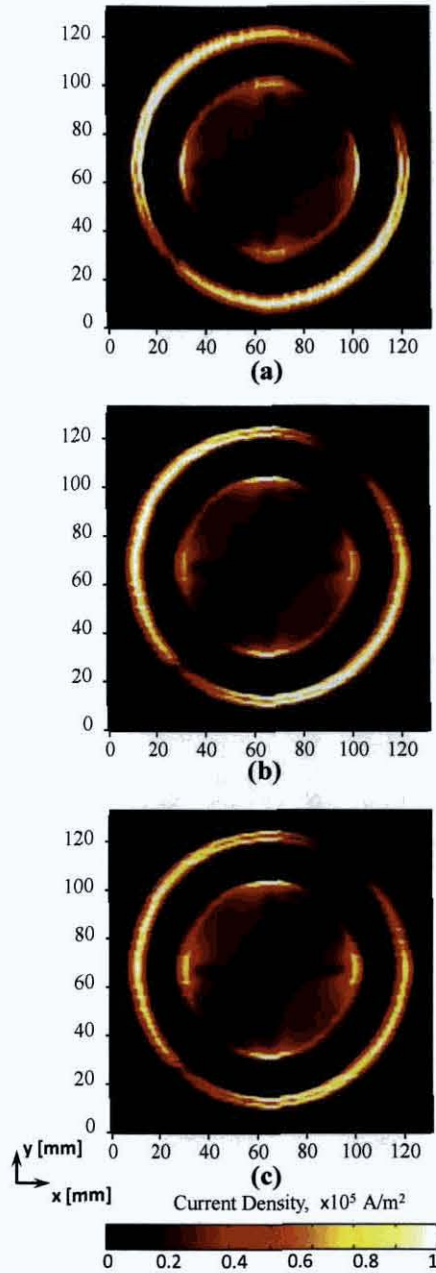
Figure 5.11.: Current density distribution at the antenna patch surface for (a) epigastric, (b) head and (c) inter-scapular location.

of 35.6%, 34.4% and 28.9% for the epigastric, head and inter-scapular regions, which is an average reduction of 32.9%. SAR penetration for the body models increases for the homogeneous muscle model compared with the heterogeneous model for the three locations investigated, but the lower penetration was found for the head location, in which the power absorption in the superficial tissues prevent the energy reaching deep tissues.

The head region presents the highest values of peak SAR for both body heterogeneous and homogeneous muscle models. For the heterogeneous body model, peak SAR reduces by 4.21% between the head and epigastric region and by 17.6% between the head and inter-scapular region. For the homogeneous muscle body model, peak SAR reduces by 5.95% between the head and epigastric region and by 10.7% between head and inter-scapular region.

5.6. Conclusions

The performance of a compact patch hyperthermia applicator has been described for potential use in the treatment of cancers located at the epigastric, head or inter-scapular body regions. These three locations present different aperture loading and have different tissue composition. Optimum waterbolus thickness and air gap values have been determined in terms of best S11 and highest peak SAR following the evolution of previous analysis with rectangular layered models. The tangentially aligned electric field generates the highest SAR at the head location, which presents the smaller antenna aperture loading. The required power for a maximum temperature threshold of 43 °C is inversely proportional to peak SAR. The power source has to increase from 78 to 81 W for the epigastric, from 75 to 79 W for the head and from 92 to 99 W for the inter-scapular location in order to get the same temperature threshold of 43 °C when doubling the perfusion value of each tissue. Future applications should consider perfusion rates with spatial, temporal and temperature dependence to have more accurate models. In the next chapter, modeling validation and measurements for the compact patch antenna are presented.

6. Model Validation and Measurement Setup

THE human body comprises a complex anatomy with organs and tissues of arbitrary shape and frequency-dependent dielectric properties. Electromagnetic models have been implemented to simulate the interaction between antennas and human bodies. Liquids have been developed with dielectric properties representative of homogeneous human bodies. A radiating antenna can be located in close proximity to a phantom containing the liquid and the resultant field distribution inside the liquid can be evaluated with an electromagnetic E- and H-field probes.

In order to validate the models used in this work, measurements are performed in a phantom containing liquid which simulates homogeneous human tissue. In this chapter, the recipe of the liquid, the preparation, and the dielectric property measurement processes are highlighted. The dosimetric assessment system (DASY) is used to evaluate the specific absorption rate (SAR) generated for the compact patch antenna which is detailed in the previous chapters. The measurement setup with antenna, phantom and liquid is simulated in the XFDTD electromagnetic solver. Simulated and measured results in term of SAR and S11 are evaluated.

6.1. Liquid Preparation

Different representations of human tissue have been proposed in the literature [118, 119] and liquid simulating homogeneous human tissue are some of the most used [112, 120].

The liquids are usually sugar-water or glycol based. In this work, a sugar-water based solution was used. The ingredients of the liquid were water, salt, sugar, cellulose and preventol D7. Water is the basis for the liquid and it increases the liquid relative *permittivity* and decreases the conductivity. Salt increases the conductivity and decreases the relative permittivity. Sugar decreases the relative permittivity. The cellulose increases the liquid viscosity and keeps the sugar in solution. The preventol D7 is a preservative which prevents the spread of bacteria and moulds [112, 121].

Permittivity values with an error of 5% and conductivity values with an error of 10% are given for the frequencies of 450 MHz and 835 MHz [121]. Interpolating those values at the frequency of 434 MHz gives values that are in the range of error of the recipe at 450 MHz. Consequently the recipe at 450 MHz ($\varepsilon_r = 44.5$, $\sigma = 0.86\,\mathrm{S/m}$) was used. The recipe was: 513.24 g of water, 50.0 g of salt, 750.9 g of sugar, 3.33 g of cellulose and 1.6 g of preventol D7. In one litre of liquid, adding 20 ml of water increases the relative *permittivity* by 0.8 and decreases the conductivity by 0.01 S/m. Adding 1 g of salt increases the conductivity by 0.05 S/m and decreases the relative permittivity by 0.8. Adding 60 g of sugar decreases the relative permittivity by 3.0 [121].

When the liquid was being prepared, the room temperature was 22.3 °C. The water was heated and stirred in a container. After 30 minutes, the water temperature was 26 °C. Salt, cellulose and preventol were added into the water and stirred. Once the liquid was transparent again, the sugar was added and stirred until it was completely dissolved. Then, the heat was removed and when the liquid was at room temperature, the dielectric properties were measured. Figure 6.1 shows the liquid preparation setup with the liquid container, hotplate/magnetic stirrer and thermometer. Figure 6.2 shows a detailed view
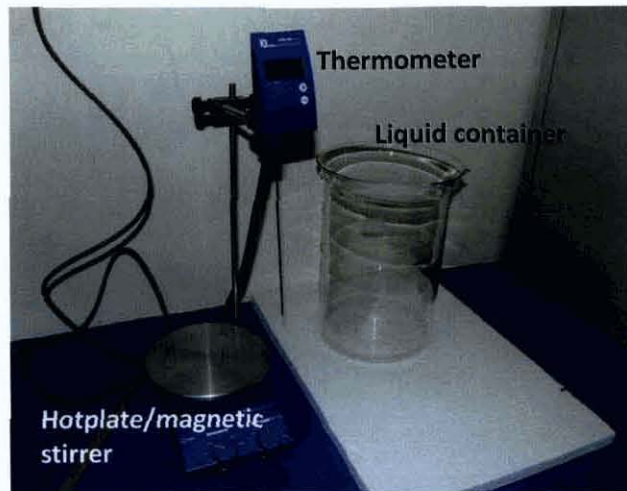
Figure 6.1.: Hotplate/magnetic stirrer, thermometer and liquid container.

of the liquid and magnetic stirrer with the temperature and stirrer speed controls.

6.2. Dielectric Properties of the Liquid

The Agilent 85070D dielectric probe kit was used to measure the dielectric properties of the liquid simulating homogeneous human tissue. The dielectric probe kit was connected to the Agilent 8510C vector network analyzer (VNA), and the Agilent 82357A USB-GPIB converter connected the VNA to a PC. Figure 6.3 shows a schematic representation of the setup for the measurement of the dielectric properties of the liquid.

Before the measurements can be performed, the system has to be calibrated in short circuit, open/air and load/water configuration as shown in Figure 6.4.

The liquid has to be at constant temperature and be perfectly homogeneous. With 1 °C of temperature increase the permittivity and conductivity increases and decreases respectively by about 0.5% and 1.0%. Air bubbles in the liquid can be a source of errors in the measurements. The measured dielectric properties of the liquid at the frequency of 434 MHz were found to be relative permittivity of 45.07 and conductivity of 0.82 S/m.
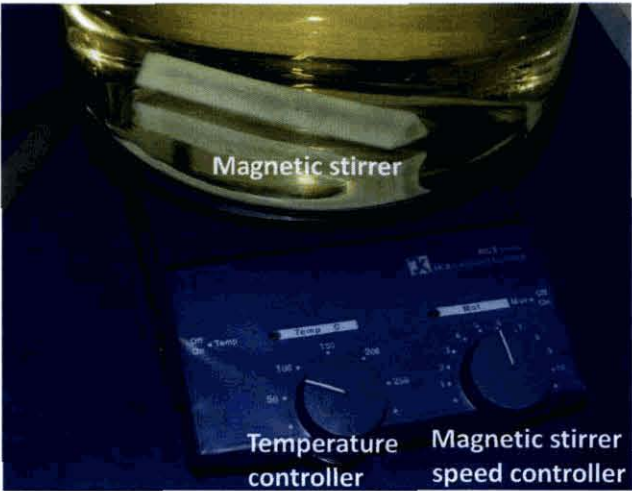
Figure 6.2.: Detail of the hotplate/magnetic stirrer.
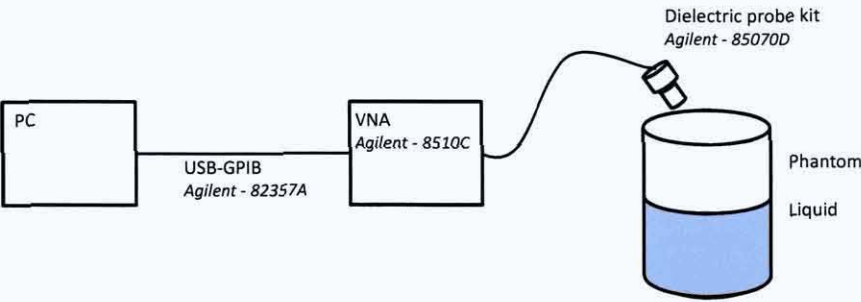
Figure 6.3.: Setup for the measurement of the dielectric properties of the liquid.
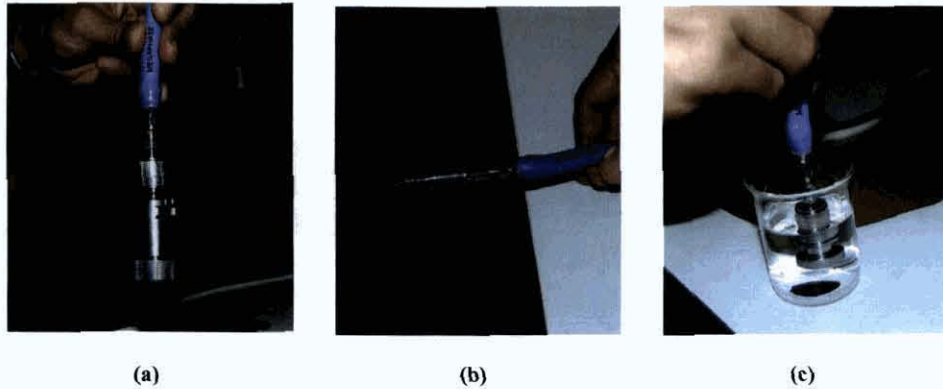
Figure 6.4.: Dielectric probe kit calibration (a) short circuit, (b) open/air and (c) load/water configuration.

6.3. DASY System

The Dosimetric Assessment System (DASY) is a measurement package which allows SAR distribution evaluation inside a lossy liquid contained in a phantom.

A PC with the DASY software is connected to the system, and the main parts that can be identified in the package are a measurement server, robot controller, robot, electro optical converter (EOC) box, data acquisition electronic (DAE) box, probe with proximity sensor, liquid, phantom and device holder. Figure 6.5 shows a schematic setup representation.

The DASY software controls the measurement server and monitors the robot exact location as shown in Figure 6.6. The measurement server communicates with the robot controller, and with the DAE via the EOC. The robot controller manages the robot movement. The EOC converts electro-optical signal between the measurement server and the DAE or proximity sensor which automatically detect the phantom surface. Figure 6.7 shows a detail of the proximity sensor and DAE connected to the EOC which it is located inside the robot arm. The DAE processes optical signal from the probe and sends the information to the measurement server. The probe measures the field that the antenna under test (AUT) generates inside the lossy liquid which is contained
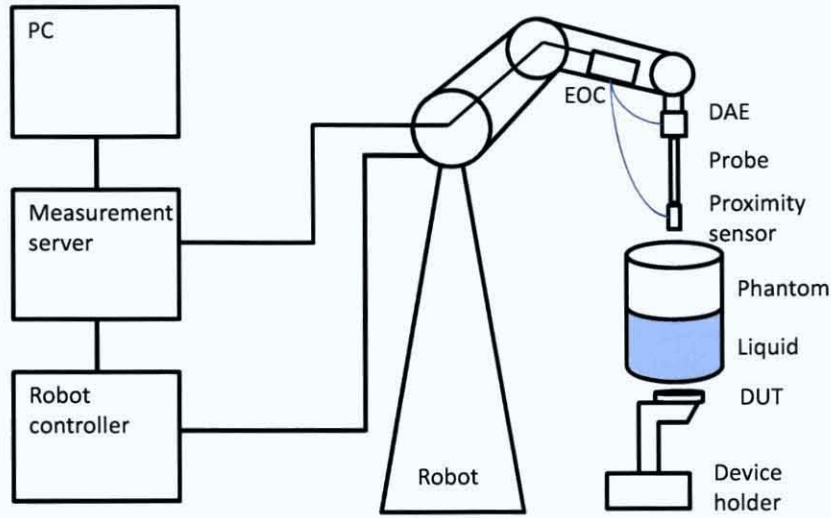
Figure 6.5.: DASY system measurement setup schematic representation.

in the phantom. Figure 6.8 shows a detailed view of the probe approximating to the lossy liquid. The device holder keeps the radiating antenna near the phantom at a fixed location during the measurement. A light beam unit is installed at a fixed, easily reached and safe position respect the robot which provides high precision alignment of the probe tip to the robot coordinate system with a red LED signal. Figure 6.9 shows a detailed view of the light beam unit aligning the probe.

6.4. Measurements

The antenna was located at a distance of 10 mm from the flat section of the phantom without using waterbolus as shown if Figure 6.10. SAR measurements were performed with the DASY system and S11 measurements with the Agilent 8510C network analyzer and 8517B S-parameter test set. The antenna-DASY system measurement setup was modelled on the XFDTD electromagnetic solver. The phantom was modelled with a 2 mm fibreglass shell [121] of $\varepsilon_r = 3.7$. Phantom and antenna dimensions are shown in Figure 6.11.
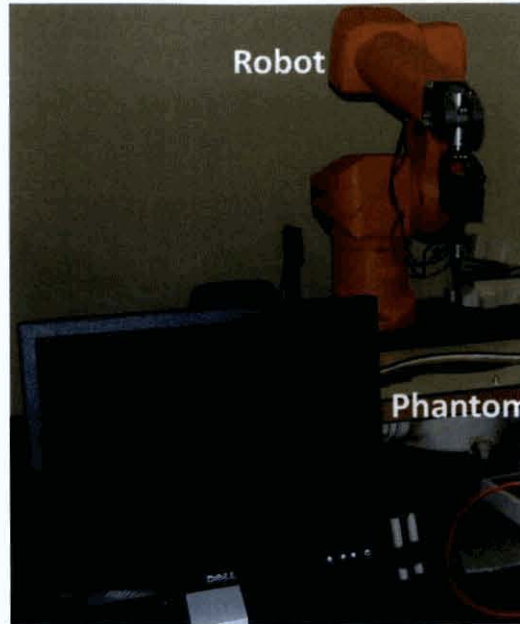
Figure 6.6.: The actual robot-phantom positioning is monitored in the PC.

6.4.1. SAR Measurements

The SAR presents a hotspot along the feed diagonal (FD) and an almost-symmetric distribution with the FD as axis of symmetry. The asymmetric shape of the phantom is why the SAR is not perfectly symmetric. The measurement shows a smaller amount of energy absorbed at the left side of the antenna compared to the simulation, where the distribution is similar in both right and left side. Simulated and measured SAR distribution is shown in Figure 6.12.

Peak SAR values were $1.76\,\mathrm{W/kg}$ and $1.68\,\mathrm{W/kg}$, the 50% iso-SAR covered an area of $67.25\,\mathrm{cm}^2$ and $65.25\,\mathrm{cm}^2$, and the 25% iso-SAR covered an area of $146\,\mathrm{cm}^2$ and $139\,\mathrm{cm}^2$ for simulation and measurement, respectively. This represents errors between simulation and measurement of 4.54%, 2.97% and 4.79%, for peak SAR, 50% iso-SAR and 25% iso-SAR areas respectively.

Distribution, peak SAR, and iso-SAR values between simulations and mea-
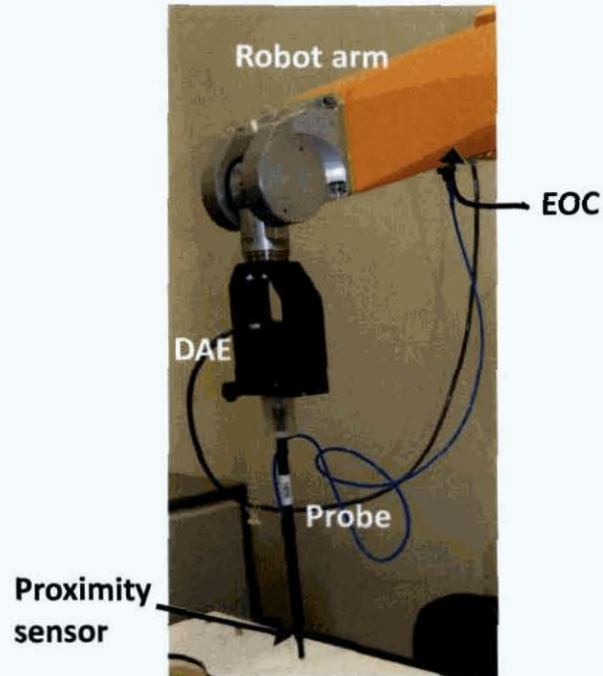
Figure 6.7.: Detail of the robot arm, DAE, proximity sensor, probe and EOC.
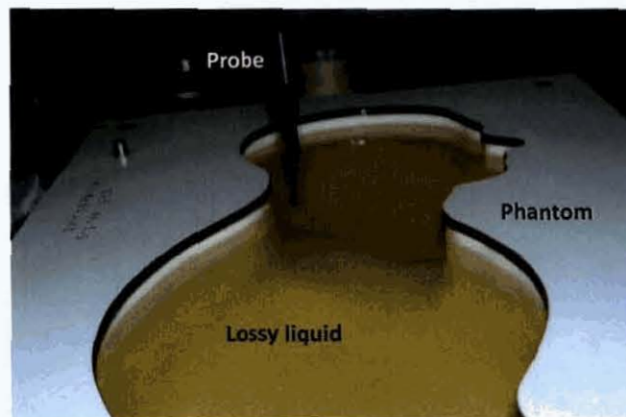
Figure 6.8.: Phantom with lossy liquid.
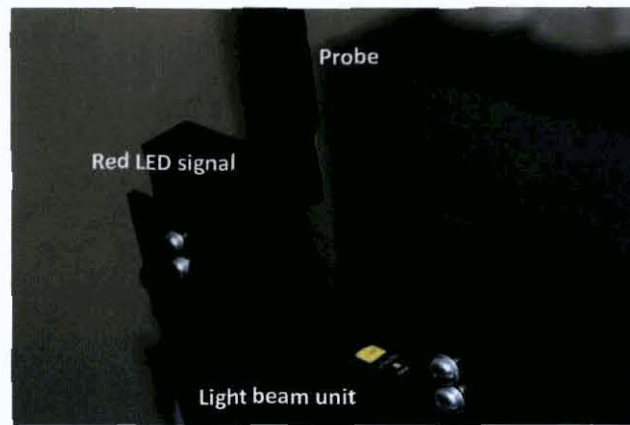
Figure 6.9.: Detail of the light beam unit aligning the probe.
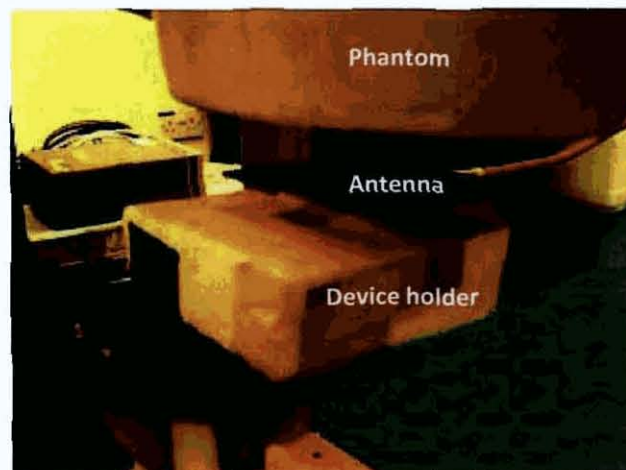
Figure 6.10.: Antenna located near the flat section of the phantom.
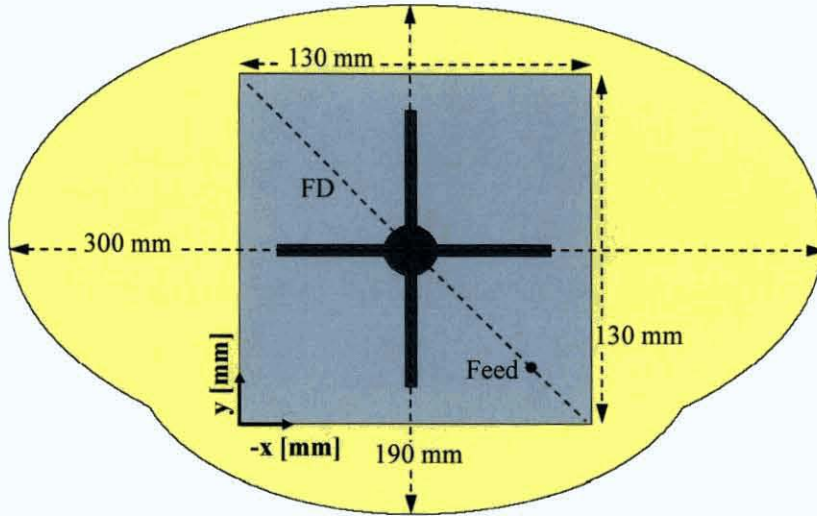
Figure 6.11.: Flat section of the phantom with antenna dimensions.

surements present good agreement. The differences are attributed to a slight non-parallel alignment of the antenna and measured phantom and the measurement system sensitivity to dielectric parameter accuracy.

Figure 6.13 shows the difference between simulated and measured SAR distribution. The maximum difference was 0.5 W/kg. The greater difference on the left side of the plot shows that this part of the antenna was farther from the phantom that the right side on the measurements.

Figure 6.14 shows the cumulative distribution function of the simulated and measured SAR results, where X is the SAR value and $F(X)$ is the proportion of SAR values less than or equal to a certain value. Good agreement is observed between simulation and measurement, especially at high SAR values.

6.4.2. S11 Measurements

The simulated and measured S11 for the antenna located at 10 mm from the DASY phantom is shown in Figure 6.15. Loading the antenna with the phantom containing the liquid detunes the resonant frequency by 7.7 MHz and
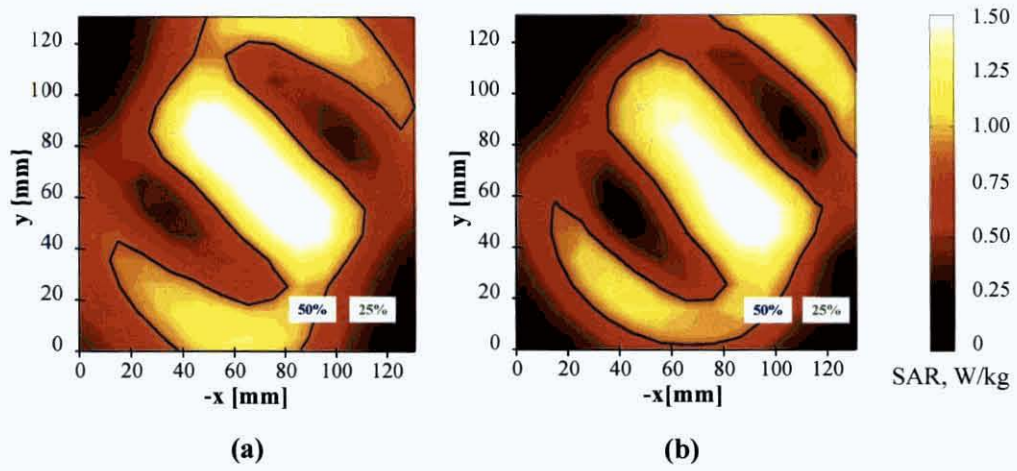
Figure 6.12.: SAR distribution (a) simulated and (b) measured.
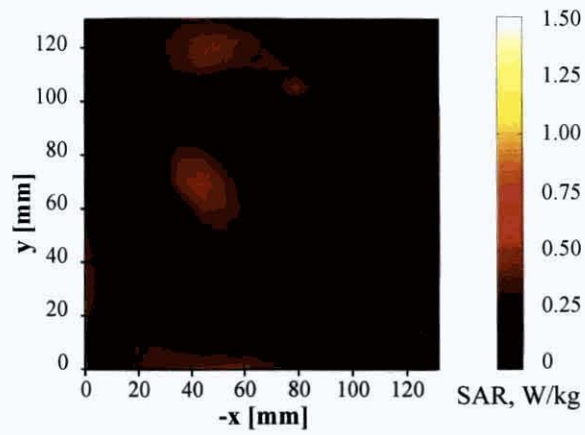
Figure 6.13.: SAR distribution of simulated less measured results. (a) – (b) in Figure 6.12.
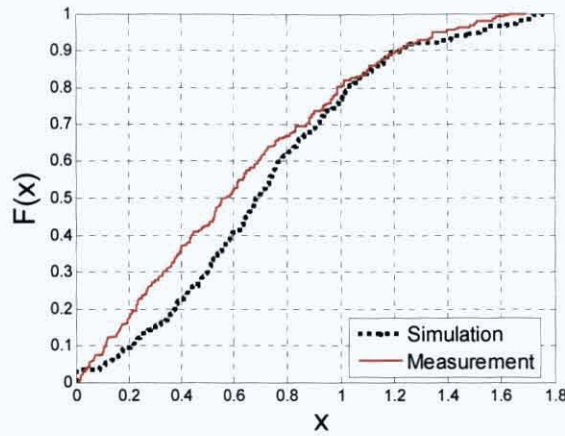
Figure 6.14.: Cumulative distribution fuction of simulated and measured SAR results.

9.1 MHz for the simulated and measured S11, respectively. The value of the S11 at the resonant frequency is -15.2 dB and -14.8 dB for the simulation and measurement respectively. The S11 at the 434 MHz source frequency is -9.51 dB and -10.9 dB for simulation and measurement respectively. The -8 dB bandwidth increases from 18.8 MHz (432.3 – 451 MHz) for the simulation up to 29.9 MHz (424.4 – 454.3 MHz) for the measurements.

The antenna was centered and parallel to the sagittal and coronal plane, respectively, at the epigastric location of a volunteer without using waterbolus. Figure 6.16 shows the antenna S11 when located at the distances between 20 mm and 0 mm from the body. It can be observed that the curves follow a similar trend and the S11 degrades as the antenna is located closer to the body.

6.5. Conclusions

While SAR measurements to generate energy absorption maps in actual human bodies (in-vivo) cannot be performed, liquids that simulate homogeneous
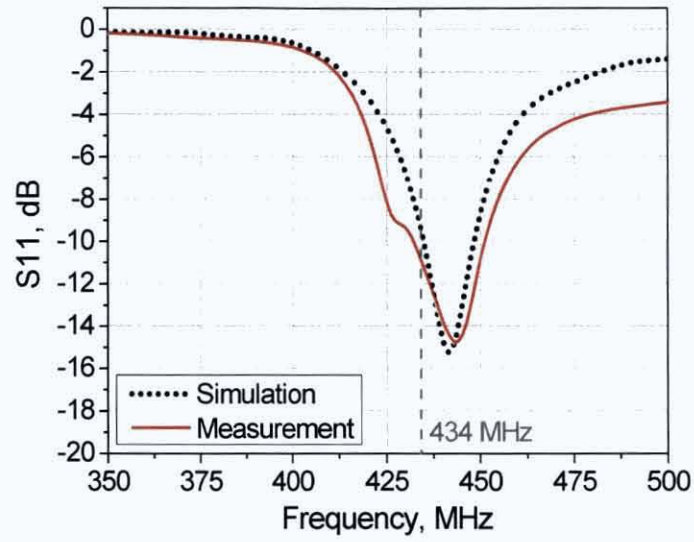
Figure 6.15.: Simulated and measured S11 for antenna at 10 mm from DASY phantom.
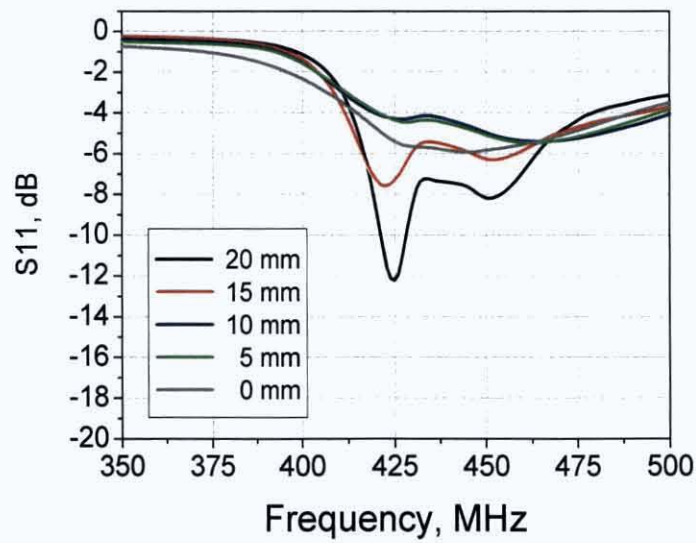
Figure 6.16.: Measured S11 for antenna at different distances of a volunteer.

human tissues have been developed. The validity of simulated electromagnetic models relies on the agreement between simulation and measurement performed in those liquids.

This chapter explains the preparation of the homogeneous human tissue simulating liquid at 434 MHz and how the dielectric properties were measured. The DASY system and its component parts was introduced. A comparison of measured SAR and S11 is made. Differences of 4.54%, 2.97% and 4.79% were obtained for the peak SAR, 50% iso-SAR and 25% iso-SAR respectively between measurements and simulations. S11 had also shown good agreement between measurements and simulations.

7. Conclusions and Future Work

T HIS chapter combines general conclusions of the thesis as well as some identified topics of relevant future work.

7.1. Conclusions

A multi-disciplinary work which merges the engineering and medical field in a comprehensive way to improve the understanding of antenna-human tissue interaction has been presented in this thesis. The goal of this work was to develop a compact antenna to efficiently deploy energy in human tissue for use as a hyperthermia applicator for cancer treatment. The work was carried out in the Antenna & High Frequency Research Centre at the Dublin Institute of Technology, Dublin; and in the RF and Optical Department at the Institute for Infocomm Research, Singapore.

The physics of hyperthermia, clinical trials and medical treatment were highlighted from the medical point of view. Different types of hyperthermia depending on the tumour physiological characteristics, dimensions, location and involved organs were described. Applicators for different hyperthermia types were outlined. The basics of antenna-human interaction, as well as the methodology to determine both specific absorption rate and temperature rise within the exposed tissue, were presented. The modelling and simulation methods used in this work were introduced.

The desirable features of antennas for medical applications and in particular

for hyperthermia as a cancer therapy have been identified. Antenna compactness for the treatment of tumors located on curved sites of the body, and the generation of tangential E-fields for coupling the energy into deeper tissues without damaging superficial tissues are some of the criteria for determining the suitability of a hyperthermia applicator. Low frequency of operation is required in order to get deep penetration. However, the frequency of operation is inversely proportional to antenna size and, consequently, miniaturization techniques are necessary. The antenna has to be well matched to the system frequency for different tissue loading conditions.

A compact patch antenna operating at the frequency of 434 MHz has been developed. The design steps and miniaturization process have been detailed. The antenna was initially designed in free space and later optimized next to human tissue. The antenna evolved from a conventional circular patch to an annular ring with concentric circular patch and slotted groundplane, which realised an area size reduction of 65.08%. The design overcomes the geometrical constraints of other applicators. The feed location was optimized in terms of input impedance, E-field distribution and specific absorption rate in a homogeneous muscle tissue.

The merits of the compact antenna have been compared with previously published applicators. A detailed performance evaluation of clinically used dipoles, loop and square patch antennas was shown in terms of S11, E-field and SAR distribution patterns. The proposed applicator has shown an enhanced specific absorption rate pattern without significant frequency detuning or impedance mismatch when the antenna was loaded with a tri-layer tissue model. The human model comprised layers of skin, fat and muscle of variable thickness to account for different patients and tissues. The dominant tangential E-fields produced greater coupling with a $1/e^2$ SAR penetration depth of 63 mm which exceeds the performance of other waveguides, horn and microstrip designs.

The full human body model, based on data from the Visible Human Project and developed by Remcom, was used to assess the performance with a more

realistic human body. This model comprised twenty-three dielectric and thermally frequency-dependent clusters of tissues. The antenna was evaluated at the epigastric, inter-scapular and head anatomical regions. These locations present different antenna aperture loading and different tissue composition. The thickness of the conformal waterbolus and air gap between antenna and waterbolus was evaluated for each location. Performance in terms of S11, SAR and temperature distribution was shown. The required power source to produce a temperature increase up to 43 °C for each of the considered body regions was investigated. The higher perfusion of the tissues at the inter-scapular location demands a greater increase in required power source when doubling the tissue perfusion to get the 43 °C threshold.

In other to validate the model, measurements were performed with the Dosimetric Assessment System (DASY) package. A liquid simulating homogeneous human tissue at 434 MHz was produced. The liquid composition, preparation process and dielectric properties measurement were detailed. The phantom of the DASY system was filled with this liquid. The specific absorption rate and the S11 for the compact antenna in proximity to the phantom were measured. The measurement setup was modeled in the XFDTD electromagnetic solver. Good agreement between measurements and simulations in terms of SAR and S11 was obtained.

7.2. Future Work

Many techniques have been investigated to reduce the rearward radiation from microstrip patch antennas. Filled cavity-backed patch antennas can suppress surface waves [122], however as back radiation depends on the surface surrounding the antennas, planar soft surfaces have been efficiently used [123]. Suppressing the antenna back radiation in a clinical environment can be beneficial for clinicians and EM compatibility with other equipments. Further analysis can focus on evaluating the antenna in a realistic clinical environment
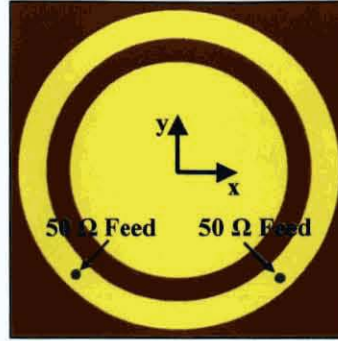
Figure 7.1.: Geometry of compact patch antenna with two feed ports.

and designing a miniaturized effective soft surface in order to suppress possible rearward radiation.

It has been shown that the addition of a feed port to a patch antenna can modify the patch current distribution [124]. Possible future work could focus on the optimization of a second feed port position on the annular ring of the compact patch antenna as shown in Figure 7.1. Two highly decoupled feed ports could increase the current distribution on the patch and generate a greater SAR distribution in the tissue.

The computational time of electromagnetic simulations is a function of mesh refinement and it is an important issue when modeling complex geometries such as the human body. When improved computational resources become available, a finer mesh of would improve the model accuracy without compromising the computational time.

Actual tissue thermal and dielectric properties differ among patients [43]. Tissue blood perfusion varies spatially and temporally during treatment [104]. Further research could be devoted to improve the understanding on dielectric properties and perfusion mechanisms in healthy and tumour tissue, and to use adaptive models, which can lead to a more accurate temperature analysis.

The contrast in dielectric properties between healthy and tumour tissue is

the basis of microwave cancer detection [125]. In addition, dielectric properties of liver tissue in the frequency range between 0.5 and 20 GHz have been shown to be temperature-dependant [126]. Further investigations could analyse the dependence of dielectric properties on temperature, for both healthy and tumour tissues. It will be valuable research to determine whether exposing tissue to hyperthermia produces an increased dielectric contrast between tumour and healthy tissue (temperature increases more in tumour than in healthy tissue for the same incident E-field) which can facilitate tumour detection and/or progress monitoring with a microwave imaging system. Research can focus on combining a hyperthermia and a microwave imaging system.

The development of medical implants as pacemakers, sphincter sensors or intracranial pressure sensor has increased in the last few years [127] and they require advanced external devices to communicate with. The developed compact patch antenna could be used to communicate with these and others medical implants.

While model validation had been proved performing S11 and SAR measurements in a liquid simulating homogeneous human tissue at the frequency of 434 MHz further possible investigation should focus on the evaluation of antenna performance in clinical experiments.

Bibliography

EACH bibliographic entry specifies the page number where it was cited. For electronic references, the URL and date when they were accessed are indicated.

[1] American Cancer Society. (2010, April). [Online]. Available: http://www.cancer.org/ (Cited on Page 1)

[2] P. Boyle and J. Ferlay, "Cancer incidence and mortality in Europe, 2004," *Annals of Oncology*, vol. 16, no. 3, pp. 481–488, 2005. (Cited on Page 1)

[3] WHO – World Health Organization. (2010, April). [Online]. Available: http://www.who.int/en/ (Cited on Page 1)

[4] National Cancer Institute. (2010, April). [Online]. Available: http://www.cancer.gov/ (Cited on Page 1)

[5] J. Van der Zee, "Heating the patient: a promising approach?" *Annals of Oncology*, vol. 13, no. 8, pp. 1173–1184, 2002. (Cited on Pages 1, 2, 6, 7, 8, and 9)

[6] M. R. Horsman and J. Overgaard, "Hyperthermia: a potent enhancer of radiotherapy," *Clinical Oncology*, vol. 19, no. 6, pp. 418–426, Aug. 2007. (Cited on Pages 2, 8, 11, and 13)

[7] P. Wust, B. Hildebrandt, G. Sreenivasa, B. Rau, J. Gellermann, H. Riess, R. Felix, and P. M. Schlag, "Hyperthermia in combined treatment of cancer," *The Lancet Oncology*, vol. 3, no. 8, pp. 487–497, Aug. 2002. (Cited on Pages 1, 7, 10, and 11)

[8] A. Chicheł, J. Skowronek, M. Kubaszewska, and M. Kanikowski, "Hyperthermia - description of a method and a review of clinical applications," *Reports of Practical Oncology and Radiotherapy*, vol. 12, no. 5, pp. 267–275, 2007. (Cited on Pages 1, 8, 9, 10, and 11)

[9] C. Chou, "Evaluation of microwave hyperthermia applicators," *Bioelectromagnetics*, vol. 13, no. 6, pp. 581–597, Jun. 1992. (Cited on Pages 3 and 14)

[10] N. Ichinoseki-Sekine, H. Naito, N. Saga, Y. Ogura, M. Shiraishi, A. Giombini, V. Giovannini, and S. Katamoto, "Changes in muscle temperature induced by 434 MHz microwave hyperthermia," *British Journal of Sports Medicine*, vol. 41, no. 7, pp. 425–429, Jan. 2007. (Cited on Page 6)

[11] J. H. Breasted, "The Edwin Smith surgical papyrus," *University of Chicago Press Chicago*, 1930. (Cited on Page 7)

[12] F. K. Storm and D. L. Morton, "Localized hyperthermia in the treatment of cancer," *Cancer Journal for Clinicians*, vol. 33, no. 1, pp. 44–56, Jan. 1983. (Cited on Page 7)

[13] F. K. Storm, R. Elliott, W. H. Harrison, and D. L. Morton, "Hyperthermia in cancer treatment: Potential and progress," *Practice Oncology for the Primary Care Physician*, vol. 1, pp. 42–52, 1980. (Cited on Page 7)

[14] J. G. Short and P. F. Turner, "Physical hyperthermia and cancer therapy," *Proceedings of the IEEE*, vol. 68, no. 1, pp. 133–142, Jan. 1980. (Cited on Page 7)

[15] A. Y. Cheung and A. Neyzari, "Deep local hyperthermia for cancer therapy: external electromagnetic and ultrasound techniques," *Cancer Research*, vol. 44, no. 1, pp. 4736–4744, Oct. 1984. (Cited on Pages 7 and 13)

[16] M. Dollinger, E. H. Rosenbaum, M. Tempero, and S. Mulvihill, *Everyone's Guide to Cancer Therapy: How Cancer is Diagnosed, Treated, and*

Managed Day to Day, fourth edition ed. USA: Andrews McMeel Publishing, 2002. (Cited on Pages 7, 10, and 22)

[17] M. W. Dewhirst and D. A. Sim, "Estimation of therapeutic gain in clinical trials involving hyperthermia and radiotherapy," *International Journal of Hyperthermia*, vol. 2, no. 2, pp. 165–178, 1986. (Cited on Page 7)

[18] W. C. Dewey, "Arrhenius relationships from the molecule and cell to the clinic," *International Journal of Hyperthermia*, vol. 10, no. 4, pp. 457–483, 1994. (Cited on Page 7)

[19] STM – Society for Thermal Medicine. (2010, April). [Online]. Available: http://www.thermaltherapy.org (Cited on Page 7)

[20] ASHO – Asian Society of Hyperthermic Oncology. (2010, April). [Online]. Available: http://www.jsho.jp/index.php?option= com_content&task=blogcategory&id=35&Itemid=32 (Cited on Page 7)

[21] ESHO – European Society for Hyperthermic Oncology. (2010, April). [Online]. Available: http://www.esho.info/ (Cited on Page 7)

[22] M. Franckena, D. Fatehi, M. Bruijne, R. A. M. Canters, Y. Norden, J. W. Mens, G. C. Van Rhoon, and J. Van der Zee, "Hyperthermia dose-effect relationship in 420 patients with cervical cancer treated with combined radiotherapy and hyperthermia," *European Journal of Cancer*, vol. 45, no. 11, pp. 1969–1978, 2009. (Cited on Pages 8 and 11)

[23] J. A. Holt, "The extra nuclear control of mitosis & cell function. a theory of cellular organization," *Medical Hypotheses*, vol. 6, no. 2, pp. 145–192, 1980. (Cited on Page 9)

[24] O. Warburg, "The prime cause and prevention of cancer," in *Revised lecture at the meeting of the Nobel laureates*, Jun. 1966. (Cited on Page 9)

[25] P. R. Stauffer, "Evolving technology for thermal therapy of cancer," *International Journal of Hyperthermia*, vol. 21, no. 8, pp. 731–744, Dec. 2005. (Cited on Page 9)

[26] T. Samaras, P. J. M. Rietveld, and G. C. Van Rhoon, "Effectiveness of FDTD in predicting SAR distributions from the Lucite cone applicator," *IEEE Transactions on Microwave Theory and Techniques*, vol. 48, no. 11, pt. 2, pp. 2059–2063, Nov. 2000. (Cited on Pages 9, 40, and 41)

[27] I. J. Bahl, S. S. Stuchly, J. W. Lagendijk, and M. A. Stuchly, "Microstrip loop radiators for local hyperthermia," in *Proc. IEEE MTT International Microwave Symposium*, 1981, pp. 465–467. (Cited on Pages 9, 40, 41, and 57)

[28] P. Gabriele, T. Ferrara, B. Baiotto, E. Garibaldi, P. G. Marini, G. Penduzzu, V. Giovannini, F. Bardati, and C. Guiot, "Radio hyperthermia for re-treatment of superficial tumours," *International Journal of Hyperthermia*, vol. 25, no. 3, pp. 189–198, May 2009. (Cited on Page 10)

[29] K. Saito, H. Yoshimura, K. Ito, Y. Aoyagi, and H. Horita, "Clinical trials of interstitial microwave hyperthermia by use of coaxial-slot antenna with two slots," *IEEE Transactions on Microwave Theory and Techniques*, vol. 52, no. 8, part 2, pp. 1987–1991, Aug. 2004. (Cited on Pages 10 and 26)

[30] D. Fatehi and G. C. Van Rhoon, "SAR characteristics of the Sigma-60 Ellipse applicator," *International Journal of Hyperthermia*, vol. 24, no. 4, pp. 347–356, Jun. 2008. (Cited on Page 10)

[31] J. Van der Zee, D. González González, G. C. Van Rhoon, J. D. P. Van Dijk, W. L. J. Van Putten, and A. A. M. Hart, "Comparison of radiotherapy alone with radiotherapy plus hyperthermia in locally advanced pelvic tumours: a prospective, randomised, multicentre trial," *The Lancet*, vol. 355, pp. 1119–1125, 2000. (Cited on Page 12)

[32] M. Sherar, F. F. Liu, M. Pintilie, W. Levin, J. Hunt, R. Hill, J. Hand, C. Vernon, G. C. Van Rhoon, J. Van der Zee, D. González González, J. Van Duk, J. Whaley, and D. Machin, "Relationship between thermal dose and outcome in thermoradiotherapy treatments for superficial recurrences of breast cancer: data from a phase III trial," *International Journal of Radiation Oncology, Biology and Physics*, vol. 39, no. 2, pp. 371–380, 1997.   (Cited on Page 12)

[33] M. Franckena, L. J. A. Stalpers, P. C. M. Koper, R. G. J. Wiggenraad, W. J. Hoogenraad, J. D. P. Van Dijk, C. C. Wárlám-Rodenhuis, J. J. Jobsen, G. C. Van Rhoon, and J. Van der Zee, "Long-term improvement in treatment outcome after radiotherapy and hyperthermia in locoregionally advanced cervix cancer: An update of the dutch deep hyperthermia trial," *International Journal of Radiation Oncology, Biology and Physics*, vol. 70, no. 4, pp. 1176–1182, Mar. 2008.   (Cited on Page 12)

[34] N. R. Datta, A. K. Bose, H. K. Kapoor, and S. Gupta, "Head and neck cancers: results of thermoradiotherapy versus radiotherapy," *International Journal of Hyperthermia*, vol. 6, no. 3, pp. 479–486, 1990.   (Cited on Page 12)

[35] J. Overgaard, D. González González, M. Hulshof, G. Arcangeli, O. Dahl, O. Mella, and S. M. Bentzen, "Hyperthermia as an adjuvant to radiation therapy of recurrent or metastatic malignant melanoma. A multicentre randomized trial by the European Society for Hyperthermic Oncology," *International Journal of Hyperthermia*, vol. 25, no. 5, pp. 323–334, Aug. 2009.   (Cited on Page 12)

[36] B. A. Berdov and G. Z. Menteshashvili, "Thermoradiotherapy of patients with locally advanced carcinoma of the rectum," *International Journal of Hyperthermia*, vol. 6, no. 5, pp. 881–890, 1990.   (Cited on Page 12)

[37] E. L. Jones, J. R. Oleson, L. R. Prosnitz, T. V. Samulski, Z. Vujaskovic,

D. Yu, L. L. Sanders, and M. W. Dewhirst, "Randomized trial of hyperthermia and radiation for superficial tumors," *Journal of Clinical Oncology*, vol. 23, no. 13, pp. 3079–3085, May 2005. (Cited on Page 12)

[38] R. Colombo, L. F. Da Pozzo, A. Salonia, P. Rigatti, Z. Leib, J. Baniel, E. Caldarera, and M. Pavone-Macaluso, "Multicentric study comparing intravesical chemotherapy alone and with local microwave hyperthermia for prophylaxis of recurrence of superficial transitional cell carcinoma," *Journal of Clinical Oncology*, vol. 21, no. 23, pp. 4270–4276, Dec. 2003. (Cited on Pages 12 and 13)

[39] V. J. Verwaal, S. Van Ruth, E. de Bree, G. W. Van Slooten, H. Van Tinteren, H. Boot, and F. A. N. Zoetmulder, "Randomized trial of cytoreduction and hyperthermic intraperitoneal chemotherapy versus systemic chemotherapy and palliative surgery in patients with peritoneal carcinomatosis of colorectal cancer," *Journal of Clinical Oncology*, vol. 21, no. 20, pp. 3737–3743, Oct. 2003. (Cited on Page 12)

[40] J. F. Bakker, M. M. Paulides, I. M. Obdeijn, G. C. Van Rhoon, and K. W. Van Dongen, "An ultrasound cylindrical phased array for deep heating in the breast: theoretical design using heterogeneous models," *Physics in Medicine and Biology*, vol. 54, no. 10, pp. 3201–3215, May 2009. (Cited on Page 13)

[41] J. J. W. Lagendijk, "Hyperthermia treatment planning," *Physics in Medicine and Biology*, vol. 45, no. 1, pp. 61–76, 2000. (Cited on Page 14)

[42] M. Weihrauch, P. Wust, M. Weiser, J. Nadobny, S. Eisenhardt, V. Budach, and J. Gellermann, "Adaptation of antenna profiles for control of MR guided hyperthermia (HT) in a hybrid MR-HT system," *Medical Physics*, vol. 34, no. 1, pp. 1–20, 2007. (Cited on Page 14)

[43] V. L. Stakhursky, O. Arabe, K. S. Cheng, J. MacFall, P. Maccarini, O. Craciunescu, M. Dewhirst, P. R. Stauffer, and S. K. Das, "Real-time

MRI-guided hyperthermia treatment using a fast adaptive algorithm," *Physics in Medicine and Biology*, vol. 54, no. 1, pp. 2131–2145, Mar. 2009. (Cited on Pages 14, 16, and 97)

[44] O. I. Craciunescu, P. R. Stauffer, B. J. Soher, C. R. Wyatt, O. Arabe, P. Maccarini, S. K. Das, K. S. Cheng, T. Z. Wong, E. L. Jones, M. W. Dewhirst, Z. Vujaskovic, and J. R. MacFall, "Accuracy of real time noninvasive temperature measurements using magnetic resonance thermal imaging in patients treated for high grade extremity soft tissue sarcomas," *Medical Physics*, vol. 36, no. 1, pp. 4848–4858, 2009. (Cited on Page 14)

[45] J. W. Hand, J. L. Cheetham, and A. J. Hind, "Absorbed power distributions from coherent microwave arrays for localized hyperthermia," *IEEE Transactions on Microwave Theory and Techniques*, vol. 34, no. 5, pp. 484–489, May 1986. (Cited on Page 15)

[46] R. C. Gupta and S. P. Singh, "Analysis of the SAR distributions in three-layered bio-media in direct contact with a water-loaded modified box-horn applicator," *IEEE Transactions on Microwave Theory and Techniques*, vol. 53, no. 9, pp. 2665–2671, Sep. 2005. (Cited on Pages 15, 40, and 41)

[47] J. A. G. Holt, "Increase in X-ray sensitivity of cancer after exposure to 434 MHz electromagnetic radiation," *Journal of Bioengineering*, vol. 1, pp. 479–485, Jun. 1977. (Cited on Pages 15 and 41)

[48] J. Keshvari, R. Keshvari, and S. Lang, "The effect of increase in dielectric values on specific absorption rate (SAR) in eye and head tissues following 900, 1800 and 2450 MHz radio frequency (RF) exposure," *Physics in Medicine and Biology*, vol. 51, no. 6, pp. 1463–1477, Mar. 2006. (Cited on Page 15)

[49] IFAC CNR – Institute for Applied Physics. Italian national research council. (2010, April). [Online]. Available: http://niremf.ifac.cnr.it/tissprop/ (Cited on Pages 15, 20, 42, and 59)

[50] A. Van der Vorst, A. Rosen, and Y. Kotsuka, *RF/Microwave Interaction with Biological Tissues*. Wiley-IEEE Press, 2006. (Cited on Page 15)

[51] W. T. Joines, Y. Zhang, C. Li, and R. L. Jirtle, "The measured electrical properties of normal and malignant human tissues from 50 to 900 MHz," *Medical Physics*, vol. 21, no. 4, pp. 547–550, Apr. 1994. (Cited on Page 16)

[52] R. A. Kruger, K. D. Miller, H. E. Reynolds, W. L. Kiser, D. R. Reinecke, and G. A. Kruger, "Breast cancer in vivo: Contrast enhancement with thermoacoustic CT at 434 MHz-feasibility study," *Radiology*, vol. 216, no. 1, pp. 279–283, 2000. (Cited on Page 18)

[53] *IEEE Recommended practice for measurements and computations of radio frequency electromagnetic fields with respect to human exposure to such fields, 100 kHz - 300 GHz*, IEEE Std. C95.3-2002 (Revision of IEEE Std. C95.3-1991), 2002. (Cited on Pages 18 and 20)

[54] H. H. Pennes, "Analysis of tissue and arterial blood temperatures in the resting human forearm," *Journal of Applied Physiology*, vol. 1, pp. 93–122, Aug. 1948. (Cited on Pages 21 and 60)

[55] J. Wang and O. Fujiwara, "FDTD computation of temperature rise in the human head for portable telephones," *IEEE Transactions on Microwave Theory and Techniques*, vol. 47, no. 8, pp. 1528–1534, Aug. 1999. (Cited on Page 22)

[56] *XFDTD Full-wave, 3D electromagnetic analysis software. Users Guide*, REMCOM, 2005. (Cited on Page 22)

[57] CST GmbH – Computer Simulation Technology. (2010, April). [Online]. Available: http://www.cst.com (Cited on Pages 23 and 43)

[58] REMCOM – Electromagnetic Simulation Software. (2010, April). [Online]. Available: http://www.remcom.com/ (Cited on Pages 23, 58, and 61)

[59] K. S. Yee, "Numerical solution of initial boundary value problems involving Maxwell's equations in isotropic media," *IEEE Transaction on Antennas and Propagation*, vol. 14, no. 3, pp. 302–307, 1966.   (Cited on Page 23)

[60] T. Weiland, "A discretization model for the solution of Maxwell's equations for six-component fields," *Archiv Elektronik und Uebertragungstechnik*, vol. 31, pp. 116–120, 1977.   (Cited on Page 23)

[61] A. Taflove, "Application of the finite-difference time-domain method to sinusoidal steady-state electromagnetic-penetration problems," *IEEE Transactions on Electromagnetic Compatibility*, vol. 22, no. 3, pp. 191–202, Aug. 1980.   (Cited on Page 23)

[62] A. Rosen, M. A. Stuchly, and A. Van der Vorst, "Applications of RF/Microwaves in medicine," *IEEE Transactions on Microwave Theory and Techniques*, vol. 50, no. 3, pp. 963–974, Mar. 2002.
(Cited on Pages 24 and 26)

[63] E. C. Fear, "Microwave imaging of the breast," *Technology in Cancer Research and Treatment*, vol. 4, no. 1, pp. 69–82, Feb.   (Cited on Page 24)

[64] D. Adang and A. Van der Vorst, "First results of a long-term epidemiological study on low-level microwave exposure of rats," in *Proc. IEEE MTT International Microwave Symposium*, 2006, pp. 1742–1745.
(Cited on Page 24)

[65] C. H. Durney, "Antennas and other electromagnetic applicators in biology and medicine," *Proceedings of the IEEE*, vol. 80, no. 1, pp. 194–199, 1992.   (Cited on Page 25)

[66] G. C. Van Rhoon, A. G. Visser, P. M. Van den Berg, and H. S. Reinhold, "Evaluation of ring capacitor plates for regional deep heating," *International Journal of Hyperthermia*, vol. 4, no. 2, pp. 133–142, 1988.
(Cited on Page 25)

[67] F. K. Storm, R. S. Elliott, W. H. Harrison, and D. Morton, "Clinical RF hyperthermia by magnetic-loop induction: a new approach to human cancer therapy," *IEEE Transactions on Microwave Theory and Techniques*, vol. 30, no. 8, pp. 1149–1158, Aug. 1982. (Cited on Page 25)

[68] J. C. Camart, J. J. Fabre, B. Prevost, J. Pribetich, and M. Chive, "Coaxial antenna array for 915 MHz interstitial hyperthermia: design and modelization-power deposition and heating pattern-phased array," *IEEE Transactions on Microwave Theory and Techniques*, vol. 40, no. 12, pp. 2243–2250, Dec. 1992. (Cited on Page 26)

[69] B. Thiesen and A. Jordan, "Clinical applications of magnetic nanoparticles for hyperthermia," *International Journal of Hyperthermia*, vol. 24, no. 6, pp. 467–474, Sep. 2008. (Cited on Page 26)

[70] M. M. Paulides, J. F. Bakker, N. Chavannes, and G. C. Van Rhoon, "A patch antenna design for application in a phased-array head and neck hyperthermia applicator," *IEEE Transactions on Biomedical Engineering*, vol. 54, no. 11, pp. 2057–2063, Nov. 2007. (Cited on Pages 26, 27, 40, and 44)

[71] O. M. Ramahi and R. Mittra, "Design of a matching network for an HF antenna using the realfrequency method," *IEEE Transactions on Antennas and Propagation*, vol. 37, no. 4, pp. 506–509, Apr. 1989. (Cited on Page 27)

[72] Y. Nikawa and F. Okada, "Dielectric-loaded lens applicator for microwave hyperthermia," *IEEE Transactions on Microwave Theory and Techniques*, vol. 39, no. 7, pp. 1173–1178, Jul. 1991. (Cited on Page 27)

[73] M. J. Ammann, S. Curto, X. L. Bao, and P. McEvoy, "Antenna design considerations for high specific absorption rate in local hyperthermia treatment," in *Proc. IEEE AP-S International Symposium on Antennas and Propagation*, 2008, pp. 1–4. (Cited on Page 27)

[74] C. A. Balanis, *Antenna Theory, Analysis and Design*, 3rd ed. New York: John Wiley & Sons, 2005. (Cited on Pages 28 and 41)

[75] R. Bancroft, *Microstrip and Printed Antenna Design*. Atlanta: Noble Publishing Associates, 2004. (Cited on Page 28)

[76] J. C. Kumaradas and M. D. Sherar, "Optimization of a beam shaping waterbolus for superficial microwave hyperthermia waveguide applicators using a finite element method," *Physics in Medicine and Biology*, vol. 7, no. 48, pt. 1, pp. 1–18, 2003. (Cited on Page 40)

[77] M. L. Van der Gaag, M. de Bruijne, T. Samaras, J. Van der Zee, and G. C. Van Rhoon, "Development of a guideline for the waterbolus temperature in superficial hyperthermia," *International Journal of Hyperthermia*, vol. 22, no. 8, pp. 637–656, Dec. 2006. (Cited on Page 40)

[78] W. G. Scanlon, B. Burns, and N. E. Evans, "Radiowave propagation from a tissue-implanted source at 418 MHz and 916.5 MHz," *IEEE Transactions on Biomedical Engineering*, vol. 47, no. 4, pp. 527–534, Apr. 2000. (Cited on Page 40)

[79] Z. N. Chen, A. Cai, T. S. P. See, X. Qing, and M. Y. W. Chia, "Small planar UWB antennas in proximity of the human head," *IEEE Transactions on Microwave Theory and Techniques*, vol. 54, no. 4, pt. 2, pp. 1846–1857, Apr. 2006. (Cited on Page 40)

[80] E. Tafeit, R. Möller, K. Sudi, R. Horejsi, A. Berg, and G. Reibnegger, "Orthogonal factor coefficient development of subcutaneous adipose tissue topography in girls and boys," *American Journal of Physical Anthropology*, vol. 115, no. 1, pp. 57–61, 2001. (Cited on Pages 40 and 43)

[81] R. Moller, E. Tafeit, and T. R. Pieber, "Measurement of subcutaneous adipose tissue topography (SAT-Top) by means of a new optical device, LIPOMETER and the evaluation of standard factor coefficients in

healthy subjects," *American Journal of Human Biology*, vol. 12, no. 2, pp. 231–239, 2000.

[82] W. S. Snyder, M. J. Cook, E. S. Nasset, L. R. Karhausen, G. P. Howells, and I. H. Tipton, *Report of the task group on reference man. International Commission on Radiological Protection*, 1st ed. Oxford: Pergamon Press, 1975. (Cited on Pages 40 and 43)

[83] P. Wust, H. Fähling, W. Wlodarczyk, M. Seebass, J. Gellermann, P. Deuflhard, and J. Nadobny, "Antenna arrays in the SIGMA-Eye applicator: interactions and transforming networks," *Medical Physics*, vol. 28, no. 8, pp. 1793–1805, Aug. 2001. (Cited on Pages 40 and 41)

[84] P. F. Maccarini, H. O. Rolfsnes, D. Neuman, J. Johnson, T. Juang, and P. R. Stauffer, "Advances in microwave hyperthermia of large superficial tumors," in *Proc. IEEE MTT International Microwave Symposium*, 2005, pp. 1797–1800. (Cited on Page 40)

[85] K. Arunachalam, B. Maccarini, T. Juang, C. Gaeta, and P. R. Stauffer, "Performance evaluation of a conformal thermal monitoring sheet sensor array for measurement of surface temperature distributions during superficial hyperthermia treatments," *International Journal of Hyperthermia*, vol. 24, no. 4, pp. 313–325, Jun. 2008. (Cited on Page 40)

[86] E. A. Gelvich and V. N. Mazokhin, "Contact flexible microstrip applicators (CFMA) in a range from microwaves up to short waves," *IEEE Transactions on Biomedical Engineering*, vol. 49, no. 9, pp. 1015–1023, Sep. 2002. (Cited on Page 40)

[87] W. Guy, "Electromagnetic fields and relative heating patterns due to a rectangular aperture source in direct contact with bilayered biological tissue," *IEEE Transactions on Microwave Theory and Techniques*, vol. 19, no. 2, pp. 214–223, Feb. 1971. (Cited on Pages 40 and 41)

[88] K. S. Nikita and N. K. Uzunoglu, "Analysis of the power coupling from a waveguide hyperthermia applicator into a three-layered tissue model," *IEEE Transactions on Microwave Theory and Techniques*, vol. 37, no. 11, pp. 1794–1801, Nov. 1989. (Cited on Pages 40 and 41)

[89] F. Montecchia, "Microstrip-antenna design for hyperthermia treatment of superficial tumors," *IEEE Transactions on Biomedical Engineering*, vol. 39, no. 6, pp. 580–588, Jun. 1992. (Cited on Page 40)

[90] J. Carlier, V. Thomy, J. C. Camart, L. Dubois, and J. Pribetich, "Modeling of planar applicators for microwave thermotherapy," *IEEE Transactions on Microwave Theory and Techniques*, vol. 50, no. 12, pp. 3036–3042, Dec. 2002. (Cited on Page 40)

[91] D. Andreuccetti, M. Bini, A. Ignesti, R. Olmi, S. Priori, and R. Vanni, "High permittivity patch radiator for single and multi-element hyperthermia applicators," *IEEE Transactions on Biomedical Engineering*, vol. 40, no. 7, pp. 711–715, Jul. 1993. (Cited on Pages 40 and 41)

[92] L. Beyne and D. D. Zutter, "Power deposition of a microstrip applicator radiating into a layered biological structure," *IEEE Transactions on Microwave Theory and Techniques*, vol. 36, no. 1, pp. 126–131, Jan. 1988.

[93] S. Jacobsen, H. O. Rolfsnes, and P. R. Stauffer, "Characteristics of microstrip muscle-loaded single-arm Archimedean spiral antennas as investigated by FDTD numerical computations," *IEEE Transactions on Biomedical Engineering*, vol. 52, no. 2, pp. 321–330, Feb. 2005.

[94] W. T. Chen and H. R. Chuang, "Numerical computation of the EM coupling between a circular loop antenna and a full-scale human-body model," *IEEE Transactions on Microwave Theory and Techniques*, vol. 46, no. 10, pt. 1, pp. 1516–1520, Oct. 1998. (Cited on Page 41)

[95] S. Curto and M. J. Ammann, "Electromagnetic interaction between resonant loop antenna and simulated biological tissue," *Microwave and Optical Technology Letters*, vol. 48, no. 12, pp. 2421–2425, Dec. 2006. (Cited on Page 41)

[96] H. R. Underwood, A. F. Peterson, and R. L. Magin, "Electric-field distribution near rectangular microstrip radiators for hyperthermia heating: theory versus experiment in water," *IEEE Transactions on Biomedical Engineering*, vol. 39, no. 2, pp. 146–153, Feb. 1992. (Cited on Page 41)

[97] C. Gabriel, "Compilation of the dielectric properties of body tissues at Rf and microwave frequencies," *Brooks Air Force Technical Report*, 1996. (Cited on Page 42)

[98] P. A. Mason, W. D. Hurt, T. J. Walters, J. A. D'andrea, P. Gajsek, K. L. Ryan, D. A. Nelson, K. I. Smith, and J. M. Ziriax, "Effects of frequency, permittivity, and voxel size on predicted specific absorption rate values in biological tissue during electromagnetic-field exposure," *IEEE Transactions on Microwave Theory and Techniques*, vol. 48, no. 11 Part 2, pp. 2050–2058, Apr. 2000. (Cited on Pages 42 and 60)

[99] T. Nagaoka, S. Watanabe, K. Sakurai, E. Kunieda, S. Watanabe, M. Taki, and Y. Yamanaka, "Development of realistic high-resolution whole-body voxel models of Japanese adult males and females of average height and weight and application of models to radio-frequency electromagnetic-field dosimetry," *Physics in Medicine and Biology*, vol. 49, no. 1, pp. 1–15, 2004. (Cited on Page 42)

[100] K. Ito, "Numerical and experimental human body phantoms," in *Proc. IET Seminar on Antennas and Propagation for Body-Centric Wireless Communications*, 2007, pp. 6–12. (Cited on Page 42)

[101] A. Christ, T. Samaras, A. Klingenbock, and N. Kuster, "Characterization of the electromagnetic near-field absorption in layered biologi-

cal tissue in the frequency range from 30 MHz to 6000 MHz," *Physics in Medicine and Biology*, vol. 51, no. 19, pp. 4951–4965, Sep. 2006.
(Cited on Page 42)

[102] A. Christ, A. Klingenbock, T. Samaras, C. Goiceanu, and N. Kuster, "The dependence of electromagnetic far-field absorption on body tissue composition in the frequency range from 300 MHz to 6 GHz," *IEEE Transactions on Microwave Theory and Techniques*, vol. 54, no. 5, pp. 2188–2195, May 2006. (Cited on Page 42)

[103] S. Curto and M. J. Ammann, "Electromagnetic coupling mechanism in a layered human tissue as benchmark for 434 MHz RF hyperthermia applicators," in *Proc. IEEE AP-S International Symposium on Antennas and Propagation*, 2007, pp. 3185–3188. (Cited on Pages 43 and 57)

[104] Z. Li, P. F. Maccarini, O. A. Arabe, V. Stakhursky, W. T. Joines, and P. R. Stauffer, "Towards the validation of a commercial hyperthermia treatment planning system," *Microwave Journal*, vol. 51, no. 12, pp. 28–42, Dec. 2008. (Cited on Pages 57, 61, 71, and 97)

[105] T. Samaras, A. Christ, A. Klingenbock, and N. Kuster, "Worst case temperature rise in a one-dimensional tissue model exposed to radiofrequency radiation," *IEEE Transactions on Biomedical Engineering*, vol. 54, no. 3, pp. 492–496, Mar. 2007. (Cited on Page 57)

[106] M. J. Ackerman, "The visible human project," *Proceedings of the IEEE*, vol. 86, no. 3, pp. 504–511, Mar. 1998. (Cited on Pages 57 and 58)

[107] D. G. Neuman, P. R. Stauffer, S. Jacobsen, and F. Rossetto, "SAR pattern perturbations from resonance effects in water bolus layers used with superficial microwave hyperthermia applicators," *International Journal of Hyperthermia*, vol. 18, no. 3, pp. 180–193, 2002.
(Cited on Pages 57, 64, 66, 74, and 76)

[108] E. A. Gelvich and V. N. Mazokhin, "Resonance effects in applicator water boluses and their influence on SAR distribution patterns," *International Journal of Hyperthermia*, vol. 16, no. 2, pp. 113–128, 2000.
(Cited on Pages 57, 64, 66, and 74)

[109] S. Curto, P. McEvoy, X. L. Bao, and M. J. Ammann, "Compact patch antenna for electromagnetic interaction with human tissue at 434 MHz," *IEEE Transactions on Antennas and Propagation*, vol. 57, no. 9, pp. 2564–2571, Sep. 2009. (Cited on Pages 58 and 76)

[110] D. S. Katz, M. J. Piket-May, A. Taflove, and K. R. Umashankar, "FDTD analysis of electromagnetic wave radiation from systems containing horn antennas," *IEEE Transactions on Antennas and Propagation*, vol. 39, no. 8, pp. 1203–1212, Aug. 1991. (Cited on Page 59)

[111] A. D. Tinniswood, C. M. Furse, and O. P. Gandhi, "Power deposition in the head and neck of an anatomically based human body model for plane wave exposures," *Physics in Medicine and Biology*, vol. 43, pp. 2361–2378, 1998. (Cited on Page 60)

[112] *IEEE Recommended practice for determining the peak spatial-average specific absorption rate (SAR) in the human head from wireless communications devices: measurement techniques*, IEEE Std. 1528–2003, 2003.
(Cited on Pages 60 and 81)

[113] M. M. Paulides, J. F. Bakker, E. Neufeld, J. Van der Zee, P. P. Jansen, P. C. Levendag, and G. C. Van Rhoon, "The HYPERcollar: A novel applicator for hyperthermia in the head and neck," *International Journal of Hyperthermia*, vol. 23, no. 7, pp. 567–576, Nov. 2007. (Cited on Page 60)

[114] H. K. Lee, A. G. Antell, C. A. Perez, W. L. Straube, G. Ramachandran, R. J. Myerson, B. Emami, E. P. Molmenti, A. Buckner, and M. A. Lockett, "Superficial hyperthermia and irradiation for recurrent breast

carcinoma of the chest wall: prognostic factors in 196 tumors," *International Journal of Radiation Oncology Biology Physics*, vol. 40, no. 2, pp. 365–375, 1998. (Cited on Page 60)

[115] J. Van der Zee, Z. Vujaskovic, M. Kondo, and T. Sugahara, "The Kadota fund international forum 2004 – Clinical group consensus," *International Journal of Hyperthermia*, vol. 24, no. 2, pp. 111–122, Mar. 2008. (Cited on Page 60)

[116] C. W. Song, A. Shakil, J. L. Osborn, and K. Iwata, "Tumour oxygenation is increased by hyperthermia at mild temperatures," *International Journal of Hyperthermia*, vol. 25, no. 2, pp. 91–95, 1995. (Cited on Page 61)

[117] P. Gajsek, W. D. Hurt, J. M. Ziriax, and P. A. Mason, "Parametric dependence of SAR on permittivity values in a man model," *IEEE Transactions on Biomedical Engineering*, vol. 48, no. 10, pp. 1169–1177, Oct. 2001. (Cited on Page 77)

[118] K. Ito and H. Kawai, "Solid phantoms for evaluation of interactions between the human body and antennas," in *Proc. IEEE IWAT International Workshop on Antenna Technology: Small Antennas and Novel Metamaterials*, 2005, pp. 41–44. (Cited on Page 81)

[119] J. Zhou, D. Hara, and T. Kobayashi, "Development of ultra wideband electromagnetic phantoms for antennas and propagation studies," in *Proc. IEEE EuCAP European Conference on Antennas and Propagation*, 2006, pp. 1–6. (Cited on Page 81)

[120] *Basic standard for the measurement of Specific Absorption Rate related to human exposure to electromagnetic fields from mobile phones (300 MHz–3 GHz)*, CENELEC Std. EN 50 361, 2001. (Cited on Page 81)

[121] *DASY Dosimetric Assessment System Manual*, Schmid and Partner Engineering AG, Oct 2002. (Cited on Pages 81 and 85)

[122] V. Komanduri, D. R. Jackson, and J. T. Williams, "Reducing surface-wave excitation from microstrip antennas by using a cavity filling," in *Proc. IEEE AP-S International Symposium on Antennas and Propagation*, 2007, pp. 2293–2296.   (Cited on Page 96)

[123] E. Rajo-Iglesias, L. Inclán-Sánchez, and O. Quevedo-Teruel, "Back radiation reduction in patch antennas using planar soft surfaces," *Progress in Electromagnetics Reseach Letters*, vol. 6, pp. 123–130, 2009.
(Cited on Page 96)

[124] D. Piazza, P. Mookiah, M. D'Amico, and K. R. Dandekar, "Two port reconfigurable circular patch antenna for mimo systems," in *Proc. IEEE EuCAP European Conference on Antennas and Propagation*, 2007, pp. 1–7.   (Cited on Page 97)

[125] M. Lazebnik, S. C. Hagness, and J. H. Booske, "Dielectric-properties contrast enhancement for microwave breast cancer detection: Numerical investigations of microbubble contrast agents," in *Proc. URSI Union Radio Science*, 2008.   (Cited on Page 98)

[126] M. Lazebnik, M. C. Converse, J. H. Booske, and S. C. Hagness, "Ultrawideband temperature-dependent tissue dielectric properties," *Physics in Medicine and Biology*, vol. 51, pp. 1941–1955, 2006.   (Cited on Page 98)

[127] D. Hodgins, A. Bertsch, N. Post, M. Frischholz, B. Volckaerts, J. Spensley, J. M. Wasikiewicz, H. Higgins, F. Von Stetten, and L. Kenney, "Healthy aims: developing new medical implants and diagnostic equipment," *IEEE Pervasive Computing*, vol. 7, pp. 14–21, 2008.
(Cited on Page 98)

A. List of Publications

Journal Publications

[JP 1] S. Curto, T. S. P. See, P. McEvoy, M. J. Ammann, Z. N. Chen, "In-silico hyperthermia performance of a compact patch antenna at various human anatomical regions," *IEEE Transactions on Biomedical Engineering*, (in review)

[JP 2] S. Curto, P. McEvoy, X. L. Bao and M. J. Ammann, "Compact patch antenna for electromagnetic interaction with human tissue at 434 MHz," *IEEE Transactions on Antennas and Propagation*, vol. 57, no. 9, pp. 2564–2571, Sept. 2009.

[JP 3] S. Curto, M. J. Ammann, "Electromagnetic interaction between resonant loop antenna and simulated biological tissue," *Microwave and Optical Technology Letters*, vol. 48, no. 12, pp. 2421–2425, Dec. 2006.

Invited Conference Publications

[ICP 1] M. J. Ammann, S. Curto, P. McEvoy, T. S. P. See and Z. N. Chen, "(Invited) A stable near-field antenna hyperthermia applicator for various tissue types and topologies," in *Proc. Loughborough Antennas and Propagation Conference*, Loughborough, UK, Nov. 16–17, 2009, pp. 76-79.

[ICP 2] M. J. Ammann, S. Curto, X. L. Bao, P. McEvoy, "(Invited) Antenna design considerations for high specific absorption rate in local hyperthermia treat-

ment," in *Proc. IEEE AP-S International Symposium on Antennas and Propagation*, San Diego, CA, USA, Jul. 05–11, 2008, session 126, paper 9.

Conference Publications

[CP 1] S. Curto, T. S. P. See, Z. N. Chen, P. McEvoy, M. J. Ammann, "Interaction of RF-Hyperthermia applicator with high fidelity human body model," in *Proc. IEEE AP-S International Symposium on Antennas and Propagation*, San Diego, CA, USA, Jul. 05–11, 2008, session 417, paper 6.

[CP 2] P. McEvoy, M. John, S. Curto and M. J. Ammann, "Spatial group delay patterns for three ultra wideband spline antennas," in *Proc. IEEE AP-S International Symposium on Antennas and Propagation*, San Diego, CA, USA, Jul. 05–11, 2008, session 145, paper 2.

[CP 3] P. McEvoy, S. Curto, M. John and M. J. Ammann, "Directive ultra wideband antennas for radar applications in wireless sensor networks," in *Royal Irish Academy Research Colloquium on Emerging Trends in Wireless Communications*, Dublin, Ireland, Apr. 24, 2008, pp. 103–105.

[CP 4] S. Curto, X. L. Bao, M. J. Ammann, "The electromagnetic interaction with tissue of a circular patch antenna, comprising a concentric ring and a radially slotted groundplane," in *Progress in Electromagnetics Research Symposium*, Hangzhou, China, , Mar. 24–28, 2008 pp. 372.

[CP 5] P. McEvoy, M. John, S. Curto and M. J. Ammann, "Group delay performance of ultra wideband monopole antennas for communication applications," in *Proc. Loughborough Antennas and Propagation Conference*, Loughborough, UK, Mar. 17–18, 2008, pp. 377–380.

[CP 6] S. Curto, M. J. Ammann, "Electromagnetic coupling mechanism in a layered human tissue as benchmark for 434 MHz RF hyperthermia applicators," in

Proc. IEEE AP-S International Symposium on Antennas and Propagation, Honolulu, Hawai'i, USA, Jun. 10–15, 2007, pp. 3185–3188.

[CP 7] S. Curto, M. John and M. J. Ammann, "Groundplane dependent performance of printed antenna for MB-OFDM-UWB," in *Proc. IEEE Vehicular Technology Conference,* Dublin, Ireland, Apr. 22–25, 2007, No. 44206, pp. 352–356.

[CP 8] S. Curto, X. L. Bao, M. J. Ammann, "Novel compact 434 MHz patch antenna for hyperthermia applications," in *Proc. EuCAP - European Conference on Antennas and Propagation,* Nice, France, Nov. 6–10, 2006, No. 349943.

[CP 9] S. Curto, M. J. Ammann, "Circular loop antenna operating at 434 MHz for medical applications: loop-tissue interaction," in *Proc. IEE Irish Signals and Systems Conference,* Dublin, Ireland, Jun. 28–30, 2006, pp. 327–330.

[CP 10] S. Curto, M. J. Ammann, "Resonant loop antenna operating at 434 MHz for medical applications; dosimetry and SAR evaluation," in *Proc. Loughborough Antennas and Propagation Conference,* Loughborough, UK, Apr. 11-12, 2006, pp. 229–232.